

**ADVANCED OXIDATIVE WATER TREATMENT PROCESS
USING AN ELECTROHYDRAULIC DISCHARGE REACTOR
AND TiO₂ IMMOBILISED ON NANOFIBRES**

By

Gauthier Nganda Okolongo

MSc Chemistry - University of the Western Cape

BSc Chemistry (honours) - National University of Pedagogics (D. R. Congo)



A thesis submitted in fulfillment of the requirements for the degree of Doctor of
Philosophy in Chemistry
In the Department of Chemistry, University of the Western Cape.

Supervisors: Prof. Leslie F. Petrik
Prof. Willem J. Perold

November 2013

Synopsis

To overcome the side effects of commonly used water disinfection methods based on chemicals, advanced oxidation processes (AOPs) are presently considered as alternatives. These processes are based on the effects of highly reactive oxidants, such as ozone, OH radicals, H₂O₂ etc., that act together as cocktail to decompose microorganisms and persistent organic compounds. Electrohydraulic discharges are one of the AOPs that have been studied for several years. However, the integration of innovations in nanoscience and nanotechnology has been incorporated into this area of work on a very limited scale. In this work the effects and products from newly designed electrohydraulic discharges have been investigated for their potential to remove organic contaminants and microbes from the water.

A novel and simple method to fabricate composite TiO₂ nanofibres, immobilised on a metal grid in the anatase structure, was devised, using an electrospinning technique, followed by a calcination process. The crystal structure, morphologies, surface area, and the photocatalytic activity of synthesized TiO₂ nanofibres were characterised by X-ray diffraction (XRD), transmission electron microscopy (TEM), scanning electron microscopy (SEM), Brunauer-Emmett-Teller (BET), nitrogen adsorption desorption isotherm, and UV-vis spectroscopy. The results revealed that hydrolysis of electrospun fibres, followed by carbonization at specific temperatures, had greatly influenced the morphologies and immobilization of TiO₂ nanofibres on supported material. The composite anatase nanocrystals formed were stable, even after 10 minutes of sonication. The photocatalytic activities of the TiO₂ nanofibres and anatase nanocomposites were evaluated by photocatalytic degradation of methylene blue (MB), as model dye, in water under permanent UV light irradiation originating from the electrohydraulic discharge. It was observed that the TiO₂ nano-crystalline composite obtained by calcination at 600°C for 2 hours, exhibited a higher photocatalytic activity than the commercial powder Degussa P-25. Best degradation results were achieved with a 36 W continuous duty cycle treatment. This combined advanced oxidation design has great commercial potential in realizing low cost water purification with effective power consumption, without the addition of chemicals.

Keywords

Electrohydraulic

Immobilized

Advanced

Cocktail

Oxidative

Methylene blue

Nanofibres

Discharge

Reactor

Titanium dioxide

Water treatment

Photocatalysis



Declaration

I declare that the research on "*Advanced oxidative water treatment process using an electrohydraulic discharge reactor and TiO₂ immobilized on nanofibres*" is my own work, and that it has not been submitted for any degree or examination at any other University and that all sources I have used or quoted have been indicated and acknowledged by complete references.

Gauthier Nganda Okolongo



November 2013



Acknowledgements

I would like to express my deepest regards and sincerest gratitude to Professor Petrik Leslie for her guidance, enthusiasm and support. I really appreciate her constant encouragement throughout my PhD studies, her faith in the abilities of the students and her ready availability on all matters. She is not only a helpful advisor, but also a mother.

There are a few people without whom this thesis would not have been possible:

- To my co-supervisor, Prof. W. J. Perold, thanks for your enthusiasm, readiness to support and thank you for giving me a working laboratory batch area in Electrical & Electronic Engineering at Stellenbosch University during the three years of my doctoral studies, allowing me to attend first year electrical courses and always finding the resources somewhere to support me, even from your own pocket during this study.
- To Ulrich Büttner, my fellow researcher, thank you for all the time and skills you invested in this study, for being always available to repair and rebuild the high voltage power supply and prototype designs in the way I requested and needed.
- To Prof. Corinne Greyling for the support and help to overcome the multiple challenges on multi-gate and electrospinning processes.
- To Prof. Ronald Sanderson and the *NRF Flagship Project* for the financial support that made this study possible.
- To Dr. Patrick Ndungu, and Dr. Fatoba for agreeing to proof read reports and some sections of my thesis. Kasongo and Guillaume for always being there to help even during the sad and tough situation I was in. Stanley, Arnoux, Niel for a lot of essential help and Petrus for teaching me the high voltages works.
- I am grateful to all my lab mates, technicians and all the staff of the Chemistry Department at UWC, for the past and present helpful discussions, and providing a friendly environment to work in and study.
- I am very grateful to my parents and family members for their constant encouragement.
- I am especially grateful to my lawful wife, Josephine, and my four wonderful children, Glad, Chris, Believe and Praise Okolongo, for their belief in me and their uncon-

ditional love, understanding and prayers that kept me going even when times were very tough.

Above all, and the most needed, many thanks to the omnipresent God for the strength, mercies and blessings throughout the whole journey.



Contents

Synopsis	i
Keywords	ii
Declaration	iii
Acknowledgements	iv
Contents	vi
List of Figures	xi
List of Tables	xvi
Abbreviations	xvii
Academic outputs of research reported in this thesis	xviii
1 Introduction	1
1.1 Background	1
1.2 Problem statement	3
1.3 The aims and objectives of the current research	4
1.4 Research questions	4
1.5 Hypothesis	5
1.6 Research approach	6
1.7 Scope and delimitations of the study	7
1.8 Layout of thesis chapters	8
2 Literature review	9
2.1 Advanced oxidation processes (AOP)	9
2.1.1 Anodic oxidation	10
2.1.2 Ozone oxidation	11
2.1.3 UV/O ₃ Process	12
2.1.4 Hydrogen peroxide oxidation	12
2.1.5 H ₂ O ₂ /UV Process	14
2.1.6 O ₃ /H ₂ O ₂ Process	14



2.1.7	Fenton's reaction process	14
2.2	Electrical discharge in water	16
2.2.1	Introduction	16
2.2.2	Corona discharge	16
2.2.3	Types of electrical discharges for water treatment	16
2.2.3.1	Electrical discharges above the water surface	17
2.2.3.2	Electrical discharges occurring deeper in water	18
2.2.3.3	Electrohydraulic discharge for water treatment	20
2.2.3.4	Electrode and Electrical Parameters in Electrohydraulic Discharges	21
2.2.4	Propagation of pulsed electrical discharges in water	22
2.2.4.1	Pulsed corona discharge for water treatment	24
2.2.4.2	Configurations for electrical corona discharge	24
2.2.4.3	Chemical processes of active species in corona discharge	25
2.2.4.4	Reaction mechanism	26
2.2.4.5	Physical processes of active species in corona discharge	26
2.2.4.6	Dielectric-barrier discharge (DBD)	27
2.2.5	Influence of dissolved oxygen on the production of active species	30
2.2.6	Factors that impact the plasma reaction	31
2.2.6.1	Electrode structure	31
2.2.6.2	Electrode gap	31
2.2.6.3	Input voltage	32
2.2.6.4	Pulse repetition rate	32
2.2.6.5	Airflow rate	33
2.2.6.6	Conductivity of the solution	33
2.3	Design and construction of the reactor	33
2.3.1	Introduction	33
2.3.2	The needle-plate	33
2.3.3	The pinhole electrode	34
2.3.4	The ring to cylinder	34
2.3.5	The wire to cylinder	34
2.3.6	Multi-electrodes	34
2.3.7	Preliminary conclusion	35
2.4	Photocatalysis	35
2.4.1	Introduction	35
2.4.2	Principle of photocatalytic oxidation	36
2.4.3	TiO ₂ as semiconductor	38
2.4.4	Titanium dioxide and crystalline phases	38
2.4.5	Structural properties of TiO ₂ nanomaterials	41
2.4.6	Properties of TiO ₂ nanomaterials	42
2.4.7	Applications of TiO ₂	43
2.4.8	Photo-induced electron and hole properties of TiO ₂ nanomaterials	43

2.4.9	Toxicity of TiO ₂ particles to the environment	44
2.4.10	Various light sources	44
2.4.11	Photocatalytic water splitting	45
2.4.12	Preparation methods for TiO ₂ nanostructures	45
2.4.12.1	Sol-gel method	45
2.4.12.2	Hydrothermal method	46
2.4.12.3	Solvothermal method	47
2.4.12.4	Comparison between hydrothermal and sol-gel methods	47
2.5	Electrospinning	48
2.5.1	Introduction	48
2.5.2	Fabrication of TiO ₂ nanofibres via electrospinning, combined with the sol-gel method	50
2.5.3	Transformation of TiO ₂ nanofibres	51
2.6	Chapter Summary	53
3	Materials and experimental procedures	54
3.1	Materials and chemicals	54
3.2	Experimental	55
3.2.1	Experimental setup	55
3.2.2	Equipment	56
3.2.3	Designs of prototypes	57
3.2.3.1	Prototype OK-1	57
3.2.3.2	Prototype OK-2	57
3.2.3.3	Prototype OK-3	59
3.2.4	Degradation of Methylene blue (MB) using OK-1 and OK-2	60
3.2.4.1	Preparation of standard solutions	60
3.2.5	Protocol for testing OK-3 with dye solutions	61
3.2.6	Disinfection of model solutions using OK-3	62
3.2.6.1	Enumeration of bacteria	62
3.2.7	Solar Disinfection (SODIS)	64
3.2.8	Synthesis of TiO ₂ nanofibres as photocatalyst	65
3.2.9	Preparation of electrospun nanofibres impregnated with titanium dioxide	66
3.2.10	Electrospinning process	66
3.2.11	Calcination of nano composite fibres	67
3.2.12	Carbonization of nano composite fibres	67
3.2.13	Sputter deposition and incorporation in the prototype OK-3	67
3.2.13.1	Methodology	67
3.3	Physical characterization techniques and experimental details	68
3.3.1	Introduction	68
3.3.2	Fourier Transform Infra-Red Spectroscopy	69
3.3.2.1	Experimental details: Sample preparation	69

3.3.3	X-Ray Diffractometer	69
3.3.3.1	Experimental details: Sample preparation	69
3.3.4	High Resolution Scanning Electron Microscopy (HRSEM)	70
3.3.4.1	Experimental details: Sample preparation	70
3.3.5	High Resolution Transmission Electron Microscopy (HRTEM)	70
3.3.5.1	Experimental details: Sample preparation	70
3.3.6	Brunauer-Emmet-Teller (BET) N ₂ adsorption	71
3.3.6.1	Experimental details: Sample preparation	71
3.3.7	Energy Dispersive Spectroscopy (SEM-EDS)	71
3.4	Measurement of photocatalytic activity	72
3.4.1	pH	72
3.4.2	Concentration of the dye	72
3.4.3	Analysis of the catalytic degradation achieved	73
3.5	Detection of chemicals from the aliquots	73
3.5.1	Sample preparation for ESR detection of hydroxyl and superoxide radicals	73
3.5.2	Methanol as OH radical scavenger	74
3.5.3	Ozone detection	75
3.5.4	Hydrogen peroxide detection	76
3.5.5	Ion Chromatography (IC)	76
3.5.5.1	Procedure	77
4	Results of prototype design	78
4.1	Motivation	78
4.2	Degradation of Methylene blue using different prototypes reactors	79
4.2.1	Prototype made with PVC (OK-1)	79
4.2.1.1	Results on the effectiveness of OK-1	79
4.2.2	Prototype made with Perspex (OK-2)	80
4.2.2.1	Results on the effectiveness of OK-2	80
4.2.3	Prototype made with quartz glass (OK-3)	81
4.2.3.1	Effectiveness of OK-3 with dye solutions	82
4.2.3.2	Influence of water conductivity	84
4.2.3.3	Corrosion	85
4.2.3.4	Results and discussions	88
4.2.3.5	Comparative results between solar disinfection (SODIS) and the OK-3 reactor using river water	92
4.2.3.6	Summary conclusion	93
5	Results of synthetic TiO₂ nanofibres and its degradation efficiency	94
5.1	Comparison between TiO ₂ nanofibres and commercial TiO ₂ nanoparticles (Degussa P-25)	94

5.1.1	Structural changes and phase formation of TiO ₂ nanofibres and baseline material by XRD	95
5.1.2	Surface area and pore size distribution of the synthetic and baseline material	96
5.1.3	Structural changes and functionalization of TiO ₂ nanofibres	98
5.1.4	High Resolution Scanning Electron Microscopy (HRSEM)	99
5.1.5	High Resolution Transmission Electron Microscopy (HRTEM)	104
5.2	Integration of nanomaterials into the reactor	106
5.2.1	Photocatalytic activity	106
5.2.1.1	Effect of different catalysts on photocatalytic activity of MB without dissolved ozone	106
5.2.1.2	Effect of pH on photodegradation	107
5.2.1.3	Effect of MB concentration on photodegradation	108
5.2.1.4	The effect of air flowing through the system on the photodegradation of MB	108
5.2.1.5	The effect of TiO ₂ nanofibres on the photodegradation of Methylene blue	109
5.3	Detection of active species	110
5.3.1	ESR spin-trapping experiments under UV light for OH radical detection	110
5.3.2	Ozone detection	112
5.3.3	Hydrogen peroxide detection	113
5.4	Ion Chromatograph-Mass Spectra (IC-MS) results	114
6	Conclusions and Recommendations	117
6.1	Introduction	117
6.2	Conclusions	117
6.3	Significance of the current study to the scientific and industrial community .	118
6.4	Recommendations for future work	120
	Appendices	121
	A Summary of Advanced Oxidative Processes	122
	B Details of the new design reactor (OK-3)	125
	C SEM images of different samples	131
	List of References	133

List of Figures

1.1	Summary of the research approach of this study	6
2.1	Electron-transfer scheme for anodic oxidation processes: [A] Direct oxidation, and [B] indirect oxidation	10
2.2	Schematic of the splitting of oxygen molecules by an electric field to form ozone	11
2.3	Major chemical reaction paths leading to the production of oxidants with outcome in corona discharges. (Blue dots represent reactions taking place in the bulk solution; red dots show reactions occurring at the interface and inside the plasma channel)	15
2.4	Lightning type of natural corona discharge	16
2.5	Electrical discharge above the surface of wastewater	17
2.6	Simplified illustration of some possible different electrode configurations for electrical discharges in water; (a) two plane electrodes, (b) a plane electrode and a needle electrode, (c) two needle electrodes, (d) a plane electrode with a multi-needle electrode, (e) gliding arc electrodes, and (f) coaxial reactor configuration	21
2.7	Historic sketch of the ozone discharge tube	27
2.8	Production of ozone through dielectric discharge	28
2.9	UV irradiation from the discharge gap between electrodes	28
2.10	DBD reactor using different electrode configurations	29
2.11	The influence of electrode gaps on electrical discharge	32
2.12	Typical images of the pulsed positive streamer discharge in the polluted water for different conductivities a) 1 $\mu\text{S}/\text{cm}$, b) 200 $\mu\text{S}/\text{cm}$, c) 600 $\mu\text{S}/\text{cm}$. The initial phenol concentration was 0.62 mM and the pulse energy 0.7 J	33
2.13	Diagram showing the processes involved in photo-mineralization of organic compounds	36
2.14	The photocatalytic reaction mechanisms	37
2.15	Titanium dioxide commercial fine white powder	39
2.16	Rutile in crystal form	39
2.17	Rutile structure	39
2.18	Anatase in crystal form	40
2.19	Anatase structure	40
2.20	Brookite in crystal form	40

2.21	Brookite structure	40
2.22	The electrospinning process	49
2.23	Photographs of the electrospinning setup with temperature control	51
3.1	The experimental setup	55
3.2	Two different photos showing (A) the uncirculated water system and (B) the circulated water experimental setup, using the same power source	56
3.3	The OK-1 reactor during discharge, which produces the UV irradiation on top of the dielectric glass material, and also ozone. A) Top side picture of the multi electrodes OK-1, B) Bottom side picture with one plate copper electrode of OK-1, C) complete setup, showing all the necessary peripheral items to operate the OK-1 and to circulate the water for treatment and D) The OK-1 reactor during discharge, which produce the UV irradiation on top of the dielectric glass material, and also ozone	57
3.4	CAD drawing of the discharge reactor	58
3.5	Images of OK-2, a), b) & d) are bottom, top and side views of the electrohydraulic discharge reactor, and c) is the setup used to test the reactor. (1) is the power supply for the pump, (2) is the power supply for the reactor, (3) is the high voltage probe connected to the (5) oscilloscope, (4) is the multimeter used to measure the current, (6) is the laptop for storing the data of the oscilloscope, (7) is the reactor, and (8) is a beaker with a water pump used to circulate water through the reactor.	59
3.6	A) picture of the OK-3, B) One unit of OK-3 in a beaker and connected to the power supply, C) the OK-3 during discharge, and D) complete setup showing all necessary peripheral items to operate the OK-3 and to circulate the water for treatment.	60
3.7	Standard curve for Methylene blue	61
3.8	(a) Illustration of the serial dilutions used to determine suitable concentration of <i>E. coli</i> for the count number determination in subsequent plating, and (b) example of actual agar plates with <i>E. coli</i> colonies	63
3.9	Solar disinfection design photos	64
3.10	Schematic illustration of the photocatalyst preparation protocol	65
3.11	Schematic illustration of the photocatalyst preparation protocol with ratio and different temperatures	65
3.12	Image (a) is a schematic of the electrospinning setup, and (b) is a photograph of an experimental run	66
3.13	Furnace used for the carbonization of fibres	67
3.14	Photographs of the electrospun nanofibres without carbonization (A) wrapped on an outer tube of the rig system, (A1) connected to the high voltage power supply, and (A2) the wrapped rig submerged into the contaminated water with MB (10 ppm).	68

3.15	Photographs of the TiO ₂ nanofibres electrospun on grid supporting material and carbonized in nitrogen at 600°C, (B) bent on the outer tube of the rig system, (B1) connected to the high voltage power supply, and (B2) the rig submerged in the contaminated water with MB (10 ppm).	68
3.16	Photograph of the ESR apparatus used in this study for OH radical detection	74
3.17	Setup for the detection of ozone and hydrogen peroxide	75
3.18	Photograph of the Ion Chromatograph used in this study	77
4.1	The measured degradation of MB (10 ppm) using OK-1, under the following conditions: 12 kV at 3 mA, pH 6, flowrate of 100ml/min	80
4.2	The measured degradation of MB (10 ppm) using OK-2, under the following conditions: 12 kV at 3 mA, pH 6, flowrate of 100 ml/min.	81
4.3	Degradation of acid orange, Rhodamine blue and Methylene blue (respectively from left to right) under the following conditions: 12 kV at 3 mA, pH 6, flowrate of 2l/min	82
4.4	UV-Vis result of the degradation of acid orange (4-(2-Hydroxynaphthylazo) benzenesulfonic acid sodium salt) (λ_{max} = 485 nm)	83
4.5	UV-Vis result of the degradation of Rhodamine blue(3', 6'-Bis (diethylamino) spiro[isobenzofuran-1(3H), 9'-[9H]xanthene]-3-one) (λ_{max} = 554 nm)	83
4.6	UV-Vis result of the degradation of Methylene blue (3,7-bis(Dimethylamino)-phenothiazin-5-ium chloride) (λ_{max} = 665 nm)	84
4.7	Dependence of UV transparency on dielectric materials, such as Pyrex and Quartz, using different electrolytes such as NaCl and CuSO ₄	85
4.8	Influence of electrolyte on the UV irradiation and discharge light above the water	85
4.9	Photograph of the initial copper electrode and after 24 hours of use	86
4.10	Dependence of the pH and conductivity on running time	86
4.11	(A1) The decoloration of MB after 48 min using the dissolved ozone from OK-3 and (A) no significant color change without ozone	87
4.12	(B1) The decoloration of MB after 30 min, using the dissolved ozone from OK-3, UV and other species (B)	87
4.13	The degradation of MB after different running times (0, 10, 20 and 30 minutes)	88
4.14	The measured change of the spectrum of Methylene blue solution after 0, 10, 20 and 30 min of discharge plasma treatment (applied voltage = 12 kV, treatment time = 30 min)	89
4.15	Changes in the FT-IR peak spectra during degradation of MB at different running time	89
4.16	Presentation of the mass extraction of the initial MB solution when the power was off	90
4.17	Presentation of the peak area integration of the initial MB solution when the power was off	90
4.18	The shifting peak of mass extraction of MB after 30 min running time	91
4.19	The shifting peak area integration of MB after 30 min running time	91

4.20	The measured change in carbon NMR of MB (A) before and (A1) after 30 min . . .	91
4.21	A photo of the solar disinfection model (SODIS)	92
4.22	The inactivation of microbes from contaminated river water: (A) Control plate with initial concentration, (A1) the prototype OK-3 and (A2) the solar disinfection method (SODIS)	92
5.1	XRD phase identification of commercial TiO ₂ as baseline material	95
5.2	XRD analysis of pure PAN and TiO ₂ /CNF catalysts synthesized by the electrospinning method and carbonised at 600°C in N ₂	95
5.3	CNF pore-size distributions of TiO ₂ CNF at 600°C	97
5.4	The pore size distribution of commercial TiO ₂ particles and TiO ₂ CNF at 600°C .	97
5.5	N ₂ adsorption-desorption isotherm of commercial TiO ₂ particles compared to synthetic TiO ₂ nanofibres, using N ₂ BET	98
5.6	The FTIR spectra of unstabilized TiO ₂ and stabilized TiO ₂ nanofibres	98
5.7	The specific FTIR peak area of (A) unstabilized TiO ₂ and (A1) stabilized TiO ₂ nanofibres	99
5.8	HRSEM images of (b) commercial TiO ₂ (a) TiO ₂ nanofibres stabilized at 600°C in nitrogen	100
5.9	SEM images of electrospun TiO ₂ nanofibres: (a) As-electrospun TiO ₂ fibre; (b) After carbonization at 600°C in nitrogen for 3 hours; (c) magnification 5000 × 30 μm (d) magnification 4300 × 20 μm (e) magnification 8500 × 10 μm after 10 min of sonication (f) magnification 7200 × 10 μm after 10 min of sonication	100
5.10	The non-woven on grid supporting material before (A and B) and after calcination (C)	101
5.11	SEM images of new fashion electrospun TiO ₂ nanofibres (A, B and C) after hydrolysis, at different magnifications, carbonized at 600°C in nitrogen, and SAED of the same sample.	102
5.12	SEM images of electrospun TiO ₂ nanofibre (A) TiO ₂ fibres on the grid (B) Same sample without hydrolyzed before carbonization at 600°C in nitrogen. (C) Same sample magnified at 1 μm and SAED image of the same sample.	102
5.13	SEM images of a sample prepared as in Section 3.2.13 with a combination of sputtering and electrospinning techniques. (A) As wet electrospun fibres; (B) Magnified; (C) Calcinated and its SAED image.	103
5.14	Selected HRTEM images of electrospun TiO ₂ nanofibres at different magnifications.	104
5.15	EDS pattern of the synthetic TiO ₂ /CNF.	105
5.16	The photo degradation effect of different catalyst nanomaterials on Methylene blue (MB) (50 mg/l) over time, without air flowing through the system.	107
5.17	The effect of pH change on the degradation of MB (50 ppm MB, 15 kV, 30 kHz). .	107
5.18	The effect of different MB concentrations on the photodegradation efficiency of catalysts (15 ppm MB, 20 kV, 25 kHz).	108

5.19	The effect of airflow on dye removal efficiency (TiO ₂ NF at 600°C, MB concentration 50 ppm, pH=7, 20 kV and 25 kHz).	109
5.20	Catalytic effect of TiO ₂ nanofibres, carbonized at 600°C, on MB degradation (20 kV, 25 kHz, MB concentration 50 ppm and pH=7).	109
5.21	Summary of the results of OH radical detection using ESR.	111
5.22	Compilation of ESR peak spectra of DMPO-OH adduct observed before and after power on.	112
5.23	The change of colour when ozone is bubbled in a 0.1M solution of KI.	113
5.24	The colour changes that occur when hydrogen peroxide reacts with titanium sulphate.	114
5.25	The intensity peaks of different standard solutions.	114
5.26	The intensity peaks of the MB solution after 10 minutes.	115
5.27	The intensity peaks of the MB solution after 20 minutes.	115
5.28	The intensity peaks of the MB solution after 30 minutes.	116
5.29	The intensity peaks of the MB solution after 60 minutes.	116
B.1	Fully assembled reactor vessel	125
B.2	Fully assembled reactor vessel (wire frame view)	126
B.3	Reactor vessel with end cap removed	126
B.4	Reactor vessel with electrode placement disk and electrodes removed	127
B.5	Reactor with shell flange removed	127
B.6	Reactor vessel with shell removed	127
B.7	Perspex shell dimensions	128
B.8	Teflon baffle dimensions	128
B.9	Baffle placement in shell	128
B.10	Quartz tube dimensions	129
B.11	Teflon shell flange dimensions	129
B.12	Teflon electrode placement disk dimensions	129
B.13	Perspex end cap dimensions	130
C.1	SEM images of different samples	132

List of Tables

2.1	Some characteristic of electrical discharges in water (Locke et al., 2006)	21
2.2	Summary of electrode configurations and actives species production	25
2.3	Comparison of air and high purity oxygen feed systems	30
2.4	Types and physical properties of titanium oxide	41
2.5	Diameters and physical properties of precalcined as-spun PVP/TiO ₂ composite nanofibres and calcined TiO ₂ nanofibres at various calcination temperatures . . .	52
3.1	Summary of chemicals used in the study without further purification	54
3.2	List of design tools and supplies	56
3.3	Methylene blue standard solutions	61
3.4	Experimental parameters used with the OK-3 reactor	62
3.5	Summary of characterization techniques used during catalyst development . . .	69
3.6	FTIR experimental instrument conditions	69
3.7	The Siemens D8 Advance XRD operational parameters	70
3.8	HRSEM instrument experimental parameter settings	70
3.9	HRTEM instrument experimental conditions	71
3.10	Hitachi X-650 SEM operational parameters	72
5.1	BET surface area and micropore area of synthetic TiO ₂ nanofibres and commercial TiO ₂	96

Abbreviations

HT	: High Tension
HV	: High Voltage
ESR	: Electron Spin Resonance
AOP	: Advanced Oxidative Process
HRTEM	: High Resolution Transmission Electron Microscopy
HRSEM	: High Resolution Scanning Electron Microscopy
TPR	: Temperature Programmed Reduction
BET	: Brunauer-Emmett-Teller
CVD	: Chemical Vapour Deposition
EDS	: Energy Dispersive Spectroscopy
FTIR	: Fourier Transform Infrared
SAED	: Selected area electron diffraction
MB	: Methylene Blue
MDG	: Millennium Development Goals
nm	: Nanometres
SODIS	: Solar disinfection
TiO ₂	: Titanium Dioxide
XRD	: X-Ray Diffractometry
VB	: Valence Band
CB	: Conduction Band
θ	: Theta angle
λ	: Wavelength
PAC	: Powdered activated carbon
LC-MS	: Liquid Chromatography-Mass Spectrometry
NMR	: Nuclear Magnetic Resonance
UF	: Ultra filtration
UV	: Ultraviolet
RO	: Reverse osmosis
MF	: Microfiltration
OK-1	: Okolongo reactor number one
OK-2	: Okolongo reactor number two
OK-3	: Okolongo reactor number three

Academic outputs of research reported in this thesis

This project falls under NRF Flagship Project Nanotechnology for Water Treatment, in collaboration between two universities, namely the University of the Western Cape and Stellenbosch University. The emphasis of the research was to find different designs, assisted by technical staff members at the Department of Electrical & Electronic Engineering, Mr. Ulrich Büttner and Mr. Petrus Pieterse, to build prototypes and a power supply, respectively. Thereafter, finding ways to apply nanoscience for cleaning drinking water, which led me to produce a thesis that resulted in two international patent applications, one peer reviewed conference paper, four international oral presentations and two poster presentations. Additionally, two papers, one under submission and another in preparation for publishing in international journals, were produced.

UNIVERSITY of the
WESTERN CAPE

Patent applications

1. P2269PC00/MVS - New PCT International Patent Application No. PCT/IB2012/052290 for "Water treatment apparatus". Innovators: Stellenbosch University and the University of the Western Cape.
2. P2270PC00/MVS - New PCT International Patent Application No. PCT/IB2012/052291 for "Photo-catalyst and its preparation". Innovators: Stellenbosch University and the University of the Western Cape.

Peer reviewed conference paper and publication papers in preparation

1. G. Okolongo, P. Ndungu, A. Nechaev, W. Perold, U. Büttner, and L. Petrik. "Advanced oxidative water treatment process using an electrohydraulic discharge reactor and TiO₂ immobilised on nanofibres". *International Water Association (IWA) Specialist Conference on Application of Nanotechnology in the Water Sector*, 15 – 18 May, 2011, Monte Verita, Ascona, Switzerland.
2. G. Okolongo, P. Ndungu, A. Nechaev, W. Perold, U. Büttner, and L. Petrik. "The influence of reactive oxygen species in the advanced oxidation process for inactivation of

microorganisms using ROUPPLA system". (Manuscript in preparation)

3. G. Okolongo, P. Ndungu, A Nechaev, W. Perold, U. Büttner, and L. Petrik. "Preparation and immobilization of titanium dioxide nanoparticles on nanofibres and grid supports for degradation of methylene blue". (Manuscript in preparation)

Oral presentations

1. G. Okolongo, P. Ndungu, A Nechaev, W. Perold, U. Büttner, and L. Petrik. "Advanced oxidative water treatment process using an electrohydraulic discharge reactor and TiO₂ immobilised on nanofibres". *International Water Association (IWA) Specialist Conference on Application of Nanotechnology in the Water Sector*, 15 – 18 May, 2011, Monte Verita, Ascona, Switzerland.
2. G. Okolongo, P. Ndungu, A Nechaev, W. Perold, U. Büttner, and L. Petrik. "Advanced oxidative water treatment process using an electrohydraulic discharge reactor (ROUP-PLA)". *WISA and Water Affairs 3rd Municipal Water Quality Landscape Conference*, 27 June – 1 July 2011, CTICC, Cape Town, South Africa.
3. G. Okolongo, P. Ndungu, A Nechaev, W. Perold, U. Büttner, and L. Petrik. "Advanced oxidative water treatment process using an electrohydraulic discharge reactor and TiO₂ immobilised on nanofibres". *Nanotechnology and University of Stellenbosch Conference*, 29 July 2011, STIAS, Stellenbosch, South Africa.
4. G. Okolongo (University of the Western Cape), Emma Ten Holter (Rotterdam University of Applied Sciences), Lamprini Naskia (Free University Amsterdam). *International Water Week Amsterdam Wetskills Innovation Challenge (IWWA)* 15-29, 2011, Innovative solutions for Watergraafsmeer's flood challenges , The Netherlands.

Poster presentations

1. G. Okolongo, P. Ndungu, A Nechaev, W. Perold, U. Büttner, and L. Petrik. "Advanced oxidative water treatment process using an electrohydraulic discharge reactor (ROUP-PLA)", *40th SACI Convention*, 16 – 21 January 2011, University of the Witwatersrand, Johannesburg, South Africa.
2. G. Okolongo, W. Perold, U. Büttner, A Nechaev, R. Akinyeye and L. Petrik. "Advanced oxidative water treatment process using an electrohydraulic discharge reactor and TiO₂ immobilised on nanofibres". *11th Annual UNESCO/IUPAC Conference on Functional Polymeric Materials & Composites*, 27 – 29 April 2011, Stellenbosch, South Africa.

Chapter 1

Introduction

1.1 Background

Conventional water and wastewater treatment processes, such as chlorination or boiling, have been long established in removing many chemical and microbial contaminants of concern for better quality of life of populations in developing countries. However, the effectiveness of these processes has become limited over the last two decades, due to the identification of emerging contaminants, the rapid growth in population, industrial activities, and the diminishing availability of water resources. These have constituted new challenges for drinking water supplies (Langlais et al., 1991; Mallevalle et al., 1996). Providing access to clean water and sanitation is a priority worldwide and ways of achieving the United Nations Millennium Development Goals (MDG) objectives by 2015 include the exploration and development of new technologies for cleaning and improving water supplies (Steiner et al., 2010). Three emerging treatment technologies, namely membrane filtration, advanced oxidation processes (AOPs), and UV irradiation, hold great promise to provide alternatives for better protection of public health and the environment. In this dissertation emphasis is placed on basic principles, main applications, and new developments in AOPs. Advantages and disadvantages of these technologies are compared (Appendix A) to highlight their current limitations and future research needs. (Mallevalle et al., 1996).

It can be noticed that, along with the growing knowledge and the advances in the manufacturing industry, the application of these technologies has increased at a first-order scale, but are costly for full implementation. Membrane filtration processes have been shown to be very effective in solid-liquid separation and in the removal of organic and inorganic materials (Jacangelo et al., 1995). Although desalination by reverse osmosis (RO) remains the most important application in water treatment in the near future, microfiltration (MF) and ultrafiltration (UF) have played increasingly significant roles in response to the need for disinfection of resistant microorganisms, such as *Giardia* and *Cryptosporidium*, while removing disinfection by-products (DBPs) precursors. To further improve the membrane processes, the major issues include the better understanding of membrane fouling mechanisms, more effective fouling control strategies, better membrane materials and module designs, and membrane integrity management. Wiesner et al., (1994) concluded that the cost of new

pressure-driven membrane filtration plants are expected to be comparable with, or even more, than those using conventional treatment processes for capacities up to 20 000 m³/day. Moreover, other authors (Chellam et al., 1998, Wiesner et al., 1994) prepared detailed cost analyses based on membrane fouling rates, backwash intervals and frequencies, and found that the method is expensive. The reuse of municipal and industrial wastewaters and the recovery of waste and removal of potential pollutants from effluents in industrial processes thus become more critical. This is especially true in arid or semi-arid areas, where potable water and irrigation water must be imported at great expense.

Ozone has been widely used as an alternative disinfectant to remove chlorine-resistant microbial contaminants. In addition, ozone has been used for colour reduction, taste and odour control, oxidation of trace synthetic organic compounds, and destabilization of particles. By properly combining ozone, hydrogen peroxide, UV, and heterogeneous photocatalysts, many advanced oxidation processes (AOPs) have been developed. Most of these processes are still in the development stage, but hold great promise, because they are more effective in oxidizing refractory organic contaminants. More research is needed to better understand and control ozonation by-products, and improve the efficiency of AOPs for the oxidation of organic contaminants.

To further use these advanced treatment processes, a number of hybrid processes have been suggested, which are formed by combining the advanced treatment processes with other conventional treatment processes. The materials used in these hybrid processes include membranes combined with powdered activated carbon (PAC), membrane bioreactor, and AOPs-biodegradation (Boman et al., 1991; Brindle et al., 1999). These processes may hold the greatest promise in the future because, if properly used, they can provide the most effective and economical approach to dealing with challenging environmental problems, which cannot be resolved using conventional treatment methods.

Recently, a non-thermal plasma technology, called electrohydraulic discharge as one of AOPs-biodegradation, has been applied for the inactivation of microbes. The application of non-thermal plasmas in water has been studied for two decades, because of its practical applications in drinking water and wastewater treatment, as well as in environmentally benign chemical processes (Ching et al., 2001). The current status of research on the application for promoting chemical reactions in the aqueous phase has been well reviewed (Locke et al., 2006). The non-thermal plasma technique is effective, simple, fast, and without residual toxicity for water treatment and can also produce UV-light (Chang et al., 2001).

Three types of plasma for water treatment have been utilized. These include remote plasma (such as glow discharge falling water film), indirect plasma (such as electron beam), and direct plasma (such as pulsed arc) (Chang et al., 2001). Electrohydraulic discharge is one of the direct plasma techniques and it is also defined as an advanced oxidation process.

The electrohydraulic discharge in water can form various active species and these species may play an important role in the in-situ killing of bacteria and degrading of organic compounds. Therefore, great attention is focused in this dissertation on advanced oxidation processes (AOP) that are based on the input of energy into the water in order to split it and in-situ production of highly reactive oxidants (such as O₃, OH radicals, H₂O₂, O[•], etc.) as an

alternative to chlorination (Sugiarto et al., 2002). The most interesting advantage of electrohydraulic discharge, beside active species production, is that it can generate UV irradiation, which could be used for the photocatalysis process.

1.2 Problem statement

The quality of drinking water is a powerful environmental determinant of health. Assurance of drinking water safety is a foundation for the prevention and control of waterborne diseases (WHO, 2000). Conventional water treatment methods, such as chlorination, have disadvantages such as handling of hazardous chemicals and producing by-products (trihalomethanes), which increase the risk of cancer (Dvorak & Skipton et al., 2008). Despite several treatment technologies being applied to treat water, there is no single conventional method that can remove or treat all contaminants in drinking water at once. Often, the combination of different treatment processes is required to effectively treat water. Titanium dioxide is a good photocatalyst for the degradation of organic pollutants, but it has many drawbacks, such as a very low settling velocity of its powder and the requirement of a long retention time in the clarifier (Fatta-Kassinos et al., 2010). Another problem is that, as the titanium dioxide loading content is increased, the photocatalytic activity is reduced, because of an increase in turbidity in the solution to be treated due to high titanium dioxide concentration (Qamar et al., 2006). Therefore the turbidity can decrease the depth of the UV light penetration from the sun (Hader et al., 2007).

Among the photocatalysts, TiO_2 with anatase phase has been most widely investigated in the slurry form, due to its acceptable photocatalytic activity under UV radiation, chemical stability, and low cost (Doh et al., 2007). Unfortunately, the use of nanometric photocatalysis has also presented problems, such as the separation of catalyst particles from the suspension after photocatalysis and the possibility of aggregation of the suspended particles. Therefore, the way of overcoming this problem will be to integrate the photocatalyst upon support materials, such as polymer nanofibres, using electrospinning techniques. The electrospinning process has been largely used as a facile way to prepare nanofibres, and it can be used to convert TiO_2 nanoparticles into long nanofibres, with the aid of a polymer base (Hu et al., 2006) to produce filters, membranes, optical and electronics applications, amongst others. However, polymer nanofibres are degraded by free radicals. A route should thus be found to introduce polymer free supported TiO_2 .

Moreover, recent studies have shown that UV irradiation may also be very effective in killing *Cryptosporidium* (Ventresque et al. 1997; Yoo et al. 1995). However, the source of UV irradiation is not permanent when using solar irradiation, or unreliable and expensive using mercury lamps to perform the photocatalysis. It is likely that UV application in water treatment will expand rapidly. So a permanent and inexpensive source of UV irradiation is very important and need to be addressed.

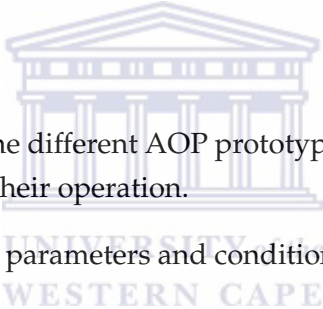
The electrohydraulic discharge processes which produce UV irradiation based on various electrodes configurations have been studied for several years. However, the integration of innovation in nanotechnology into the electrohydraulic discharge process has received

little attention. The reason was in connection with the problems associated with the use of nanometric photocatalysts. The problems include the separation of catalyst particles from the suspension after photocatalysis and the possibility of aggregation of the suspended particles. Therefore, there is a need to design a prototype AOP reactor in a particular way for generating a permanent source of UV irradiation and also a clear need to immobilise the high surface area, nanostructured photocatalyst on a solid supporting material that would not disintegrate over time in a free-radical rich environment. The composite supported anatase form of TiO_2 should be stable to prevent release of particles of TiO_2 into the water and the composite form would thus be relatively simple to remove from treated water.

1.3 The aims and objectives of the current research

The aim of this study was to design and build an electrohydraulic discharge reactor in such a way that the synthetic immobilized TiO_2 nanophotocatalytic components could be integrated, for the production of active species such as OH radicals, ozone and hydrogen peroxide, as a cocktail to clean drinking water without the addition of chemicals.

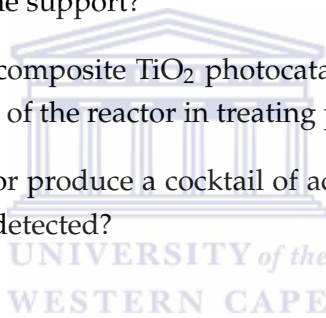
The research objectives include:

- 
- To design and construct the different AOP prototypes based on various electrode configurations and compare their operation.
 - To optimize the discharge parameters and conditions of the best AOP system.
 - To determine the effectiveness of the best prototype for the degradation of methylene blue as model pollutant.
 - To compare the designed AOP system with the Sodis method for the disinfection of contaminated river water.
 - To prepare supported TiO_2 nanoparticles via electro spinning, followed by combustion and study the effect on the morphology of TiO_2 nanoparticles.
 - To determine the stability and robustness of composite nano-crystalline TiO_2 photocatalysts by sonication
 - To determine the enhanced effect of combining the composite TiO_2 in the AOP system on degradation of methylene blue under the same conditions.
 - To detect the active species promoting disinfection.

1.4 Research questions

The questions that need to be addressed by this research are:

- Which prototype design to build, based on corona discharge, to build and what geometry of the electrodes generates better plasma directly in water?
- What are the parameters and conditions that should be optimized for the most efficient prototype design, which leads to the formation of permanent UV light?
- Can the AOP prototype reactor by itself be effective in the degradation of dyes and kill *E.coli* in drinking water?
- Does the multi-electrode system reduce the discharge load on each electrode to prevent the corrosion of electrodes?
- Is the electrospinning method going to be suitable for the synthesis of new TiO₂ nanofibres?
- Is the supported TiO₂ nanofibre effective for photocatalytic activity?
- How can electrospun TiO₂ nanofibres be immobilized and utilized in an AOP reactor without degradation of the support?
- Can the integration of a composite TiO₂ photocatalyst in the AOP prototype reactor improve the effectiveness of the reactor in treating polluted water?
- Does the prototype reactor produce a cocktail of active species from water ionisation and can these species be detected?



1.5 Hypothesis

In order to answer these questions, a number of hypotheses based on the literature review were developed and investigated in this thesis. These include:

- An optimized design of an AOP reactor, which is based on corona discharge, can produce a cocktail of active species that attack micro-organisms in polluted water.
- The multiple electrodes in the system can provide several sources of active species along the water flow path, and thus maximize micro-organism exposure and eventual rapid decomposition.
- The preparation and synthesis of composite TiO₂ nanoparticles on stable support materials, using an electrospinning technique followed by combustion, will prevent the release of TiO₂ nanoparticles in the disinfected water.
- The integration of nanocrystals of TiO₂ immobilized on support material in the AOP reactor can reduce the energy consumption of the system, increase the lifetime of the reactor, enhance the cocktail of active species and overcome the particle separation problem from the treated water.

1.6 Research approach

In order to achieve the above mentioned aims and objectives of this study, the research was designed in a sequential manner as indicated in Figure 1.1 below. The designed reactor was based on the corona discharge principle as stipulated: "A high voltage alternating current between two electrodes, which are separated by a layer of dielectric material and a narrow gap through which the oxygen bearing gas is passed". Different prototypes were designed and tested by applying a high voltage over different electrodes configurations, in order to generate the plasma. The plasma, a gas of charged and neutral particles, then initiated water splitting to cause physical effects such as a high electric field, intense UV radiation and chemical effects such as the generation of ozone, hydrogen peroxide and OH radicals. Moreover, the UV irradiation produced during the discharge process was also used as a way to apply a photocatalyst to enhance active species production, in order to reduce the time of exposure and therefore increase the efficiency of electrical disinfection. Composite TiO₂ in nano-crystalline form was obtained using an electrospinning technique via the sol-gel method, followed by combustion. This was then integrated into the UV production reactor for the photocatalysis process. Finally the synergetic physical and chemical effects were applied to the total disinfection or degradation of microbes and organics respectively.

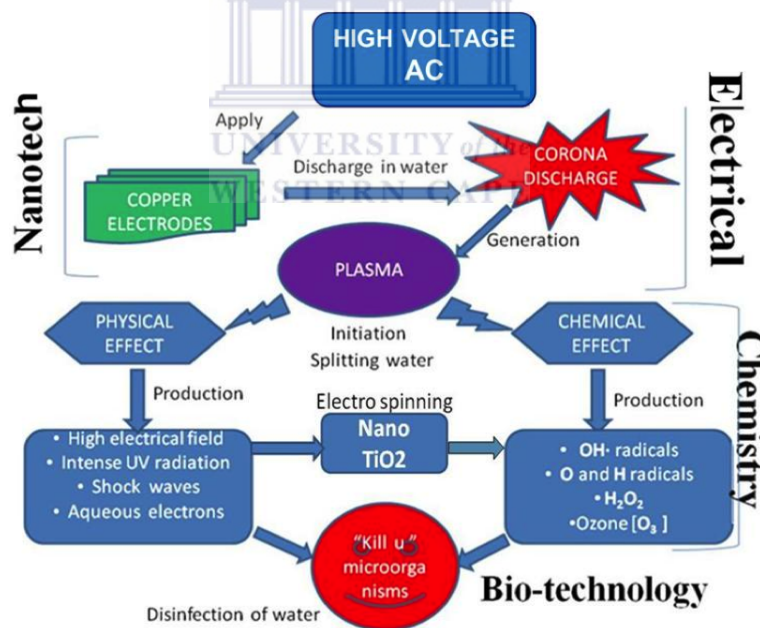


Figure 1.1: Summary of the research approach of this study

The electrospun TiO₂ nanofibres, supported on a stainless steel grid, were transformed at various temperatures (400°C, 500°C, and 600°C) to produce supported TiO₂ nanoparticles by using calcination, combustion and inert combustion methods. The unsupported electrospun nanofibres and supported composite TiO₂ nano-crystalline were then compared and characterized using Fourier Transform Infrared Spectroscopy (FTIR), X-ray diffraction

(XRD), Scanning Electron Microscopy (SEM), Transmission Electron Microscopy (TEM), Energy Dispersive Spectroscopy (EDS), Selected Areas Electron Diffraction (SAED), and Brunauer-Emmett-Teller (BET) Surface Area analysis.

The electrohydraulic discharge reactor was used to compare the photocatalytic activity of supported TiO₂ nanoparticles with unsupported TiO₂ electrospun fibres, using the UV-irradiation light from the reactor as the source of energy.

Methylene blue and *E.coli* were used as model pollutants in the water to be treated. The cocktail generated during AOP was characterized and shown to be constituted of active species. The OH radicals were detected using an Electron Spin Resonance (ESR) method, ozone using the iodometric method, and hydrogen peroxide using the colorimetric method with titanyl ions.

1.7 Scope and delimitations of the study

The scope of this thesis was to design and build a suitable reactor that is based on corona discharge, initiating a plasma in water for the production of a cocktail of active species, such as OH radicals, O₃, H₂O₂, O atomic or super oxide. These active species were expected to target and attack micro-organisms or organic compounds in the water without secondary effects, because of their short life time. For the purpose of this thesis a reactor with the specific geometry of electrodes in horizontal position inside the water flow path was used to generate a corona discharge and UV light in water. The study of the processes initiated by the discharge in water focused on the production of OH radicals, hydrogen peroxide, ozone and ultraviolet radiation. Moreover, the permanent UV irradiation produced from the reactor offered the opportunity of improving the system by integrating composite TiO₂ nanocrystals, immobilized on a support substrate, for photocatalysis, in order to promote the generation of more active species and to contribute to lower energy consumption. The effects of the physicochemical parameters (pH, conductivity of the water, additives), discharge conditions (applied voltage polarity and peak value) and the effect of different gases (air, pure oxygen and argon) on UV-light production were investigated in this study. methylene blue and *E.coli* were used as model organic compounds and microbes for the investigation of the corona induced degradation and inactivation processes, respectively. The key parts of this study are the optimal degradation of dyes, removal efficiency of microbes and the detection of active species as killing factors. In addition, the comparison between the reactor (new design based on corona discharge process) and a solar disinfection system was considered in this study.

The conversion of anatase phase (more photocatalytically active) to rutile was found to occur at temperatures above 600°C (Sotter et al., 2005; Miki et al., 2009). Thus, to ensure that part of the TiO₂ was in the anatase phase, a maximum annealing temperature of 600°C was used. The limitations of this study were that temperatures beyond 600°C were not applied, the quantification of active species was not done, but only their detection as proof of concept, ZnO₂ was not explored as photocatalyst, only *E.coli* was investigated as emerging pollutant,

and model dyes other than Methylene blue, such as Rhodamine blue and acid orange, were not used in in-depth studies.

1.8 Layout of thesis chapters

This thesis is organized into six chapters. Apart from the introduction, which constitutes the first chapter, the following overview presents the structure of the present thesis and some attached annexes, which will constitute the final part of the study.

Chapter 2 is the literature review that covers the advanced oxidation methods for disinfection. Topics reviewed include electrical discharge in water, the photocatalysis process, TiO_2 as catalyst, electrospinning, calcination and carbonization.

Chapter 3 presents a short description of the research design, detailed description of the experimental procedures and instrumental setups used in the present research work. The methodologies, materials, equipment used, preparation of solutions, synthesis of the TiO_2 nanofibres and the characterization procedures are also detailed.

Chapter 4 presents the design approach and the development of different AOP prototypes, as well as the results and comparative discussion of degradation of methylene blue as model pollutant dye, using different prototypes (OK-1, OK-2 and OK-3).

Chapter 5 describes the methods used to synthesize TiO_2 nanoparticles and the results of immobilization of TiO_2 containing electro-spun nanofibres, their characterization, the outcomes and discussions with comparison to commercial Degussa (P-25) TiO_2 nanoparticles. This chapter presents the characteristic results of the new composite TiO_2 nanocrystals, supported on stainless steel mesh. Different results for the characterization techniques, such as XRD, BET, FTIR, SEM, SAED, HRTEM, and EDS are presented. The chapter also presents results of studies conducted by the incorporation of the new composite TiO_2 nano-crystals in the reactor, compared with P-25 Degussa as baseline for investigating the potential to produce clean water. Finally, the detection of the active species, such as OH radicals, ozone and hydrogen peroxide, that are responsible for the degradation of organics and inactivation of micro-organisms in the water is presented.

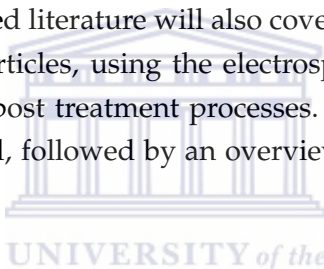
Chapter 6 presents the conclusions that can be drawn from the study and the recommendations of future work related to the study carried out. This final chapter will summarize the work and answer the research questions.

Appendices include different comparison tables of AOP, different disinfection methods and new prototype designs.

Chapter 2

Literature review

This chapter presents an overview of advanced oxidation processes for water disinfection, since they are the main techniques for the production of active species used as cocktail in this study. Thereafter, the general aspects of electrical discharge in water are broadly discussed with respect to the electrode geometry, prior to an in-depth discussion of different prototype designs. The reviewed literature will also cover various aspects of photocatalysis and immobilisation of nanoparticles, using the electrospinning technique for water treatment, in order to avoid extra post treatment processes. Different synthesis procedures of nanofibres are then highlighted, followed by an overview of applications of nanofibres for water treatment.



2.1 Advanced oxidation processes (AOP)

Advanced oxidation processes have been defined as water treatment processes that involve an input of energy (either chemical, electrical or radiative) into the water matrix to produce highly reactive radical intermediates, which then attack and destroy the target compound(s). Most advanced oxidation processes for water and wastewater treatment are based on the generation of hydroxyl radicals to initiate an oxidation reaction. A concise description is presented by Prousek (1996) and Carrey (1992) for major advanced oxidation processes. Advances in chemical water and wastewater treatment have led to the development of a range of processes termed as advanced oxidation processes (AOPs). The suitability of AOPs for aqueous pollutant degradation was recognized in the early 1970s and much research and development work has been undertaken to commercialise some of these processes (Rodriguez et al., 2003). The use of AOPs is a concept in the treatment of industrial and domestic drinking water, which has gained increasing interest. This process involves the use of hydroxyl radicals to remove organic and inorganic contaminants. The common goal of many groups working worldwide is to increase the number of applications of these processes and to improve the efficiency. The main interesting characteristics of hydroxyl radicals are their very high oxidation potential (2.8 V) and the fact that they exhibit faster oxidation reaction rates to target various pollutants of interest, compared to conventional oxidant such as hydrogen peroxide (1.8V) and chlorine (1.36V) (Gogate and Pandit, 2004). The hydroxyl radicals are

also non-selective oxidants with a short-life time and no by-products. Therefore, OH radicals can be detected indirectly using scavengers such as methanol and bicarbonate. There are different ways and possibilities to generate OH radicals as described in Sections 2.1.1 to 2.1.7 (Munter et al., 2001).

2.1.1 Anodic oxidation

In an electrochemical treatment, organic compounds can be destroyed through different routes: oxidized indirectly or directly by the anodes (Beltran et al., 1994). An indirect anodic process, via the production of oxidants such as hydroxyl radicals and ozone amongst others, destroys the organics and toxic microbiological pollutants present in wastewater. A direct anodic process is one in which the pollutants are first adsorbed on the anode surface and then oxidized by an electron, as described in Figure 2.1

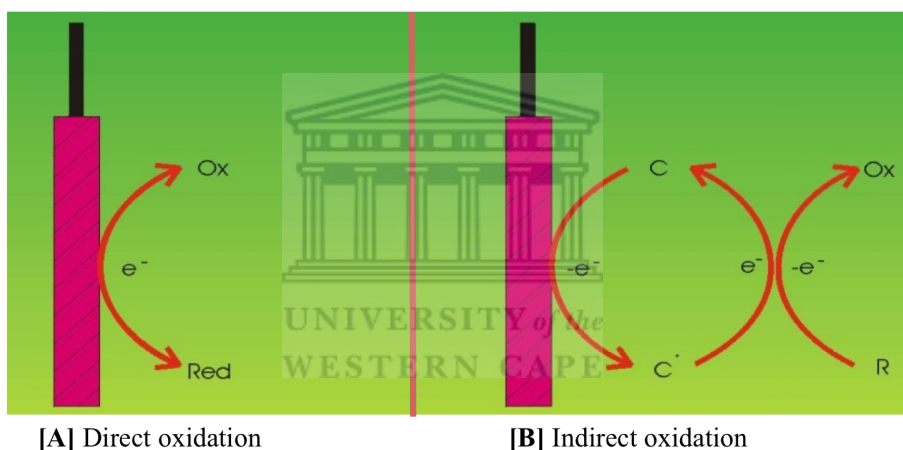


Figure 2.1: Electron-transfer scheme for anodic oxidation processes: [A] Direct oxidation, and [B] indirect oxidation

Electrochemical oxidation of pollutants can occur directly at anodes through the generation of physically adsorbed "active oxygen" (adsorbed hydroxyl radicals) or chemisorbed "active oxygen" (oxygen in the oxides lattice, MO_{x+1}). This process is usually called "anodic oxidation" or "direct oxidation" (Comnimellis et al., 1999). Among the main problems encountered with direct oxidation is the large number of electrons required for the complete oxidation (that is, all the way to carbon dioxide) as well as the large variety of reaction intermediates.

Concerning the indirect oxidation, the most used electrochemical oxidant is probably chlorine, or hypochlorite. In addition, peroxide, Fenton's reagent, peroxodisulphate and ozone are well-known oxidants that can also be electrochemically produced (Nakajima et al., 2005).

2.1.2 Ozone oxidation

The most established way to generate ozone is through corona-discharge, ozone being created when the air flows through the discharge gap between two electrodes which are separated by a dielectric material. At the heart of a corona discharge ozone system is the dielectric, which has the role of establishing the electrical fields between the high voltage and the ground electrode. The electrical charge is diffused over this dielectric surface, creating an electrical field, or "corona", which splits oxygen molecules to form ozone, as shown in Figure 2.2.

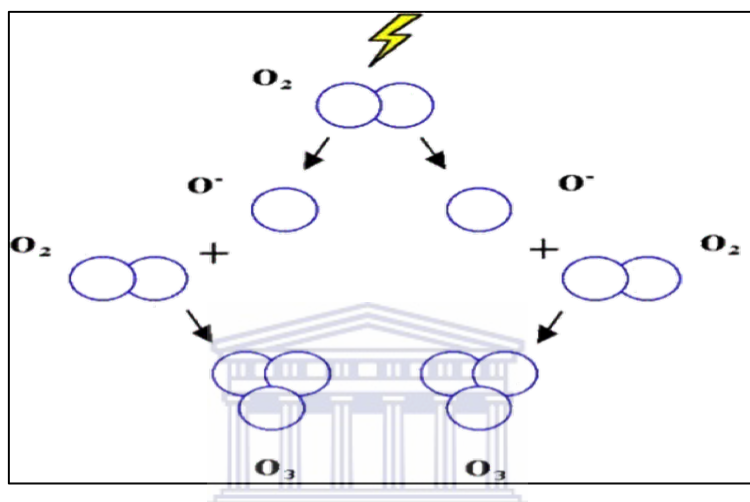


Figure 2.2: Schematic of the splitting of oxygen molecules by an electric field to form ozone (Hoigne et al., 1976)

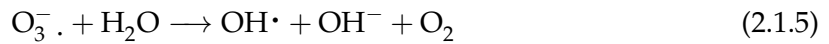
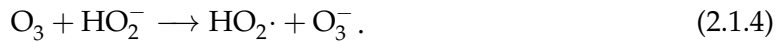
Ozone is a powerful oxidant, second only to the hydroxyl radical. Therefore, it can oxidize organic matter in water, either directly or through the hydroxyl radicals produced during the decomposition of ozone. Direct oxidation with molecular ozone is of primary importance under acidic conditions. However, it is a relatively slow process compared to hydroxyl free radical oxidation. In neutral and basic solutions, ozone is unstable and decomposes via a series of chain reactions to produce hydroxyl radicals, as shown in Equation (2.1.1) (Andreozzi et al., 1999):



The added hydrogen peroxide or ultraviolet radiation accelerates the decomposition of ozone and increases the hydroxyl radical concentration. Also, the presence of suspensions of activated carbon might be able to stimulate the production of OH[•] radicals from ozone. For the photolysis of ozone in the 200-280 nm region a two-step process has been proposed involving light induced homolysis of ozone and subsequent production of OH[•] radicals by the reaction of excited oxygen from O(¹D) with water, as shown in Equations (2.1.2) and (2.1.3) (Peyton et al., 1988).



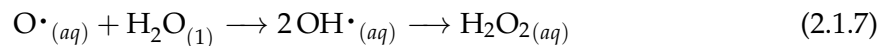
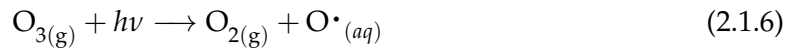
The chemistry involved in the generation of $\text{OH}\cdot$ radicals by the $\text{O}_3/\text{H}_2\text{O}_2$ process (peroxone) is assumed to be mainly through decomposition of ozone by the conjugate base of hydrogen peroxide (HO_2^-) to produce the ozonate radical ($\text{O}_3^- \cdot$) that gives the hydroxyl radical by rapid reaction with water (Staehelin et al., 1982).



This process is further enhanced by the photochemical generation of hydroxyl radicals in the $\text{O}_3/\text{H}_2\text{O}_2/\text{UV}$ process.

2.1.3 UV/ O_3 Process

Three dominant reactions during ultraviolet (UV)/Ozone (O_3) treatment processes that effectively decompose organic pollutants are photolysis, ozonation, and reactions of hydroxyl radicals. The generation of hydroxyl radicals is an essential, transitional reaction that ultimately destroys organic pollutants during the oxidation process. The advanced oxidation process with UV radiation and ozone is initiated by the photolysis of ozone. This process is preceded by the generation of two hydroxyl radicals, which, if they do not react, recombine to produce the hydrogen peroxide, as shown in Equations (2.1.6), (2.1.7) and (2.1.8) (Tominaga et al., 2005).



This system UV/ O_3 can produce hydroxyl radicals, hydrogen peroxide and oxidize the pollutants by attacking the cell wall of microorganisms to cause cell death by rupturing and alteration of proteins.

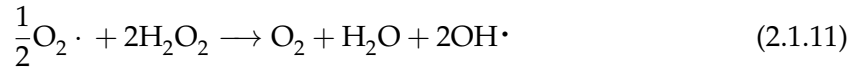
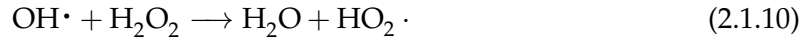
2.1.4 Hydrogen peroxide oxidation

The most commonly used ways for generation of hydroxyl radicals from hydrogen peroxide are through the photolysis of H_2O_2 and Fenton's reaction. The primary process of H_2O_2 photolysis in the 200-300 nm regions is dissociation of H_2O_2 to hydroxyl radicals with a

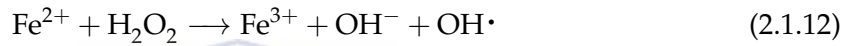
quantum yield of two $\text{OH}\cdot$ radicals formed per quantum of radiation absorbed (Staehelin et al., 1982), as expressed by



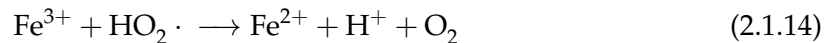
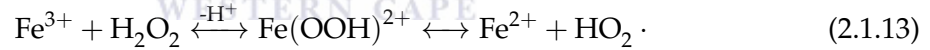
The $\text{OH}\cdot$ radicals thus formed enter a radical chain mechanism in which the propagation cycle gives a high quantum yield of the photolysis of H_2O_2 , as shown in Equation (2.1.10).



Fenton-type catalyzed generation of hydroxyl radicals is based on the decomposition of hydrogen peroxide by ferrous ions (Walling et al., 1975), which is shown in Equation (2.1.12) as



This method is very effective for generating hydroxyl radicals, but involves consumption of one molecule of Fe^{2+} for each hydroxyl radical produced. The decomposition of hydrogen peroxide is also catalyzed by ferric ions. In this process, H_2O_2 is decomposed to H_2O and O_2 and a steady-state concentration of ferrous ions is maintained during peroxide decomposition:



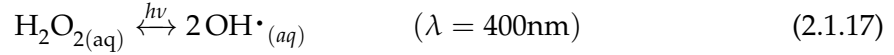
The ferric system, known as the Fenton-like reagent, is attractive, because degradation of organics can be catalytic over iron. However, the initial rate of destruction of organic pollutants by the $\text{Fe}(\text{III})/\text{H}_2\text{O}_2$ is much slower than that of the $\text{Fe}(\text{II})/\text{H}_2\text{O}_2$ due to the lower reactivity of ferric ions toward hydrogen peroxide. The oxidizing power of the Fenton-type systems can be greatly enhanced by irradiation with UV or UV-visible light due to the photoreduction of hydroxylated ferric ion in aqueous solution (Pignatello et al., 1992), as shown in Equations (2.1.15) and (2.1.16).



The combined process, as described by Equations (2.1.13), (2.1.15) and (2.1.16), is known as the photo-Fenton reaction, and results in increased production of $\text{OH}\cdot$ radicals and more importantly, iron is cycled between the +2 and +3 oxidation states, so $\text{Fe}(\text{II})$ is not depleted, and $\text{OH}\cdot$ production is limited only by the availability of light and H_2O_2 .

2.1.5 H₂O₂/UV Process

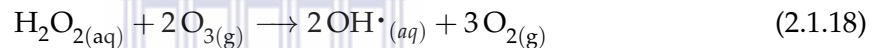
The H₂O₂/UV system involves the formation of hydroxyl radicals by hydrogen peroxide photolysis, as shown by Equation (2.1.17) below.



This equation presents the advantages of working with peroxide, since it provides a cheap and sure source of radicals and eliminates the problem of the handling of chlorine. The major drawback of this process is that strongly absorbing substances can compete with hydrogen peroxide for the radiation. Thus, a solution that is cloudy and containing compounds that can absorb UV radiation, can present problems in this method (Heredia et al., 2001).

2.1.6 O₃/H₂O₂ Process

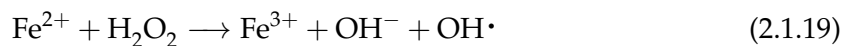
Addition of hydrogen peroxide to ozone offers another way to accelerate the decomposition of ozone, leading to the formation of hydroxyl radicals. The reaction of this process is illustrated in Equation (2.1.18):



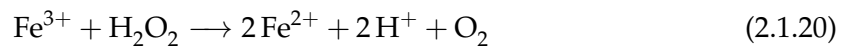
This process does not depend on the UV radiation absorption to activate the ozone or hydrogen peroxide molecules and can be applied to turbid water without problems (Masayoshi et al., 2007).

2.1.7 Fenton's reaction process

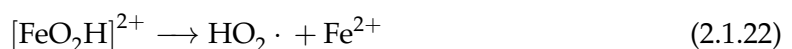
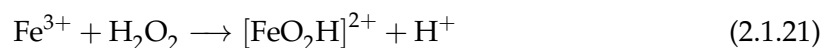
The "Fenton reaction" is one of the most severe oxidizing reactions available. The reaction involves hydrogen peroxide and a ferrous iron catalyst. The H₂O₂ is broken down into a hydroxide ion and hydroxyl free radical. The OH radical is the primary oxidizing species and can be used to oxidize and break apart organic molecules (Pignatello et al., 2007).

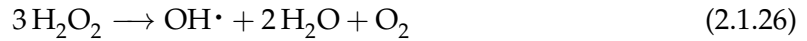
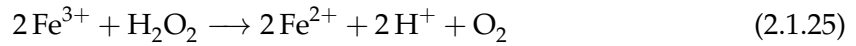
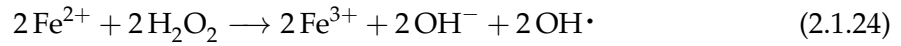
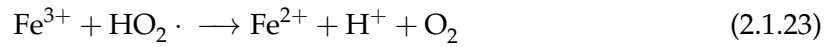


Under these conditions, it is considered that the following reaction also occurs:



The reaction above proceeds via the following intermediate steps:





Hydrogen peroxide is thus decomposed using $\text{Fe}^{2+}/\text{Fe}^{3+}$ as a catalyst (Mangombo et al., 2006).

There is evidence for the production of the hydroxyl radical ($\text{OH}\cdot$) as an intermediate to the oxygen and hydrogen evolution, looking at the different chemistry reactions of Advanced Oxidation Process (AOP), as summarized in Figure 2.3. The hydroxyl radical ($\text{OH}\cdot$) is a highly reactive, short-lived species that can rapidly oxidize most organic compounds in water.

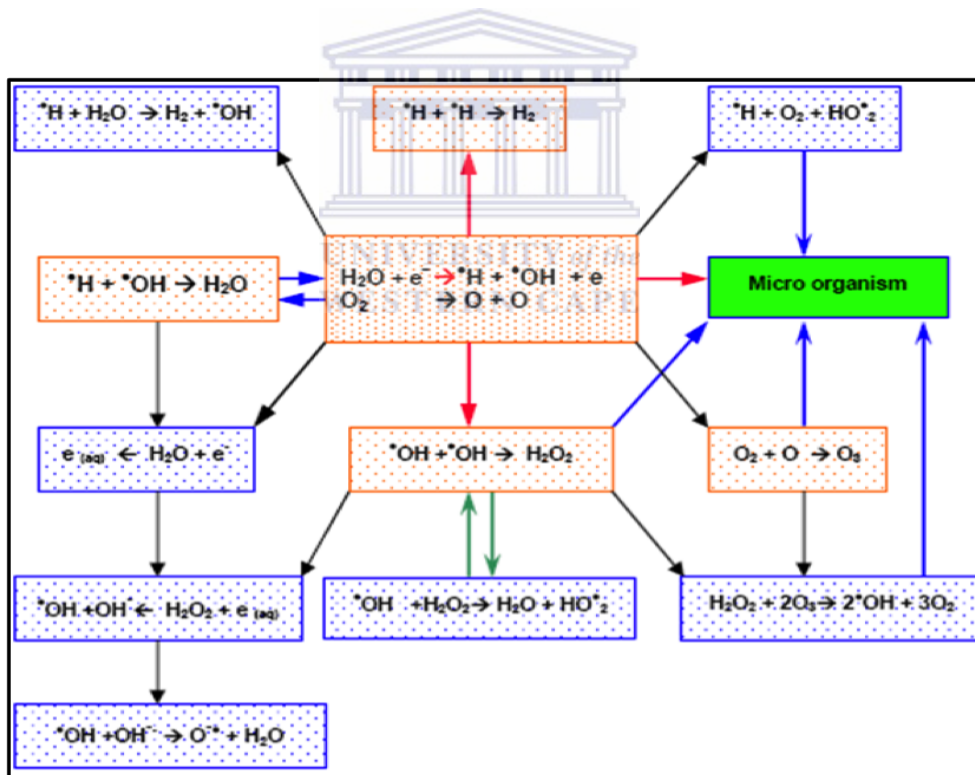


Figure 2.3: Major chemical reaction paths leading to the production of oxidants with outcome in corona discharges. (Blue dots represent reactions taking place in the bulk solution; red dots show reactions occurring at the interface and inside the plasma channel) (Glaze et al., 1994)

2.2 Electrical discharge in water

2.2.1 Introduction

Fundamentals of electrical discharges in water are briefly reviewed with regard to the types of electrical discharges used for water treatment, the principle of breakdown phenomena in the liquid, and the physical and chemical processes initiated by the electrical discharge in water.

2.2.2 Corona discharge

A corona can be observed in the air around high voltage transmission lines and around lightning rods, where it is called "Saint Elmo's fire". The corona can be ignited with a relatively high voltage, which mainly occupies the region around one electrode. The corona is a weakly luminous discharge, which usually appears at atmospheric pressure near sharp point edges or thin wires, where the electric field is sufficiently large. The image in Figure 2.4 presents the natural corona discharge occurring during a lightning strike.



Figure 2.4: Lightning type of natural corona discharge (Lisitsyn et al., 1999)

Corona discharges are always non-uniform, and a strong electric field, ionization and luminosity are actually located in the surrounding area of one electrode. Charged particles are dragged by the weak electric field from one electrode to another to close the electric circuit. However, at this stage, the breakdown circuit in the corona discharge is closed by a displacement current, rather than charged particle transport (Lisitsyn et al., 1999).

2.2.3 Types of electrical discharges for water treatment

There are various types of electrical discharges generated, either directly in water or above the water surface, that have been investigated as possible methods for water treatment. Consequently, a large variety of reactors and electrode configurations have been used. Alternating current (AC), direct current (DC) and pulsed electric fields have been applied in

conditions where the electrodes have been fully immersed in the liquid phase, and where one electrode has been placed in an adjacent gas phase, and/or where arcing across the electrodes may occur (Goheen et al., 1992).

2.2.3.1 Electrical discharges above the water surface

Among the types of electrical discharges above the water level, glow discharge electrolysis and the related contact glow discharge electrolysis are methods of electrochemical generation of plasmas used for water treatment. In glow discharge electrolysis (Hickling et al., 1952), operated under reduced pressure, a DC high voltage electrode is placed above the surface of an electrolyte, as shown in Figure 2.5, and the glow discharge is established between the high voltage electrode and electrolyte surface, in water vapour, formed at the gas-liquid interface, under low pressure conditions.

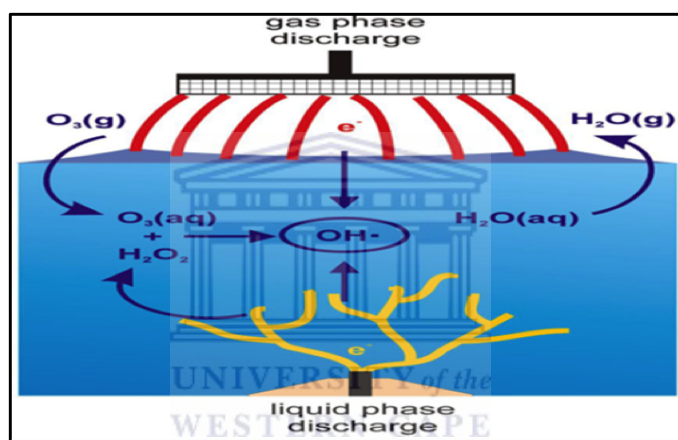


Figure 2.5: Electrical discharge above the surface of wastewater (Sengupta et al., 1997)

In contact glow discharge electrolysis, a thin wire electrode is in contact with the surface of the electrolyte and the DC glow discharge is initiated in a thin vapour film covering the electrode surface, even at atmospheric pressure. It was suggested that the gaseous jacket over an electrode is caused by a film of solvent, vaporized locally due to Joule heating (Sengupta et al., 1997). Elements in such a plasma are electrolytically dissociated at a high temperature and thus differ considerably from elements in electrochemical systems at room temperature. This situation sometimes results in the formation of reaction products (H_2O_2 , H_2 , and O_2) with non-Faraday efficiency.

The glow discharge electrolysis was interpreted by the primary formation of the H_2O^+ ions from vapor H_2O molecules in the gas phase. These H_2O^+ ions bombard the surface of the gas-liquid interface under the influence of the large electric field driving force, which then react with liquid H_2O molecules to form $\text{OH}\cdot$ and $\text{H}\cdot$ radicals. As a mixture of the active species, $\text{OH}\cdot$, $\text{H}\cdot$ and H_2O^+ diffuse out from the gas-liquid interface and into the bulk electrolyte through the action of the electric field. They can interact among themselves or with any active substrate in the solution (Sengupta et al., 1998). In general, strong oxidative

reagents, such as $\text{OH}\cdot$ radicals, O atoms and their reaction products (O_3 , H_2O_2 etc.), can be produced in the gas-liquid interface and can initiate reactions in the water.

2.2.3.2 Electrical discharges occurring deeper in water

In the cases where both high voltage and ground electrodes are placed in the liquid phase, point to plane geometry has most typically been studied for pulsed discharges, where the needle, used as point electrode, is connected to the high voltage and the plane is earthed. When a pulsed high voltage (positive or negative polarity) is applied to the point, small white spots (micro discharges) are initially formed at the tip. The white spots are surrounded by a thin magenta layer, which consists of very short streamers.

As the voltage is increased, the streamer becomes larger and filamentary. This is called "pulsed streamer corona", or "corona-like" discharge. A further increase of the voltage leads to spark-over, whenever one of the streamers contacts the plate electrode. The streamer is transformed into a high-current arc, discharge proceeds from the streamer corona discharge stage to spark discharge. Lukes et al., (2001) conducted the first extensive analysis of both chemical and physical factors that occur in pulsed streamer corona discharges in water, with a point to plane electrode configuration, with and without the combination of various gases bubbled through the high voltage electrode. Emission spectroscopy was used to show the production of significant quantities of hydrogen radicals in the liquid phase and, by chemical means, the formation of ozone when air or oxygen was bubbled through a hollow electrode needle immersed in the water. They also reported indigo and antraquinone dye bleaching with this setup.

Subsequently, a number of investigators have also used the same point to plane electrode system for underwater pulsed discharge experiments, either in the streamer, spark or mixed streamer spark mode (Sugiarto et al., 2001). It has been demonstrated that pulsed streamer corona discharge produces various reactive chemical species such as radicals ($\text{OH}\cdot$, $\text{H}\cdot$, $\text{O}\cdot$, $\text{HO}_2\cdot$) and molecular species (H_2O_2 , H_2 , O_2). In the case of spark discharge, higher radical emission intensities and hydrogen peroxide concentration were obtained than in streamer corona discharge, when the energy input was the same. In addition, intense ultraviolet radiation and overpressure shock waves were generated by the spark discharge.

A special metallic electrode covered by a thin layer of porous ceramic was developed in order to generate a multichannel discharge and to overcome some of the problems associated with point to plane geometry, including the increasing volume of the plasma discharge active region, and reducing the problem of needle tip wear (Clupek et al., 1998). The role of the ceramic layer is to enhance the electric field on the anode surface by concentration of the pre-discharge current in small open pores. Many discharge channels, distributed almost homogeneously along the whole surface of the composite electrode, can be generated during each voltage pulse. The composite electrode can be made in various forms and dimensions, enabling the construction of reactors of different geometrical configurations (e.g. wire-cylinder or planar) with various discharge volumes and power (up to kW level). Results of optical spectroscopy demonstrated that plasma, with spectral features very similar

to those measured in the reactor with point to plane electrode geometry, was produced. It was observed that the composition of the used ceramic had a significant effect on the H_2O_2 production. Consequently, it was shown that, at very high solution conductivity (0.5–1.5 S/m), the multichannel discharge with the composite electrode generated strong acoustic waves (Sunka et al., 2001).

Other researchers (Akiyama et al., 2000) have developed a liquid phase pulsed electrical discharge reactor with a ring to cylinder electrode configuration. In this system the ring electrode is shaped and insulated up to the very edge and placed coaxially at the centre of an outer cylinder grounded electrode. Streamer corona or spark discharge can be formed from the edge of the ring electrode and can propagate to the outer ground cylinder electrode. As in the point to plane geometry, the protrusion length of the ring electrode from the insulator surface affects the initiation voltage of the streamer discharge. However, the ring to cylinder type is considered to be suitable for scaling up the reactor, through stacking multiple rings in series down the reactor, therefore leading to a larger plasma region. The formation of $\text{OH}\cdot$ and $\text{H}\cdot$ radicals in this system was proven by emission spectroscopy, and production of hydrogen peroxide was determined by the colorimetric method (Sugiarto et al., 2000). Another electrode configuration used in liquid phase corona discharge, is the "pinhole" geometry, also called a diaphragm discharge. In such a type of discharge, the plasma starts to be generated in small holes made in an insulating plate, separating the high voltage and ground electrodes.

The pre-discharge current is concentrated in the hole and leads to strong thermal effects, causing bubble formation and breakdown. Pulsed streamer discharge occurs at the pinhole, because of the very high field in the pinhole. In the case of a multiple pinhole system, discharges are formed regularly through all holes, and directed towards both electrodes. The streamer length varies with the electrical conductivity of the solution, the flow rate of the water through the pinhole and the voltage polarity of the applied pulse. Shorter streamers are formed on the positively charged electrode side, rather than on the negative electrode side. Generation of plasma with similar parameters to the streamer discharge in configuration point to plane in positive and negative polarity in sheet-electrode gap, respectively, is expected. A potential advantage of such a discharge would be the possibility of pumping the treated water through the active discharge volume (Sugiarto et al., 2000). A pulseless corona discharge, produced by strong DC fields between capillary point and ground electrodes, submerged in water, has been investigated by (Shin et al., 2000). The method combines corona discharge with electro hydrodynamic spraying of oxygen through the capillary. It has been demonstrated that such a system leads to the formation of the same chemically active species as was the case with the pulsed streamer corona discharge process. Emission spectra results showed that the major radical species from the process were hydroxyl radicals, ozone and atomic hydrogen. However, based on modeling results, it was inferred that the dominant species for the pulseless corona discharge system are hydroxyl radicals and aqueous electrons, as opposed to hydrogen peroxide for the pulsed streamer corona system. Consequently, the pulseless corona method was shown to be comparable to the direct use of ozone at a high applied voltage.

The so-called electrohydraulic discharge technique, i.e. high voltage/high current spark discharges between two submerged electrodes in water, has been extensively studied (Willberg et al., 1996). In such discharges the destruction of pollutants may be initiated simultaneously by pyrolysis in a hot plasma channel, free radical oxidation, UV radiation, supercritical water oxidation and electrohydraulic cavitation. It was observed that the addition of ozone significantly increased the rate and extent of the degradation of the pollutants in the electrohydraulic reactor, due to the formation of $\text{OH}\cdot$ radicals produced by the photolysis of ozone (Lang et al., 1998).

Consequently, multispark electric discharge in water, using a multi-electrode metal-dielectric system with gas supply into the inter-electrode gaps, has been investigated by Anpilov et al. (Anpilov et al., 2001). The system consisted of a set of annular electrodes, mounted on a dielectric tube with holes between electrodes, through which a gas (air, argon, and oxygen) is injected into water, in order to facilitate breakdown in the inter-electrode gaps. Thus, the origin of the plasma channel created between electrodes is located in a gas bubble in which the electric field increases above the gas-breakdown threshold. It was demonstrated that the multi-spark electric discharge system produced significant amount of H_2O_2 , ozone and ultraviolet radiation. (Anpilov et al., 2001)

2.2.3.3 Electrohydraulic discharge for water treatment

Electrohydraulic discharge (ED) is the application of strong electric fields to water, and one aspect of this relatively mature field of study is water treatment. Primarily ED can be characterized by the amount of energy used per pulse, where corona or non-thermal plasma discharges use ~ 1 J/pulse, and more energy intensive discharges, arc or plasma, use ~ 1 kJ/pulse. Although useful in some regards, these two limits should only be used as a guide, since a large amount of literature falls within the ranges specified, and it is more useful to look at the active species formed and other mechanisms of degradation associated with the energy used (Locke et al., 2006). Several factors must be considered when using strong electrical fields in water treatment. Specifically, the generation of active chemical species, shock waves, UV radiation, and cavitations. Some of these effects, due to the discharge parameters used, are summarized in Table 2.1.

Besides the discharge parameters, the electrode geometry and configuration plays an important role in the overall characteristics of discharge effects with water, along with the use of AC versus DC, pulse and frequency. Some excellent reviews on electrical discharges are available in the literature (Locke et al., 2006). However, important information relevant to this study is summarized below.

Table 2.1: Some characteristic of electrical discharges in water (Locke et al., 2006)

Parameter	Value	
	Pulsed corona	Pulsed arc
Operating frequency	10^2 – 10^3 Hz	10^{-2} – 10^{-4} Hz
Current (peak)	10 – 10^2 A	10^3 – 10^4 A
Voltage (peak)	10^4 – 10^6 AV	10^3 – 10^4 V
Voltage rise	10^{-7} – 10^{-9} s	10^{-5} – 10^{-6} s
Pressure wave generation	Weak to moderate	Strong
UV generation	Weak to moderate	Strong

2.2.3.4 Electrode and Electrical Parameters in Electrohydraulic Discharges

There are numerous configurations regarding the placement of the electrodes, types of electrodes, and reactor design that have been studied, and a summary of the more common configurations is presented in Figure 2.6 below. A more detailed list and description can be found in the literature (Gupta and Bluhm, 2007),(Locke et al., 2006). However, a brief overview is given below. Each configuration in Figure 2.6 can consist of two or more variations. Specifically, one or both electrodes can be in the water, an electrode or a separate distributor can be used to supply additional gas (air or oxygen), the electrodes can be placed horizontally, or both electrodes above the water. From these diagrams, it is possible to design various unique systems, incorporating fixed or fluidized bed catalysts for investigation of synergistic effects of nanoparticles in the system.

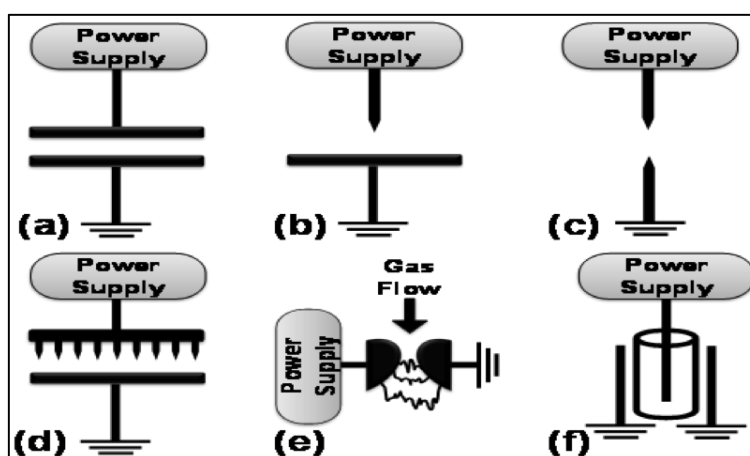


Figure 2.6: Simplified illustration of some possible different electrode configurations for electrical discharges in water; (a) two plane electrodes, (b) a plane electrode and a needle electrode, (c) two needle electrodes, (d) a plane electrode with a multi-needle electrode, (e) gliding arc electrodes, and (f) coaxial reactor configuration

The different configurations are motivated by discipline. For example, the point to point (2-6 (c)), point to plane (2-6(b)), or plane to plane with a pinhole (2-6(a) variant), utilizing kV voltages and very short pulses were typically found in the physics and electrical engineering literature. Thus, it is not surprising that these studies were more concerned with dielectric breakdown effects i.e. physical effects. In contrast, some of the configurations have been developed as a result of electrolysis research (Locke et al., 2006).

Irrespective of the electrode configuration utilized, the physical and chemical processes must be ascertained. Electrical discharges in water can initiate from one electrode with the discharge current partially travelling i.e. it does not reach the counter electrode. These partial electrical discharges can be described as corona like, possess very little current, and can form non-thermal plasmas. With sufficient conductivity in the solution, a greater power density can be achieved, resulting in plasmas with greater densities, and generation of acoustic waves (Locke et al., 2006). It should be noted that the use of nanowire electrodes in a plasma discharge system may result in plasma densities between non-thermal and thermal plasmas, due to the intense electric fields on the nanowires.

Arc and spark discharges can produce plasmas with temperatures $> 10\,000$ K. These systems use high kV power supplies (power supply engineering is key to the successful use of such systems). The high energy plasmas generated by the arc usually generate UV, and strong shock waves (Gupta and Bluhm, 2007), (Locke et al., 2006). In terms of chemical processes, various radicals and reactive species can form, such as OH, H₂O₂, O₃, O, etc. Measurement and detection of these species are extremely difficult, due to their short lifetimes (Gupta and Bluhm, 2007), (Locke et al., 2006).

2.2.4 Propagation of pulsed electrical discharges in water

Breakdown phenomena in liquids have been studied for a long time, in particular its relation to electric insulation (Barmann et al., 1996). However, the detailed mechanism of the initiation of the liquid phase discharges is still not fully understood compared to the understanding of the gas phase discharges for which very detailed one-, two- and three-dimensional streamer propagation models, coupled with ionization and chemical processes occurring in the streamers, have been developed (Nasser et al., 1971). Such differences between the understanding of the liquid phase and that of the gas phase discharge are mainly caused by the substantially higher density of the liquid, leading to a much higher collision frequency and lower mobility of charges, as the mobility of ions is much less than that of electrons (Joshi et al., 1995).

In addition, water is a highly polar liquid with large electrical permittivity and specific conductivity. Water molecules, having a dipole moment, are oriented along the applied pulse electric field, resulting in the generation of electrostriction pressure waves, which create inhomogeneity in density near the high voltage electrode. Consequently, ions present in the liquid strongly alter the propagation of the streamer by compensating for the space charge electric field on the streamer head (Yangzong et al., 2007). In general, two types of theories, i.e. electronic theories and thermal (bubble) theories, have been proposed for liquid

phase discharges (Hayashi et al., 2000).

According to the electronic theories, the free electrons in the discharge gap are accelerated under the influence of the high electric field applied to the needle (in needle-plate reactor) or the wire (in wire-cylinder reactor). The accelerating free electrons may collide with and ionize the ambient molecules, thus producing more free electrons, causing an electron avalanche (streamer or plasma channel) and leading to breakdown in water. Usually a positive DC voltage is applied and in this case the free electrons are attracted towards the high voltage electrode. The drift of free electrons leaves behind a positive charge at the streamer head, which enhances the applied electric field effect and attracts the electron of any secondary avalanche. When secondary avalanche electrons intermix with primary avalanche ions, positive space charge remains in the head of the streamer and greatly enhances the electric field strength at the end of the streamer. This further favours avalanche development, because these positive charges attract the electrons of the next generation of secondary avalanches, and in this way the streamer propagates. Therefore, very long streamer channels can be produced when positive polarity is used. When the polarity of the voltage is reversed, i.e. when the point becomes the cathode, an avalanche starts to develop from the point (strong field region) towards the plate electrode (weak field region). Positive space charge in the primary avalanche channel reduces the electric field strength at the end of the streamer, which is unfavourable to further avalanches development. In this case, the streamer channels are shorter than those for positive polarity (Hayashi et al., 2000). In the thermal theory, it is hypothesized that the current in the high electric field region causes heating and vaporization of the liquid, forming bubbles, and that streamer discharge in water propagates through the bubble in a manner similar to that in the gas phase. The measured resistance of the streamer discharge was found to be much lower than that of the free water and this, coupled with the fact that the streamer velocities in deionized and tap water were equivalent, was taken as evidence for the major role of ionization in the liquid on the pre-breakdown current. Proton mobility in the vapour (but not liquid) phase is sufficient to account for the velocity of streamer propagation. Thus, the physical nature of the streamers is gaseous (Bérroual et al., 1993). However, no published model explains all the experimental results that occur in high voltage pulsed electric discharge in water.

Generally, there is a large difference between the discharge in deionized or distilled water and more conductive water solutions. In addition, the existence of both fast streamers (>1 km/s) and slow streamers (0.1 km/s), and differences between positive and negative polarity streamers propagation velocity, considerably complicate the analysis (Akiyama et al., 2000). An approach, combining both mechanisms of the breakdown of liquids, i.e. electronic and thermal bubble process, has been developed (Bérroual et al., 1993). It is based on the consideration of the energy balance between the input electrical energy and the kinetic energy of streamer displacement. It could establish the relationship between the current and the shape and the velocity of streamers. However, this approach is qualitative and unable to predict the streamer behaviour without exact knowledge of the charge localized at the streamer head. Processes initiated by pulsed electrical discharges in water in general, and the pulsed high voltage discharges in water, generate plasmas that initiate a variety of

physical and chemical effects, such as high electric field, intense ultraviolet radiation, over-pressure shock waves and, especially, formation of various reactive chemical species acting on biological cells and chemical compounds dissolved in water. These effects have various important roles in different application regions in the liquid, and the magnitude of their contributions strongly depends upon the energy of the discharge (Goheen et al., 1992).

2.2.4.1 Pulsed corona discharge for water treatment

Corona discharge is very attractive for different modern industrial applications, such as surface treatment and cleansing of gas and liquid exhaust streams. These discharges are able to generate a high concentration of active atoms and radicals at atmospheric pressure, without heating the gas volume. As shown previously, the application of continuous corona discharge is limited by low currents and, hence, very low power of the discharge, resulting in a low rate of treatment of materials and exhaust streams. Currently, pulsed corona is one of the most promising atmospheric pressure, non-thermal discharge phenomena. For pulsed corona discharge, it is important to make pulsed power supplies, capable of generating sufficiently short voltage pulses with steep front and short rise times (Goryachev et al., 1998).

2.2.4.2 Configurations for electrical corona discharge

The most typical configurations for pulsed corona, as well as continuous corona discharge, involve the use of thin wires, which maximize the active discharge volume. Limitations of the wire configurations for corona are related to the durability of the electrodes and also to the non-optimal interaction of the discharge volume with the incoming gas flow, which is important for plasma-chemical applications. Table 2.2 gives a configuration summary of selected researchers.

With regard to the summary table, it is useful to use a different corona discharge configuration, based on multi stages of pin-to-plate electrodes (Clements et al., 1987). This model is obviously more durable and is able to provide good interaction of the incoming gas stream with the active corona volume formed between the electrodes, which leads to the production of active chemical species responsible to target and kill microorganisms in the water.

Table 2.2: Summary of electrode configurations and actives species production

Authors	Year	Origin	Electrode	Pollutant	Applied voltage	Disinfectant
Anpilov	2004	Russian	Titanium	E. coli	20 kV	O ₃ , H ₂ O ₂ , OH [•] , H [•] , O [•]
Lukes	2004	Czech Republic	RVC and Tungsten wire	N/A	15–30 kV	O ₃ , H ₂ O ₂
Locke and Lukes	2005	USA	RVC and Tungsten wire	Phenol	45 kV	O ₃ , H ₂ O ₂ , OH [•]
Zhang	2007	China	Stainless steel	Methyl orange	46 kV	O ₃ , H ₂ O ₂
Lukes and Sunka	2008	Russian	Porous-ceramic and stainless steel	E. coli	30 kV	H ₂ O ₂ , OH [•]

2.2.4.3 Chemical processes of active species in corona discharge

Pulsed high voltage discharges with kW/pulse power, like pulsed streamer corona discharge, are effective for the production of various reactive chemical species, such as radicals (OH[•], H[•], O[•], HO₂[•]) and molecular species (H₂O₂, H₂, O₂), amongst which hydroxyl radicals and hydrogen peroxide are the most important for oxidation processes. Generation of hydroxyl, hydrogen and oxygen radicals in the discharge in water has been proven by emission optical spectroscopy (Sato et al., 1996).

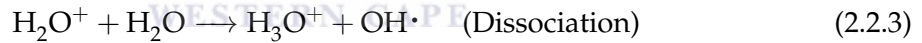
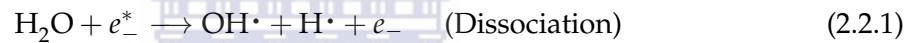
The formation of hydrogen peroxide was determined by chemical methods (Sunka et al., 1999). In addition, the generation of ozone was determined by colorimetric an indigo dye method, where oxygen gas was bubbled through the discharge region. The initial reaction rate constants for the formation of hydroxyl radicals and hydrogen peroxide by pulsed corona discharge were determined (Joshi et al., 1995). It was found that both rates were zero order, and that the reaction rate constants depended upon the magnitude of the applied electric field. The effects of the discharge parameters on radical formation were studied (Sun et al., 1997). It was observed that the pulse voltage level, polarity and liquid conductivity had a large effect on the OH[•] radical emission intensity. The OH[•] radical density increased with increasing pulse voltage and with decreasing electrode radius of curvature. The rate of increase was faster for the positive polarity than for the negative one. The radical emission intensity reached a maximum at conductivities between 1 and 8 mS/m and it greatly

increased when gas was bubbled in the discharge region.

2.2.4.4 Reaction mechanism

Streamer discharges, energized by a fast rising pulse voltage, produce non-thermal plasmas in water that generate a high electric field at the discharge streamer heads (of the order of 1 MV/cm) (Sunka et al., 1999) and produce electrons of high energy, which reaches beyond the dissociation energy of water (5.16 eV) or even ionization energy of water (12.62 eV). Therefore, the primary chemical effect of pulsed corona discharge in water is assumed to be in the production of hydroxyl and hydrogen radicals from the dissociation and/or ionization of water molecules by the highly energetic electrons. Since the process involves excitation, dissociation and ionization of water, the reaction mechanism may be similar to those in radiolysis processes such as radiation, electron beam radiation, pulse radiolysis and photochemical processes, which produce radicals and molecular species through excitation and ionization of the treated material (Joshi et al. 1995).

In these systems the mechanism of formation of $\text{OH}\cdot$ and $\text{H}\cdot$ radical is assumed to be as follows (Joglekar et al., 1991):



A high energy state is indicated by *. These radicals may, dependent on the energy distribution of electrons in the streamer head, either react with each other to form product molecules H_2 and H_2O_2 , or reform water (Equations (2.2.4) and (2.2.5)) or diffuse away from each other, to be available to react with solutes.



The system is therefore treated as though two separate reactions were occurring at the same time.

2.2.4.5 Physical processes of active species in corona discharge

In discharges with the pulse power in the MW range (Lang et al., 1998) a large part of the energy is consumed in the formation of a high temperature plasma channel, which emits

light in a wide range of wavelengths. This radiation can cause photolysis effects, leading to dissociation of water molecules and the formation of hydroxyl radicals. In addition, the expansion of the plasma channel against the surrounding water generates an intense shock wave with pressure of the order of hundreds of MPa. The resulting shockwave can induce pyrolytic and free radical reactions indirectly via electrohydraulic cavitation. As the plasma channel cools, thermal energy is transferred to the surrounding water, resulting in the formation of a steam bubble. Within a steam bubble, the temperature and pressure are high enough for the formation of transient supercritical water. Therefore, the oxidative degradation of organic compounds by such a type of discharge is attributed mainly to the ultraviolet photolysis, electro hydraulic cavitation and supercritical water oxidation (Wilbert et al., 1996).

2.2.4.6 Dielectric-barrier discharge (DBD)

Dielectric-barrier discharge, or simply barrier discharge, has been known for more than a century (Siemens et al., 1857). They concentrated on the generation of ozone. This was achieved by subjecting a flow of oxygen (or air) to the influence of a dielectric-barrier discharge (DBD) maintained in a narrow annular gap between two coaxial glass tubes by an alternating electric field of sufficient amplitude. The novel feature of this discharge apparatus was that the electrodes were positioned outside the discharge chamber and were not in contact with the plasma (Figure 2.7). In his later years Werner von Siemens considered his discharge configuration for the generation of ozone as one of his most important inventions.

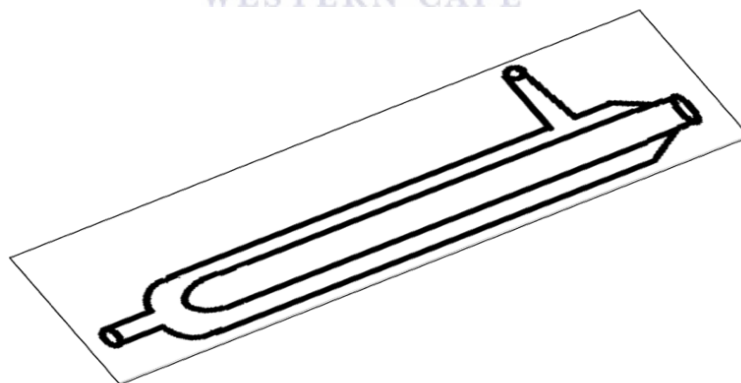


Figure 2.7: Historic sketch of the ozone discharge tube (Siemens et al., 1857)

There is an approach that helps to avoid spark formation in streamer channels. It is based on the use of a dielectric barrier in the discharge gap, which stops electric current and prevents spark formation. Such a discharge system is called a DBD. It has a large number of industrial applications, because they operate at strongly non-equilibrium conditions at atmospheric pressure and at reasonably high power levels, without using sophisticated

pulsed power supplies. This discharge is industrially applied in ozone generation. In addition, the DBD in air is commonly used in the conversion industry, where it is known commercially as "corona discharge treatment" and is used to treat polymer surfaces in order to promote adhesion, for example in the labeling on the plastics. (Sugiato et al., 2000). Important contributions to the fundamental understanding and industrial applications of DBD were made recently.

The DBD gap usually includes one or more dielectric layers, which are located in the current path between metal electrodes, as shown in Figure 2.8.

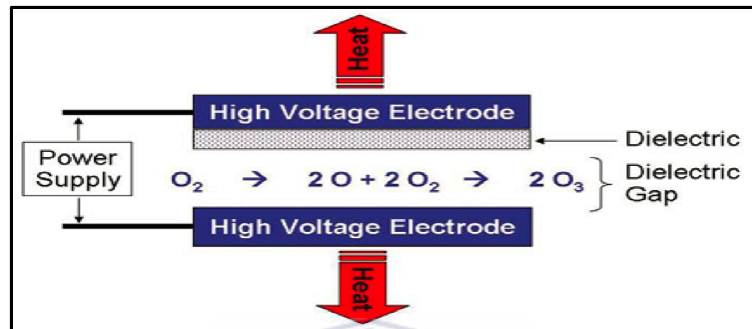


Figure 2.8: Production of ozone through dielectric discharge

The breakdown voltages of these gaps with dielectric barriers are practically the same as those between metal electrodes. If the DBD gap is a few millimeters, the required AC driving voltage, with frequency 500 Hz to 500 kHz, is typically about 10 kV at atmospheric pressure (Peyton et al., 1988). The dielectric barrier can be made from glass, quartz, ceramics or other materials of low dielectric loss and high breakdown strength. Then, a metal electrode coating can be applied to the dielectric barrier to form UV irradiation from the discharge, as shown in Figure 2.9.

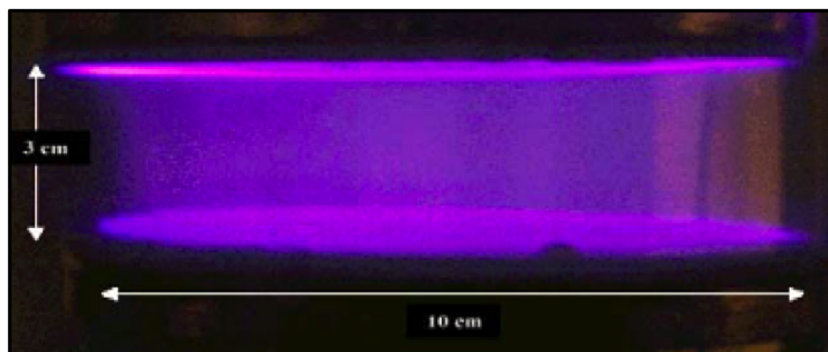


Figure 2.9: UV irradiation from the discharge gap between electrodes

The barrier-electrode combination also can be arranged in the opposite manner, where the metal electrode can be coated by a dielectric. It is important to clarify and distinguish the terms streamer and micro discharge. An initial electron starting from some point

in the discharge gap (or from the dielectric that covers the cathode in the case of well-developed DBDs) produces secondary electrons by direct ionization and develops an electron avalanche.

The streamer bridges the gap in a few nanoseconds and forms a conducting channel of a weakly ionized plasma. Intense electron current will flow through this plasma channel until the local electric field collapses. Collapse of the local electric field is caused by the charges accumulated on the dielectric surface and ionic space charge (ions are too slow to leave the gap for the duration of this current peak). On the other hand, a comparative experiment was focused on the NO decomposition behaviour in nitrogen (N_2) and air, for both pulsed corona discharge (PCD) and dielectric barrier discharge (DBD) reactors. Whereas the nitrogen discharge was expected to characterize the N generation efficiency, the air discharge characterized the O generation efficiency. A present experimental system consists of a PCD reactor with pulse power, a DBD reactor with an AC power supply, a gas supply facility, and measuring equipment for discharge and gas cleaning. The PCD processing is carried out in a wire-cylinder reactor, which is composed of a stainless steel wire electrode of 350 mm length and a cylinder electrode with a 27 mm inner diameter. Two different diameters of 1 and 2 mm are chosen for the wire electrode or different configurations, as is shown in Figure 2.10.

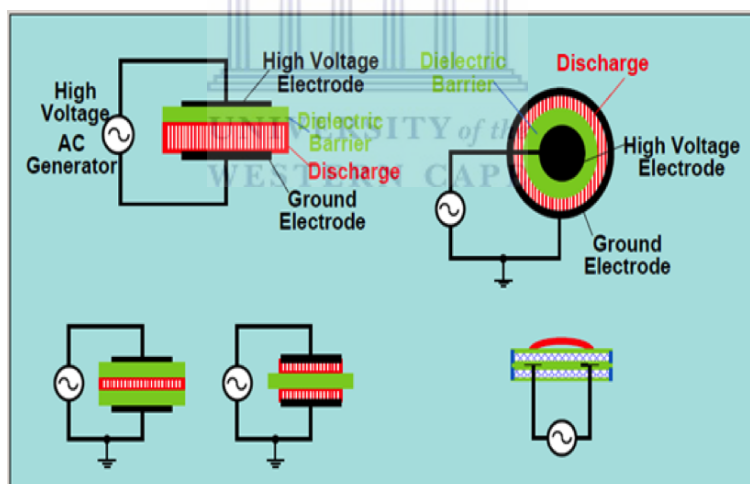


Figure 2.10: DBD reactor using different electrode configurations

The pulse power supply, operated with a rotary spark-gap switch, is delivering up to 40 kV with a 100ns pulse width, with a repetition rate fixed at 60 Hz. The DBD processing reactor has a coaxial-cylinder geometry. An outer cylinder electrode is made of a metal strip with a length of 240 mm, wrapped on a Pyrex tube (permittivity 4, inner diameter 27 mm, thickness 1.5mm) acting as a dielectric barrier. This DBD reactor is operated with a sinusoidal frequency of 60 Hz. In measuring the discharge energy deposited in the plasma, two electrical methods, current-voltage and charge-voltage measurement, are adopted for the PCD and DBD, respectively. Three different NO concentrations, namely 100, 200 and 300

ppm in both nitrogen and air ambient gases, are initially supplied to the reactors (Sugiato et al., 2000).

The authors conclude that the simulation results show that the PCD generates the energetic streamers with electric fields of 140~160 kV/cm in a wide region of the wire-cylinder reactor. On the other hand, the streamers in the DBD have relatively low electric fields of 80~120 kV/cm. The estimated G values indicate that the PCD is more efficient for generating N species, whereas the DBD is more effective for generating O species.

2.2.5 Influence of dissolved oxygen on the production of active species

The corona discharge principle is based on a high voltage alternating current between two electrodes, which are separated by a layer of dielectric material, and a narrow gap through which the oxygen bearing gas is passed. The introduction of gas improves the discharge effect, increases plasma channel volume and the quantity of active species. However, because of the difference in relative dielectric constant of water and gas, which is 80 and 1 respectively, high voltage is difficult to be applied to the mixed medium. With the introduction of oxygen, more ozone can be produced, while the generation of hydrogen peroxide is inhibited (Grymonpre et al., 2003). For liquid phase high voltage pulsed discharge, oxygen (air) is introduced through a hollow needle electrode. The $\text{OH}\cdot$, $\text{H}\cdot$, $\text{O}\cdot$, $\text{HO}_2\cdot$, O_2 , O_3 , H_2O_2 , and other active species generated by discharge are utilized to degrade organic pollutants (Kirkpatrick and Locke, 2005; Vel Leitner et al., 2005; Wang et al., 2006).

Table 2.3: Comparison of air and high purity oxygen feed systems

Source	Advantages	Disadvantages
Air	<ul style="list-style-type: none"> · Commonly used equipment · Proven technology · Suitable for small and large systems 	<ul style="list-style-type: none"> · More energy consumed per ozone volume produced · Extensive gas handling equipment required · Maximum ozone concentration of 3–5%
Oxygen	<ul style="list-style-type: none"> · Higher ozone concentration · Approximately doubles ozone concentration for same generator · Suitable for small and large systems 	<ul style="list-style-type: none"> · Safety concerns · Oxygen resistant materials required · Expensive

The combination of liquid phase and gas phase discharge processes have been investigated for water treatment (Yang et al., 2005). Gas-liquid series or parallel discharge reactor processes have the advantage of both liquid and gas phase discharge, in which the active species generated in liquid and gas phase cooperate to treat the organic wastewater and increase the decomposition efficiency of organic pollutants (Grymonpre et al., 2004). However, only part of the ozone dissolved in water is used, and the energy yield is low.

The synergistic combination of both gas and liquid discharge occurs through a peroxone process between the ozone dissolved in the water and the hydrogen peroxide produced in the liquid phase, which enhances the formation of hydroxyl radicals.

2.2.6 Factors that impact the plasma reaction

In general, plasma processing involves chemical and physical reactions between particles and solid surfaces in contact with the plasma processes. It uses many different ions sources or plasma sources, produced by DC glow or arc discharges, capacitive or inductive.

2.2.6.1 Electrode structure

A number of papers have been published on pulsed streamer corona discharge generated in water, using a point to plane geometry of electrodes, where the needle used as point electrode, is connected to the high voltage and the plane is earthed. It has been demonstrated to be effective at degrading a variety of organic compounds in water. It was shown that the principle reactive species involved in the breakdown process are hydroxyl radicals and hydrogen peroxide. However, the use of such a type of electrode configuration is limited, since needle electrode is quickly eroded in the discharge and only a small volume of the plasma discharge active region is generated.

The authors (Gasparik et al., 1998) recently developed a wire to cylinder electrode system, generating a large number of discharge channels, using a special composite electrode that consists of a metallic wire covered by a thin porous ceramic layer. The role of the ceramic layer is to enhance the electrical field on the anode surface by concentration of the pre-discharge current in small open pores. Optical spectroscopy results demonstrated that the ceramic coated electrode produced a plasma with very similar parameters as the needle-plate electrode configuration.

It was also found that the electrode material might have a catalytic effect on the reactions taking place during water cleaning. In the case of the gas phase plasma chemical reaction, the electrodes made of copper performed better than stainless-steel (Malik et al., 1999), probably due to a catalytic effect of copper to promote the decomposition.

2.2.6.2 Electrode gap

The electric field between electrodes mainly depends on the distance between them when the input voltage is kept unchanged, as shown in Figure 2.11. With a large electrode gap (30mm), a small discharge current was formed, due to the weakened electric field. For this case few and bright streamers, and less active species, were produced.

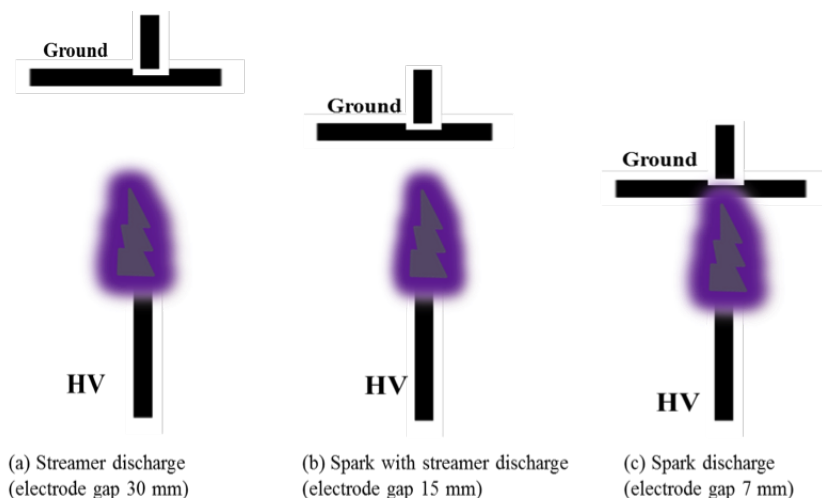


Figure 2.11: The influence of electrode gaps on electrical discharge (Lukes et al., 2002)

To change the electrode gap, the distance between the high voltage electrode and liquid surface was maintained at 12 mm, while the gas layer height between the ground electrode and liquid surface was changed to 3, 5, 7, 9 and 11 mm respectively. It was found that the optimal spacing between neighbouring needles also increased with the increase of needle numbers. The electrode gap has an appropriate range, and spark discharge may occur as the electrode gap decreases beyond this range, which may result in the erosion of the needle electrodes (Yang et al., 2007).

UNIVERSITY of the
WESTERN CAPE

2.2.6.3 Input voltage

With a higher input voltage, energetic electrons are produced more readily, and the formation of active species is thus accelerated. On the other hand, the change of discharge mode from weak streamer to intense streamers, with mixed blue-white light emitted, is observable with an increase of the input voltage to 46 kV (71 mJ). However, an intense spark discharge was produced between two electrodes when the input voltage was increased to 50 kV (84 mJ). It was found that the conversion increased with an increase of input voltage. A higher pulse frequency was also advantageous.

2.2.6.4 Pulse repetition rate

It was demonstrated that the conversion increased with an increase in pulse repetition rate. The energy injected into the reactor increased with an increase of the pulse repetition rate, which is beneficial for the conversion. However, the conversion increased very little when the pulse repetition rate was changed from 100 to 150 pps. This behaviour can be explained by the fact that the discharging capacitor, at higher repetition rates, does not have sufficient time to fully re-charge and so the pulse energy decreases (Grabowski et al., 2006).

2.2.6.5 Airflow rate

It was also demonstrated that the conversion improved with an increase of airflow rate. The highest conversion was obtained when the airflow rate was 96 l/h. The reaction between the ozone and the organic solutions is categorized as a gas-liquid interfacial reaction. Under usual conditions, the transfer of ozone from the gas phase to the liquid phase pertains to the liquid film control process, thus the increase of the airflow rate will be helpful for such a transfer. However, with a further increase of airflow, the residence time of ozone in the pre-oxidation zone is shortened. Accordingly, the utilization efficiency of ozone is decreased. (Lukes et al., 2006).

2.2.6.6 Conductivity of the solution

Lukes has shown that an increase in conductivity of the solution increases the UV component of the pulsed streamer discharge (Lukes et al., 2001).

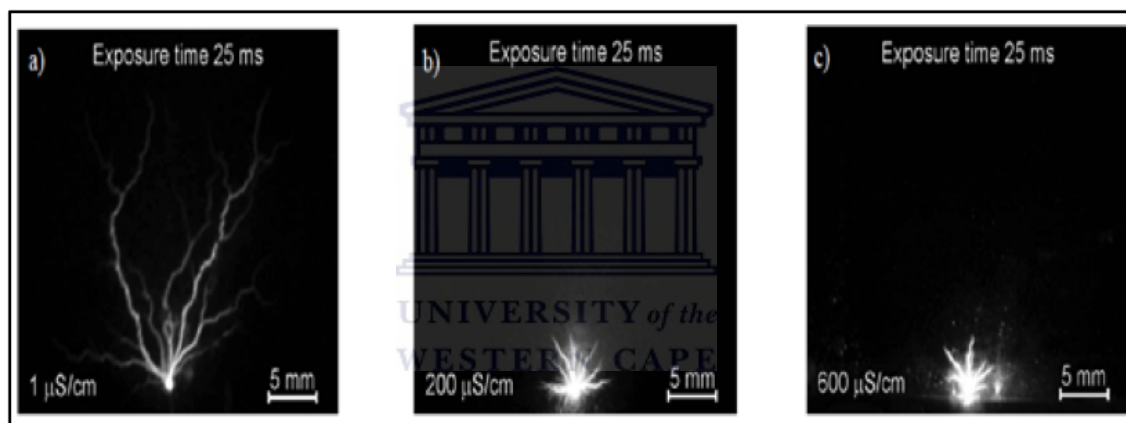


Figure 2.12: Typical images of the pulsed positive streamer discharge in the polluted water for different conductivities a) 1 $\mu\text{S}/\text{cm}$, b) 200 $\mu\text{S}/\text{cm}$, c) 600 $\mu\text{S}/\text{cm}$. The initial phenol concentration was 0.62 mM and the pulse energy 0.7 J (Lukes et al., 2001).

2.3 Design and construction of the reactor

2.3.1 Introduction

The composite electrode can be made in various dimensions and geometrical configurations, like the needle-plate, the pinhole electrode, the ring to cylinder, the wire to cylinder and the multi-electrodes, as shown in Figure 2.6.

2.3.2 The needle-plate

An electric field of about 1 MV/cm is necessary to initiate the discharge in water. For a needle electrode totally insulated from the liquid, except at its tip, the pre-discharge electric field can be estimated as $E = U/r_c$, where U is the applied voltage and r_c is the radius of

curvature of the needle tip. The goal was to build a sharper needle in order to generate the discharge at a lower applied voltage.

The sharp needles ($r_c = 0.05$ mm) are quickly eroded in the discharge and at an average power of 100 W, their lifetime is limited to 10–20 minutes, and only a small volume of the plasma discharge active region is generated. To overcome the limitation of the needle-plate electrodes, metal electrodes coated by a thin porous ceramic layer were developed (Lukes et al., 2002). The role of the ceramic layer is to enhance the electric field on the anode surface by concentration of the pre-discharge current in small open pores.

2.3.3 The pinhole electrode

In a pinhole electrode, also called a diaphragm discharge, the high voltage and ground electrodes are separated by an insulating sheet with a small hole. The diaphragm discharge has a coaxial electrode geometry, where the insulating sheet was placed on the surface side of the anode, which is connected to the high voltage.

2.3.4 The ring to cylinder

When using the needles configuration, the principle reactive species involved in the breakdown process are hydroxyl radicals and hydrogen peroxides. However, the plasma is quickly eroded in the discharge and only a small volume of the plasma discharge active region is generated. In order to produce a plasma with a larger volume, a ring to cylinder electrode configuration is used, where the discharge in the liquid is initiated from the shaped edges of the ring electrode.

2.3.5 The wire to cylinder

The wire to cylinder is a system that generates a large number of discharge channels, using special composite electrodes that consist of a metallic wire covered by a thin porous ceramic layer. Without the thin ceramic coating of the wire cylinder electrodes it is more difficult to develop the intense electric field necessary to initiate corona discharge, and the wires also corrode easily.

2.3.6 Multi-electrodes

In pulsed electric discharges, researchers have considered a number of processes and products involved in the microbiocidal action. These include the production of chemically active substances, including ozone, hydrogen peroxide and hydroxyl and superoxide free radicals. UV radiation is also generated by the discharge itself, as well as acoustic and shock waves. Among the different means of electric discharge, a novel configuration involving ring wire cylindrical multi-electrode discharge may have some advantages over the two electrode systems most generally used at the present time. Recent studies, utilizing multi-electrode discharge systems, have been performed, where measurements of generated UV

radiation, as well as production of ozone and hydrogen peroxide have been made.

Advantages of multi-electrodes over the two-electrode system are:

1. The generation of UV radiation, as well as the production of ozone, hydrogen peroxide and free radicals. All plays the major role and are very effective in the destruction of microorganisms in liquids.
2. A decrease in the discharge load on each electrode, thereby enhancing the erosion resistance of the system as a whole, which will increase the lifetime of the system considerably.
3. Due to the short lifetime radicals, such hydroxyl radicals, produced in the reactor, the multi-gate system, which generates the oxidants at each single gate, will be more effective in microorganism removal from water. (Maximization of radical's production and lethal effect of bacteria).
4. The enhancement of the effective corona discharge treatment volume by distributing a varying electric field guide over the reactor's interior chamber.

2.3.7 Preliminary conclusion

Based on the findings of other researchers discussed above, the focus of the research will be on electrical discharge in water, using multi-electrodes in a specific way to reduce the discharge load, avoiding corrosion and producing permanent UV light. The main advantage of such a system is the direct in situ production of reactive species, thereby eliminating the need for externally supplied sources of oxidizing agents.

2.4 Photocatalysis

2.4.1 Introduction

Photocatalysis is the process whereby a photoreaction increases in the presence of a catalyst. A catalyst does not change during the chemical reaction and neither is it consumed, but plays a role by making the chemical reaction happen faster. Photocatalysis, which may also be termed as a photo-induced reaction, produces surface oxidation to eliminate harmful substances such as organic compounds and bacteria, when exposed to sun or a fluorescent lamp (Macwan et al., 2011). The photocatalyst is activated by exposure to UV light. The principle of a photocatalytic reaction is used to accelerate nature's cleaning and purifying process using light as energy. Photocatalysis can be used for various steps in purifying a contaminated environment. One of these steps is when semiconductors are selected as photocatalysts, because semiconductors have a narrow gap between the valence and conduction bands. These types of reactions are activated by absorption of a photon with sufficient energy from UV light, that equals or is higher than the band-gap energy of the catalyst. The

absorption leads to a charge separation due to promotion of an electron (e^-) from the valence band of the semiconductor catalyst to the conduction band, thus generating a hole in the valence band (Macwan et al., 2011). This movement of electrons forms e^-/h^+ or negatively charged electron/positively charged hole pairs, the hole pair can oxidize donor molecules. If a photocatalyzed reaction is favoured, then recombination of the electron and the hole must be prevented as much as possible.

2.4.2 Principle of photocatalytic oxidation

Photocatalytic reaction mechanisms are studied widely. TiO_2 is the most efficient, biologically inert, photostable and inexpensive photocatalyst. It has good mechanical hardness and is an environmentally friendly photocatalyst, which is widely used for photodegradation or photo-mineralization of various pollutants (Lee et al., 2011), as shown in Figure 2.13.

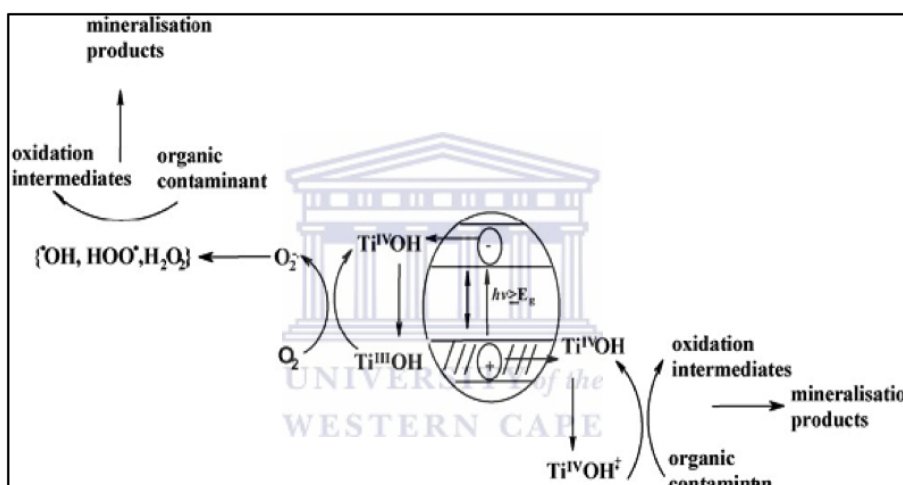


Figure 2.13: Diagram showing the processes involved in photo-mineralization of organic compounds (Lee et al., 2011)

TiO_2 is a semiconductor and the principle of the semiconductor photocatalytic reaction is straightforward. On absorption of photons with energy larger than the band gap of TiO_2 , electrons are excited from the valence band to the conduction band, creating electron-hole pairs as mentioned above. These charge carriers migrate to the surface and react with the chemicals adsorbed on the surface to decompose the chemicals. This photodecomposition process usually involves one or more radicals or intermediate species such as OH^\cdot , O_2^- , H_2O_2 , or O_2 , which play important roles in the photocatalytic reaction mechanisms (Chen & Mao, 2007). The photogenerated valence band hole converts the surface hydroxyl group and adsorbed water molecules to highly reactive OH radicals, which have strong oxidizing power to rapidly degrade a variety of organic contaminants in water (Choi & Hong, 2011). The surface-bound OH radicals oxidize organic compounds adsorbed on the TiO_2 surface, and OH radicals can also diffuse in the reaction medium to cause photocatalytic oxidation away from the surface (Choi & Hong, 2011).

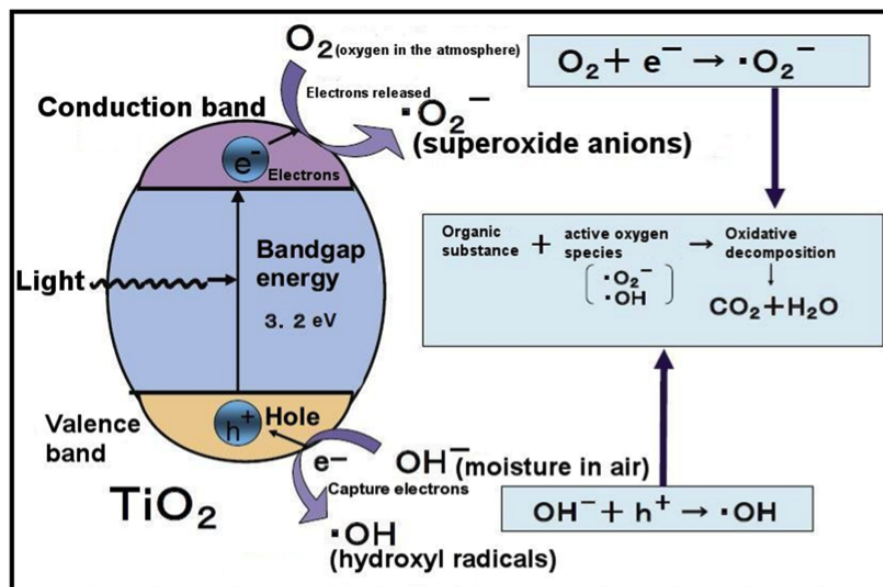


Figure 2.14: The photocatalytic reaction mechanisms (Riley et al., 2010)

The photocatalytic activity of a semiconductor is largely controlled by its light absorption properties, such as the light absorption spectrum and coefficient, reduction and oxidation rates on the surface by the electron and hole, and the electron-hole recombination rate (Chen & Mao 2007).

Riley reviewed photocatalysis and showed its environmental use in that photocatalysis purifies air and water, produces fuels such as H_2 and CH_3OH , can also initiate polymerization reactions, and enhance the treatment of tumours. In order to develop efficient catalytic materials, it is important to bring the light to where it is needed and bring the reactants into contact with the catalyst at the right time and provide sufficient surface area for an efficient reaction. Most photocatalysts are formed as nanoparticles, because it is easy to obtain the photo-hole and photo-electron near the surface, before recombination at the surface (Riley et al., 2010).

A large surface area with a constant surface density of adsorbents leads to faster surface photocatalytic reaction rates. In this sense, the larger the specific surface area, the higher the photocatalytic activity is. On the other hand, the surface is a defective site, therefore, the larger the surface area, the faster the recombination, this recombination applies to the nanocrystals as they have a large surface area. The higher the crystallinity, the fewer the bulk defects, and the higher the photocatalytic activity may be. High temperature treatment usually improves the crystallinity of TiO_2 nanomaterials, which in turn can induce the aggregation of small nanoparticles and decrease the surface area. Optimal conditions are sought by taking these considerations into account and may vary from case to case (Chen & Mao 2007).

Heterogeneous photocatalysis is a process in which a combination of photochemistry and catalysis are operating together. It suggests that both light and catalyst are necessary to initiate the chemical reaction. UV light illumination over a semiconductor such as TiO_2

produces electrons and holes. The valence band holes are powerful oxidants, while the conduction band electrons are good reductants (Macwan et al., 2011).

Advanced oxidation processes are seen as promising alternatives to traditional methods of disinfection. Several compounds have been investigated as potential photocatalytic materials for use in water purification, including TiO_2 , SiO_2 , ZnO , CdS , ZrO_2 , V_2O_5 , CuO , Fe_2O_3 , Al_2O_3 , etc. In these photocatalytic materials, TiO_2 is the most suitable chemical for photocatalytic disinfection of water. Hydroxyl radicals are powerful oxidizers that can damage microbial cell walls and membranes, DNA and RNA. The deposition of metal elements into the TiO_2 matrix has been used to increase the efficiency of photocatalytic disinfection, resulting in an increase in the hole concentration and a decrease in band gap energy, which extends the range of the photoactive response to the visible light spectrum (Lee et al., 2011).

2.4.3 TiO_2 as semiconductor

Semiconductor materials are materials whose valence band and conduction band are separated by an energy gap or band gap. Among all these semiconductors, the most widely used semiconductor catalyst in photo induced processes is titanium dioxide (TiO_2). Though TiO_2 has the disadvantage of not being activated by visible light, but by ultraviolet (UV) light, it is advantageous over the others in that it is chemically and biologically inert, photocatalytically stable, relatively easy to produce and to use, able to efficiently catalyze reactions and also cheap. However, the latest research shows that TiO_2 bio-accumulates and can be toxic. The performance of TiO_2 for certain technical applications is predominantly influenced by its crystallite size, surface area, phase structure, and impurity (dopant) type and concentration (Macwan et al., 2011). The relevant potential level of the acceptor species is thermodynamically required to be below the conduction band of the semiconductor. Otherwise, the potential level of the donor is required to be above the valence band position of the semiconductor in order to donate an electron to the vacant hole (Stamate et al., 2007).

2.4.4 Titanium dioxide and crystalline phases

Titanium dioxide is a naturally occurring oxide of the element titanium, with a molecular formula TiO_2 and molecular mass of 79.90 g/mol. Titanium dioxide is a fine white powder with a monoclinic crystal structure, also referred to as titanium (IV) oxide or titania (see Figure 2.15).

Titanium dioxide is most commonly extracted from titanium tetrachloride by carbon reduction and re-oxidization. Alternatively, it may be processed from another oxide called ilmenite, which is subjected to reduction with sulfuric acid to achieve pure titanium dioxide.

Titanium dioxide particles are referred to as primary aggregates or agglomerates. Primary particles are single crystals that are bound by crystal planes. Aggregates are sintered primary particles that are connected by crystal faces. Agglomerates are multiple primary particles and aggregates that are held together by van der Waal's forces. Scattering of light by titanium dioxide is maximized in particles that are 0.2–0.3 μm in diameter (Lezere et al., 2011). TiO_2 exists in three polymorphic phases: rutile, a tetragonal crystal structure with a



Figure 2.15: Titanium dioxide commercial fine white powder

density of 4.25 g/cm^3 ; anatase, a tetragonal crystal structure with a density of 3.894 g/cm^3 and brookite, a orthorhombic crystal structure with a density of 4.12 g/cm^3 (Ahmad et al., 2008). Of these phases, anatase and rutile are the most commonly encountered. Rutile is the thermodynamically stable form of TiO_2 at all temperatures and at normal pressures, while anatase is highly photocatalytically active.

In all three polymorphs, titanium is coordinated octahedrally by oxygen, but the position of the octahedral differs between polymorphs. The structure of rutile is the densest and its unit cell is the smallest. Anatase has four formula units per unit cell with $a = 0.379 \text{ nm}$ and $c = 0.951 \text{ nm}$; rutile has two with $a = 0.459 \text{ nm}$ and $c = 0.296 \text{ nm}$, and brookite has eight with $a = 0.917 \text{ nm}$, $b = 0.546 \text{ nm}$ and $c = 0.514 \text{ nm}$. Rutile TiO_2 has 32 atoms and anatase TiO_2 has 96 atoms in the lattice structure (Prasai et al., 2012).



Figure 2.16: Rutile in crystal form

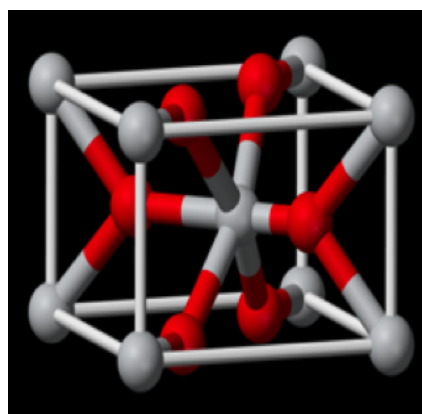


Figure 2.17: Rutile structure

The chemical composition of polymorphic phases of the natural rutile, anatase and brookite contain impurities of up to $\approx 2\%$ that include iron, chromium, vanadium, aluminium, niobium, tantal, hafnium and zirconium and account for slight variations in density, colour and indices of refraction (Lezere et al., 2011).

Rutile and anatase can be described in terms of chains of TiO_6 octahedra, where each Ti^{4+} ion is surrounded by an octahedron of six O^{2-} ions. The two crystal structures differ in the



Figure 2.18: Anatase in crystal form

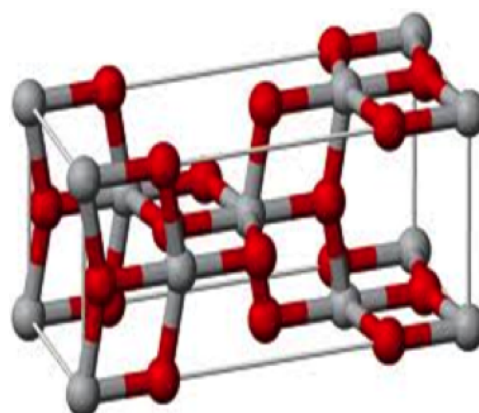


Figure 2.19: Anatase structure



Figure 2.20: Brookite in crystal form

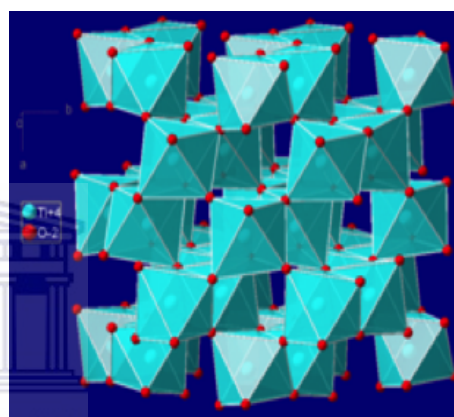


Figure 2.21: Brookite structure

distortion of each octahedron and by the assembly pattern of the octahedra chains. In rutile, the octahedron shows a slight orthorhombic distortion, while in anatase, the octahedron is significantly distorted so that its symmetry is lower than orthorhombic. The Ti–Ti distances in anatase are larger, whereas the Ti–O distances are shorter than those in rutile. In the rutile structure, each octahedron is in contact with 10 neighbour octahedrons (two sharing edge oxygen pairs and eight sharing corner oxygen atoms), while, in the anatase structure, each octahedron is in contact with eight neighbours (four sharing an edge and four sharing a corner). These differences in lattice structures cause different mass densities and electronic band structures between the two forms of TiO₂ (Chen & Mao 2007). In the different crystal structures of TiO₂, anatase has the higher photocatalytic activity and is commonly used for photocatalysis (Ahmad et al., 2008). This higher photocatalytic activity is related to its lattice structure. Each Ti atom is coordinated to six oxygen atoms in anatase tetragonal unit cell. A significant degree of buckling is associated with O–Ti–O bonds in anatase compared to rutile TiO₂ (Ahmad et al., 2008). Crystal symmetry is reduced due to this buckling and in turn results in larger unit cell dimensions (Ahmad et al., 2008). According to Blake et al. (Blake et al., 1999) the most active photocatalysts are formulations based on the anatase crystal phase, and most work has been done using the P-25 form of TiO₂. This material is a mixture of phases with an approximate composition of 75% anatase and 25% rutile and has a BET

surface area of about 50 m²/g.

Table 2.4: Types and physical properties of titanium oxide

Properties	Rutile	Anatase	Brookite
Crystalline form	Tetragonal system	Tetragonal system	Orthogonal system
Density (g/cm ³)	4.27	3.90	4.13
Refractive index	2.72	2.52	2.63
Mohs' hardness	7.0–7.5	5.5–6.0	5.5–6.0
Permittivity	114	48	78
Melting point (°C)	1825	Transformation to rutile	Transformation to rutile

TiO₂ is stable in aqueous media and is tolerant against both acidic and alkaline solutions. It is inexpensive, recyclable, reusable and relatively simple to produce. It can also more readily be synthesized in nanostructure forms than many other catalysts. Furthermore, its band gap is appropriate to initiate a variety of organic reactions (Ahmad et al., 2008). Nanocrystalline semiconductor TiO₂ particles are of interest due to their unique properties and several potential technological applications, such as photocatalysis, sensors, solar cells and memory devices (Ahmad et al., 2008).

Due to its high refractive index, chemical reactivity and photochemical reactivity, titanium dioxide (TiO₂) is considered as one of the most important photocatalysts to solve environmental problems, especially in the purification of polluted water and air. The semiconductor TiO₂ is most extensively used, because it has many advantages. It is inert and resistant to corrosion, and it requires little post-processing, making it inexpensive, as mentioned above. TiO₂ can react under mild operating conditions, although it needs ultraviolet light for photocatalysis to occur. TiO₂ is the most investigated photocatalyst system and has been found to be capable of decomposing a wide variety of organics. Tang et al. (2005) has reported the synthesis of TiO₂ nanoparticles that uses the low-temperature reaction of low-valent organometallic precursors. It is said that bis-(cyclooctatetraene) titanium reacts with dimethyl sulfoxide in organic solution at temperatures as low as room temperature to produce TiO₂. In the absence of any supporting ligand, the reaction gives precipitation of amorphous TiO₂ powder. However, in the presence of basic ligands such as tributylphosphine, tributylphosphine oxide and trioctylphosphine oxide, the precipitation is arrested, and chemically distinct, isolated, internally crystalline TiO₂ nanoparticles are formed.

2.4.5 Structural properties of TiO₂ nanomaterials

Crystals of anatase are very characteristic and are not easily confused with any other mineral. They form the eight faced tetragonal dipyrramids that come to sharp elongated points.

The elongation is pronounced enough to distinguish this crystal form from octahedral crystals, although there are some similarities. Anatase has a band gap of 3.2 eV (Blake et al., 1999) and has been found to be the most active form for photocatalysis.

The photocatalytic process includes chemical steps that produce reactive species that, in principal, can cause fatal damage to microorganisms (Blake et al., 1999). The photodecomposition process involves formation of species, such as the hydroxyl radical, hydrogen peroxide, superoxide, conduction band electrons, and valence band holes. Formation of singlet oxygen on irradiated TiO₂ is not usually considered to be present under the usual conditions of disinfection reactions. The reactive oxygen species may disrupt or damage various cells, viral functions or structures. The preponderance of evidence on photocatalytic chemistry in aqueous solution suggests that the hydroxyl radical formed by hole transfer does not diffuse from the surface of the TiO₂ into bulk aqueous phase (Blake et al., 1999).

As the size of the TiO₂ particles decreases, the fraction of atoms located at the surface increases with higher surface area to volume ratios, which can further enhance the catalytic activity. The increase in the band gap energy with decreasing nanoparticle size can potentially enhance the redox potential of the valence band holes and the conduction band electrons, allowing photoredox reactions, which might not otherwise proceed in bulk materials, to occur readily. One disadvantage of TiO₂ nanoparticles is that they can only use a small percentage of sunlight for photocatalysis. Practically, there exists an optimal size for a specific photocatalytic reaction (Chen & Mao 2007). Photocatalytic activity of TiO₂ nanoparticles was determined for hydrogenation reactions of CH₃CCH with H₂O, and it was found that activity increased as the diameter of the TiO₂ particles decreased, especially below 10 nm. The authors suggested that the dependence of the yield on the particle size arose from the differences in the chemical reactivity, and not from the physical properties of these catalysts (Chen & Mao 2007).

The modification of TiO₂ to make it sensitive to visible light is one of the most important objectives in photocatalyst studies (Yu et al., 2010). The sensitization of TiO₂ with absorbed molecules, such as a Ru complex and H₂[PtCl₆] (or PtCl₄) were reviewed. The main approaches involve either introducing an isolated impurity state into the forbidden band or narrowing the band gap by doping a foreign element into TiO₂. Anion doping into TiO₂ (anatase) can be used to control the density of states of its valence band.

2.4.6 Properties of TiO₂ nanomaterials

Rutile is the most stable phase at high temperatures, but anatase and brookite are common in fine grained (nanoscale) natural and synthetic samples. On heating concomitant with coarsening, the following transformations are all seen: anatase to brookite to rutile, brookite to anatase to rutile, anatase to rutile, and brookite to rutile. These transformation sequences imply very closely balanced energetics as a function of particle size. The surface enthalpies of the polymorphs are sufficiently different that crossover in thermodynamic stability can occur under conditions that preclude coarsening, with anatase and/or brookite stable at small particle size (Chen & Mao, 2007).

The crystal structure of TiO₂ nanoparticles depended largely on the preparation method. For small TiO₂ nanoparticles (<50 nm), anatase seemed more stable and transformed to rutile at >700°C. The prepared TiO₂ nanoparticles had anatase and/or brookite structures, which transformed to rutile after reaching a certain particle size. Once rutile was formed, it grew much faster than anatase, then rutile became more stable than anatase for particle size >14 nm (Chen & Mao, 2007).

2.4.7 Applications of TiO₂

TiO₂ nanoparticles absorb impinging photons with energies equal to or higher than its band gap (>3.0 eV). Electrons are then excited from the valence band into the unoccupied conduction band, leading to excited electrons in the conduction band and positive holes in the valence band. These charge carriers can recombine, non-radiatively or radiatively, dissipating the input energy as heat, or get trapped and react with electron donors or acceptors adsorbed on the surface of the photocatalyst. The competition between these processes determines the overall efficiency for various applications of TiO₂ nanoparticles (Chen & Mao, 2007).

The existing applications of TiO₂ nanomaterials include paint, toothpaste, UV protection, photocatalysis, photovoltaics, sensing and electrochromics, as well as photochromics. Their optical and biological properties allow TiO₂ to be suitable for UV protection applications. A surface is superhydrophilic or superhydrophobic when the water-surface contact angle is larger than 130° or less than 5°. TiO₂ nanomaterials can be imparted with clear functions on various glass products, such as mirrors and eyeglasses, having superhydrophilic or superhydrophobic surfaces (Chen & Mao, 2007).

TiO₂ nanomaterials were reviewed for water splitting and hydrogen production, due to their suitable electronic band structure, given the redox potential of water. Another application of TiO₂ nanomaterials, when sensitized with dyes or metal nanoparticles, is to build photochromic devices (Chen & Mao, 2007). One of the many applications of TiO₂ nanomaterials is the photocatalytic decomposition of various pollutants (Chen & Mao, 2007). The photocatalytic activity of titania results in thin coatings of the material exhibiting self-cleaning and disinfecting properties under exposure to UV radiation. These properties make the material a candidate for applications such as medical devices, food preparation surfaces, air conditioning filters, and sanitary ware surfaces (Fujishima et al., 1999). Titanium dioxide has also been produced as engineered nanomaterials, which may be equidimensional crystals or sheets, and are composed of either titanium dioxide-rutile or titanium dioxide-anatase. A tubular structure has been produced from different layers of titanium dioxide-anatase, which results in fibres with an outer diameter of about 6 nm and an inner tube of about 3 nm (Lezere et al., 2011).

2.4.8 Photo-induced electron and hole properties of TiO₂ nanomaterials

A photocatalyst must be able to use the excited electron to synthesize hydrogen and to use the electron hole to synthesize oxygen (Hoefelmeyer et al., 2011). This is similar to photosyn-

thesis, where plants convert sunlight to fuel, such as sugars and an oxidizer that is oxygen. For this reason photocatalysis within a photoelectrochemical cell is sometimes referred to as artificial photosynthesis. The materials that were planned to be used include nanocrystals of TiO_2 , Pt and RuO_2 , dye molecules and lipids (Hoefelmeyer et al, 2011). The materials were organized in chemical reactions and self-assembly steps to produce a reactive free-standing membrane capable of solar photocatalysis in which water was converted to hydrogen and oxygen (Hoefelmeyer et al, 2011).

2.4.9 Toxicity of TiO_2 particles to the environment

Blake et al. (1999) has done a study on the effect of the TiO_2 on the people exposed to it. The first epidemiologic survey of respiratory disease among 209 titanium metal production workers showed that 17% of the subjects had signs of pleural disease, which suggested that reductions in ventilation capacity may be associated with the exposure to titanium tetrachloride and titanium dioxide. However, the epidemiologic study of 1576 workers exposed to TiO_2 particles showed no statistically significant association between TiO_2 exposure and risk of lung cancer and chronic respiratory diseases. No cases of pulmonary fibrosis have been found among TiO_2 exposed workers. The same conclusion was reached in another epidemiologic study of 2477 employees from TiO_2 plants that showed no statistically significant association between titanium tetrachloride exposure and risk of lung cancer and chronic respiratory diseases. However, some pathologic changes, such as pulmonary fibrosis and skin necrosis, may be associated with direct exposure to large quantities of TiO_2 particles. Illuminated TiO_2 has strong oxidizing power that can be used to kill tumour cells in cancer treatment (Chen & Mao, 2007). TiO_2 was thus considered to be a non-pathogenic, inert mineral particle. Usually, in the absence of UV light, neither anatase nor rutile exhibits much biological activity. Pathogenic effects of TiO_2 particles are usually due to general physical stimulation activity (Blake et al., 1999). Titanium dioxide is an ultraviolet activated catalyst, and organic polymers that are in contact with it degrade under UV radiation. Anatase is 10 times more active than rutile and responds to slightly different wavelengths (Lezere et al., 2011).

2.4.10 Various light sources

There are various sources of light such as the sun, incandescent lamps, fluorescent lamps, UV-visible light traps, disinfectant light, and so on. Those sources emit light with different wavelengths necessary for their specific purposes, but the light used for the activation of TiO_2 is UV light. It has been previously stated that TiO_2 is a semiconductor and is active under UV light for photocatalytic activity. When titanium dioxide generates a pair of a conduction band electrons and a valence band hole in the solid oxide lattice by absorbing a photon with energy greater than 3.2 eV ($\lambda < 388$ nm), and the subsequent charge transfers at the interface, this initiates various kinds of redox reactions under the ambient condition (Choi et al., 2006). The energy that excites the electrons is provided by light and it should

have the same wavelength as ultraviolet light forming free radicals. The resulting free-radicals are very efficient oxidizers of organic matter.

2.4.11 Photocatalytic water splitting

Photo electrochemical cells include catalysts that rapidly capture sunlight and convert the energy to a chemical fuel and chemical oxidizer. This can be done by 'splitting' water into hydrogen and oxygen. More specifically, water undergoes auto dissociation to give protons and hydroxide anions. If electrons are added to protons, then hydrogen is synthesized, while taking away electrons from hydroxide anions would yield oxygen. The catalyst speeds up these two chemical processes. The catalyst must also be able to absorb sunlight. Upon doing so, the light energy causes the excitation of an electron. The electron is more reactive after excitation, which is why it leaves an electron 'hole' (Hoefelmeyer et al., 2011). The work on photocatalyst materials for solar hydrogen involves the use of high surface area TiO_2 functional materials, that enable photocatalytic water splitting (Hoefelmeyer et al., 2011). TiO_2 photocatalysis is a typically treatment that reduces toxic organic compounds to non-toxic inorganic compounds, such as carbon dioxide, water, ammonium or nitrates, and chloride ions (Bessergenev et al., 2005).

Since the discovery of photocatalytic splitting of water on a TiO_2 electrode, an enormous research effort has been dedicated to the study of the properties and applications of TiO_2 under light illumination (Fujishima et al., 1999). Photocatalytic splitting of water into H_2 and O_2 , using TiO_2 nanomaterials, continues to be of interest for clean and sustainable energy sources. The principle of water splitting using a TiO_2 photocatalyst has been studied. Water molecules are reduced by the electrons to form H_2 and oxidized by the holes to form O_2 , leading to overall water splitting (Chen & Mao, 2007).

The potential of the band structure of TiO_2 is just the thermodynamical requirement. Other factors such as charge separation, mobility and the lifetime of photogenerated electrons and holes also affect the photocatalytic properties of TiO_2 . These factors are strongly affected by the bulk properties of the material, such as crystallinity. Surface properties such as surface states, surface chemical groups, surface area, and active reaction sites are also important. The water-splitting process, in return, affects the local pH environment and surface structures of the TiO_2 electrode (Chen & Mao, 2007).

2.4.12 Preparation methods for TiO_2 nanostructures

2.4.12.1 Sol-gel method

The sol-gel method is one of the most convenient ways to synthesize various metal oxides due to low cost, ease of fabrication and low processing temperatures. It is widely used to prepare TiO_2 for films, particles or monoliths. In general, the sol-gel process involves the transition of a system from a liquid "sol" (mostly colloidal) into a solid "gel" phase. The homogeneity of the gels depends on the solubility of reagents in the solvent, the sequence of addition of reactants, the temperature and the pH. The precursors normally used for the synthesis and doping of nanoparticles are organic alkoxides (Ahmad et al., 2008). Ultrafine

titanium dioxide nanoparticles that range in size from 1 to 150 nm, with a modal primary particle size of 10–50 nm, are generated by sol-gel synthesis and the wide variation in their morphology and size is controlled by the pH of the gel (Lezere et al., 2011). Sol-gel is one of the best techniques that can be applied to prepare and analyze the formation of nanotitania. Some effective parameters on the nature of the sol-gel process are the metal precursor, temperature, pH of solution and the presence/absence of a catalyst. The proposed benefits of the sol-gel process are considered to be easy control of the formation process, high stability, better homogeneity, and high purity. The sol-gel process has been widely employed for the preparation of titanium dioxide particles, because the control of hydrolysis and polycondensation reactions can be easily established and the appropriate properties obtained. TiO₂ nanomaterial can be synthesized by the sol-gel process with different titanium precursors.

Typically, synthesis of TiO₂ nanoparticles via the sol-gel process includes an acid-catalyzed hydrolysis step of titanium (IV) alkoxide, followed by condensation. The development of Ti-O-Ti is carried out in the presence of a small amount of water. The presence of a large excess of water leads to the development of polymeric Ti-O-Ti chains (Zhang et al., 2009). This method is based on inorganic polymerization reactions. It includes four steps: hydrolysis, polycondensation, drying and thermal decomposition (Tavakoli et al., 2007). The advantages of the sol-gel method is excellent compositional control, ultrafine porous powders, homogeneity of product, strong promise of industrial application on a large scale, use of matrix support which can, in principle, modify the properties of nanomaterials. On the other hand, the disadvantage is its high cost (Tavakoli et al., 2007). In a typical sol-gel process, a colloidal suspension, or a sol, is formed from the hydrolysis and polymerization reactions of the precursors, which are usually inorganic metal salts or metal organic compounds, such as metal alkoxides. Complete polymerization and loss of solvent leads to the transition from the liquid sol into a solid gel phase. Thin films can be produced on a piece of substrate by spin-coating or dip-coating (Chen & Mao, 2007). According to Tang et al. (Tang et al., 2005) the researchers exploited "nonhydrolytic sol-gel" chemistry that had been developed previously for the manufacture of bulk titania.

2.4.12.2 Hydrothermal method

Hydrothermal processing is when aqueous solutions, vapours, and/or fluids react with solid materials at high temperature and high pressure. It is a well-known process in mineralogy and geology for the formation, alteration or deposit of minerals, ores or rocks. This method exploits the solubility of almost all inorganic substances in water at elevated temperatures and pressures and subsequent crystallization of the dissolved material from the fluid. Water at elevated temperatures plays an essential role in the precursor material transformation, because the vapour pressure is much higher and the structure of water at elevated temperatures is different from that at room temperature. The properties of the reactants, including their solubility and reactivity, also change at high temperatures (Tavakoli et al., 2007).

During hydrothermal treatment metal cations initially precipitate in the form of poly-

meric hydroxides. Over time, these hydroxides undergo dehydration to form the metal oxide crystal structures. It was found that the presence of the second metal cation was beneficial in controlling the particle formation process, probably by preventing the formation of complex hydroxides when the base was added to the cold metal. Particularly, hydrothermal processing is suitable for the preparation of powders in the form of nanoparticles or even single crystals (Tavakoli et al., 2007).

The advantages of hydrothermal methods include desired size and shape, well crystallized powders, homogeneous in size, shape, and composition, high density powders, very low grain sizes, narrow particle size distribution, single phase, controlled particle morphology, high-purity powders and nanocrystals with high crystallinity. Its disadvantages are the difficult to control the process, problems with reliability and reproducibility (Tavakoli et al., 2007).

2.4.12.3 Solvothermal method

In the solvothermal method, the solvent is not limited to water, but also includes other polar or nonpolar solvents, such as benzene. The process is more appropriately called solvothermal synthesis in different solvents. High temperature-high pressure solutions, vapours, and/or fluids can act on materials as:

- transfer medium of pressure, temperature, and mechanical energy,
- adsorbate, which plays a role of catalyst or reaction accelerator,
- solvent, which dissolves and allows to reprecipitate the solid materials.

Reagents, which form hydroxides, oxides, oxyhydroxides, and/or salts, that are the substances acting as adsorbate and/or solvent, are called "mineralizers". These actions can also be used in processing of inorganic materials: preparation, formation, alteration, sintering, etching, etc. (Tavakoli et al., 2007). Recent trends in preparing the starting powders for hydrothermal or solvothermal synthesis of nanoparticles are directed toward more dispersed systems using solutions (wet systems) and/or gases (dry systems), rather than traditional solid state systems. In the solid state systems, the homogeneity of composition, structure, and microstructure cannot be controlled not to exceed the range of the solid particle size, whereas the gas or solution systems can manipulate much finer particles on molecular or atomic size. Thus, the gas or solvent dispersed systems can assure much better process control. Pressurized and heated gas and solution systems are transferred to hydrothermal equipment, so that the hydrothermal systems can be regarded as developed gas and/or solution systems (Tavakoli et al., 2007).

2.4.12.4 Comparison between hydrothermal and sol-gel methods

Many researchers have found the sol-gel method to be the best method to use for the synthesis of TiO₂ nanofibres. In addition, it was reported that the sol-gel method is a more suitable

method compared to the hydrothermal method (Chuangchote et al., 2009). TiO₂ nanofibres were fabricated by the combination of the electrospinning and sol-gel techniques using poly(vinylpyrrolidone) (PVP), titanium(IV) butoxide, and acetylacetone in methanol as a spinning solution. TiO₂ nanofibres (260-355 nm in diameter), with a bundle of nanofibrils (20-25 nm in diameter), aligned in the fibre direction, or particle-linked structures were obtained from the calcination of as-spun TiO₂/PVP composite fibres at temperatures ranging from 300°C to 700°C. These nanofibres were utilized as photocatalysts for hydrogen evolution. The nanofibre photocatalyst calcined at 450°C showed the highest activity among the TiO₂ nanofibres tested, such as those prepared by the hydrothermal method and anatase nanoparticles. These results indicate that one-dimensional electrospun nanofibres with highly aligned bundled nanofibrils are beneficial for the enhancement of the crystallinity, large surface area and higher photocatalytic activity.

2.5 Electrospinning

2.5.1 Introduction

Electrospinning is a relatively simple method for fabricating ultrafine fibres, which are known as nanofibres. Electrospinning can be used to convert nanoparticles into long nanofibres with the aid of a polymer base (Hu et al., 2006). This process is used to spin fibres having a diameter in the sub-micron range, using an electric field (Ojha et al., 2007). The surface of a polymer solution droplet is charged by a high voltage to induce the ejection of a liquid jet. The ejected liquid jet is solidified at the collector (Doh et al., 2007). This is a facile technique to produce nanofibres, having potential in a variety of applications (Ojha et al., 2007).

The dispersion of metal nanoparticles into polymer nanofibres is of great interest, not only due to the novel properties of the nanocomposite materials, but also the continuously growing demand for further miniaturization of electronic components, optical detectors, chemical and biochemical sensors and devices (Mishra & Ahrenkiel, 2011). Fibre membranes have been shown to be very useful for heterogeneous catalysis and also as supports for catalytic metal nanoparticles and nanowires. Compared to conventional film photocatalysts, nanofibre-based photocatalysts have greater surface-to-volume ratio, and the porous structure allows for higher surface active sites for effective catalysis. The surface area is proportional to the fibre diameter and the volume is proportional to the square of the diameter, the specific surface area is inversely proportional to the fibre diameter, leading to high specific surface areas for small fibres (Dzenis et al., 2004). The pore size depends on the fibre diameter, and, therefore, small fibres will produce non-wovens with a small pore size (Ojha et al., 2007). These nanofibres may provide a connection between the nanoscale and the macroscale, since the diameters are in the nanometer range and the lengths are kilometers. The electrospinning process can be combined with the sol technique, sol-gel technique and gas-solid reaction, to fabricate nanofibres. Electrospinning is also used for the generation of TiO₂ fibres, when combined with the sol-gel process (Park et al., 2011). In a typical electrospinning process for the preparation of TiO₂ nanofibres, a Ti-precursor sol-gel solution

with a polymer matrix is used as the starting material, to proceed under a high electrical field (Lin et al., 2011). The electrospinning process has three primary components, a high voltage supply to charge the polymer solution, a grounded electrode where nanofibres are deposited and a syringe with pumps, from which the polymer solution is fed through a capillary connected to a syringe filled with the polymer solution, as shown in Figure 2.22 (Ojha et al., 2007).

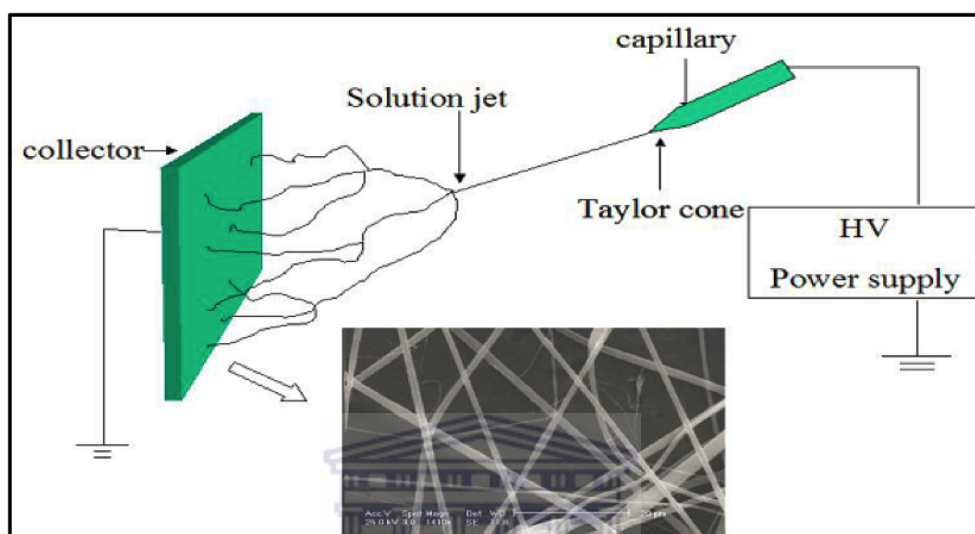


Figure 2.22: The electrospinning process (Huang et al., 2003)

Electrospinning offers several advantages, which are:

- The process of fabricating nanofibres is simple and efficient.
- The diameters of nanofibres fabricated can be easily controlled.
- The range of the application is wide.

TiO₂ nanofibres have opened a wide spectrum of new possibilities for high photocatalytic activity and easy recovery. Moreover, the electrospun nanofibres, with both high porosity and large surface area, being available for reaction are promising materials for surface modification and functionalization (Wang et al., 2009). Titania is a wide band gap semiconductor material with many important applications, including solar cell and photocatalysis. Anatase can be excited under UV light and rutile under visible light. The production of mixed-phase anatase and rutile nanocrystalline fibres are beneficial. Incorporation of noble metal nanoparticles is a recent method to enhance the photocatalytic behaviour of titania. Nanostructured noble metals are believed to be excellent heterogeneous catalysts (Mishra & Ahrenkiel, 2011).

Hollow titania, containing multilayer nanofibres, can be fabricated through the combination of electrospinning with a layer-by-layer technique (Zhang et al., 2008). Two different solvents, methylbenzene and THF were used to remove the template. The morphology of

the obtained hollow multilayer nanofibres confirmed that THF is better than methylbenzene. The obtained hollow multilayer fibre had a diameter of about 700 nm and its shell thickness was about 140 nm. FTIR spectra showed the fabrication of multilayer nanofibres. XPS measurements indicated that TiO₂ nanoparticles could be assembled successfully. The obtained multilayer hollow nanofibres showed a higher photocatalytic activity to degrade methylene blue solution compared with TiO₂ films, due to their unique hollow structure.

2.5.2 Fabrication of TiO₂ nanofibres via electrospinning, combined with the sol-gel method

The electrospinning technique has attracted much attention, because it provides a cost-effective, versatile and simple way to fabricate 1-D TiO₂ nanostructure materials in a short period time (Lin et al., 2011).

A study of synthesized nanofibres has shown good biological performances, such as improved cell adhesion and differentiation (Lim et al, 2008). Therefore, nanofibrous modification of dental and bone implants might enhance osseo-integration. The purpose of the study was to investigate the nanofibrous modification of titanium implants. TiO₂ nanofibres were fabricated by the electrospinning method, using a mixture of Ti(IV) isopropoxide and poly(vinyl pyrrolidone) (PVP) in an acidic alcohol solution. Then the nanofibres were immobilized on the NaOH/HCl-treated titanium plates by inducing the alcohol condensation reaction of Ti(IV) isopropoxide with Ti-OH group on the titanium surface, and subsequent calcination (500–1000°C). The immobilized TiO₂ nanofibres were characterized by SEM, XRD and a simulated removal test. The diameter of the TiO₂ nanofibers could be controlled within the range of 20–350 nm by changing the amounts of Ti(IV) isopropoxide and PVP. Phase transformation from anatase to rutile was observed after calcination. After the simulated removal test, TiO₂ nanofibres remained on the titanium surface. These TiO₂ nanofibres on titanium plates can potentially be used for the surface modification of titanium implants to improve their integration.

The study on nucleation and growth kinetic of titania nanoparticles, prepared by a sol-gel method, shows that the rate constant for coagulation of particles increases with temperature, because the velocity of monomer through the particles has a high dependency upon temperature. Secondary particles were formed and the growth of particles increased when they passed a critical radius and became stable (Mehranpour et al., 2011), (Zhang et al., 2009).

TiO₂ nanofibres and TiO₂ nanotubes were formed by calcination of new precursor nanofibres of poly (vinyl alcohol) (PVA)–titanium compound hybrids (Nakane et al., 2007). The precursor nanofibres were formed by using electrospinning with water as a solvent. It was the safest method to use water as a solvent during the electrospinning process. The immobilization of TiO₂ catalysts on various substrates has also been studied to prepare TiO₂ nanofibres by a modified sol-gel method, to tune the electronic structure of TiO₂ and improve its photocatalytic activity under visible light

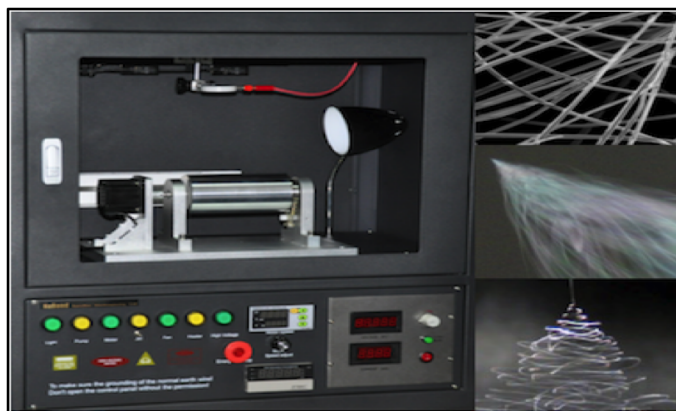


Figure 2.23: Photographs of the electrospinning setup with temperature control

2.5.3 Transformation of TiO_2 nanofibres

Various techniques can be applied to transform nanofibres. The formed nanofibre mats were decomposed by initial drying for 24 h at 80°C under vacuum, after which they were calcined in an air atmosphere at 600°C for 1 h, with a heating rate of $5^\circ\text{C}/\text{min}$ (Kanjwal et al., 2010). Nanocrystalline TiO_2 was also synthesized by the solution combustion method, using titanyl nitrate and various fuels such as glycine, hexamethylenetetramine, and oxalyldihydrazide. These catalysts are active under visible light, have optical absorption wavelengths below 600 nm, and show superior photocatalytic activity for the degradation of methylene blue and phenol under UV and solar conditions compared to commercial TiO_2 , Degussa P-25. The higher photocatalytic activity is attributed to the structure of the catalyst. Various studies such as X-ray diffraction, Raman spectroscopy, Brunauer-Emmett-Teller surface area, thermo gravimetric-differential thermal analysis, FT-IR spectroscopy, NMR, UV-vis spectroscopy, and surface acidity measurements were conducted. It was concluded that the primary factor for the enhanced activity of the combustion-synthesized catalyst is a larger amount of surface hydroxyl groups and a lowered band gap. The lower band gap can be attributed to carbon inclusion into TiO_2 , giving $\text{TiO}_{2-2x}\text{C}_x\text{VO}_2$ (Nagaveni et al., 2004).

Titania nanofibres were fabricated by drying electrospun TiO_2 /polyvinylpyrrolidone nanofibres for 5 hrs in air and subsequent annealing for 3 hrs at temperatures from 450°C to 550°C in air. To improve the bond strength, a TiO_2 buffer layer with a thickness of 400 nm was spin-coated onto a glass slide prior to electrospinning, by using the same precursor solution. Only the anatase TiO_2 phase was observed for the TiO_2 /PVP fibres calcined at temperatures between 450°C and 550°C , but the fibres calcined at temperatures higher than 600°C yielded a mixture of anatase and rutile phases. The bond strength of the TiO_2 nanofibres with a height of $1\ \mu\text{m}$ was investigated by using a tape test, according to ASTM D 3359-02, to evaluate the extent of adhesion of the fibre mat to the glass substrate. Among the coatings, the highest bond strength of the fibres was achieved for the TiO_2 nanofibre/ TiO_2 buffer layer/glass coatings, calcined at 500°C . Experimental results revealed that the extent of adherence increased by 10% when a buffer layer was inserted between the fibres and the glass. Therefore, it can be concluded that the addition of a buffer layer has a modest in-

fluence on the bond strength between the nanofibre mat and the glass substrate (Lee et al., 2008).

TiO₂ nanofibres, formed by the gel-sol process from a condensed Ti(OH)₄ gel, performed by the hydrolysis of a Ti-triethanolamine (TEA), were also decomposed (Mehranpour et al, 2011). The titanium complex was hydrolyzed by degrees in water and completely converted to a rigid gel of Ti(OH)₄ after aging at 100°C for 24 hrs. This was the first aging step. Then, the Ti(OH)₄ gel was totally transformed into anatase TiO₂ nanoparticles by additional aging at 140°C in an autoclave for 3 days, to obtain uniform anatase TiO₂ nanoparticles.

Nakane and Ogata (2010) had decomposed the TiO₂ by calcinating the PVA-TL nanofibres at 400–700°C for 5 hours. Anatase-type TiO₂ was formed at 400–600°C, and the peak intensities increased with the calcination temperature. Rutile-type (rutile-anatase mixed) TiO₂ was formed at 700°C. It is well-known that anatase is superior to rutile for photocatalysis. Thus, a calcination temperature of 600–700°C would be an effective condition when using the TiO₂ nanofibres as a photocatalyst. The relationship of the calcination temperature of the TiO₂ nanofibres, the specific surface area and pore volume decrease with an increase of the calcination temperature. This is due to the sintering of the TiO₂ by the calcination. They then concluded by saying that the photocatalysis of the TiO₂ nanofibres calcined at 600°C and 700°C was higher than that of the TiO₂ nanofibres calcined at 400°C and 500°C. Chuangchote et al. (2009) showed the effect of varying the temperature and their results are shown in Table 2.5.

Table 2.5: Diameters and physical properties of precalcined as-spun PVP/TiO₂ composite nanofibres and calcined TiO₂ nanofibres at various calcination temperatures

Material	Calcination Temperature (°C)	Diameter of nanofibres (nm)	Diameter of nanofibrils or nanoparticles (nm)	Percentage of the Anatase phase	Size of the Anatase crystals (nm)	Size of the Rutile crystals (nm)
Nanofibres	Precalcined	409±110				
Nanofibres	300	355±92				
Nanofibres	400	298±71	15.4±3.2	100%	13.2	
Nanofibres	450	272±90	20.6±3.1	100%		
Nanofibres	500	261±76	24.8±3.7	80.3%	16.1	17.4
Nanofibres	600	264±86	44.4±5.9	7.2%	25.3	30.8
Nanofibres	700	259±59	74.7±7.2			39.9
ST-01			19.5±3.3	100%	10.4	

2.6 Chapter Summary

The relevant information concerning advanced oxidation methods for water treatment, the electrical discharge in water, photocatalysis and, more specifically, the synthesis of TiO₂ nanofibres, have been presented in this chapter. Some limitations exist on the use of a single treatment method which requires the combination of techniques for proper cleaning water. The titania photocatalyst can be used to enhance the treatment process either as free-standing particulate or as coating on a substrate. Most experiments utilized finely powdered TiO₂ particles suspended in contaminated water, in slurry form, which provides a large surface area and makes recovery difficult after treatment. Coated catalyst configurations, on the other hand, eliminate the need for catalyst filtration and centrifugation, immobilization of the titania photocatalyst is the best way to overcome drawbacks, but generally result in a significant reduction in system efficiency. A reduction of 60-70% in performance is reported in aqueous systems for immobilized TiO₂, compared to the unsupported catalyst (Kabra et al., 2004). Therefore, there is a need for new fashion techniques to prevent the drawback of unsupported catalysts and to enhance the immobilization system's performance. Furthermore, many kinds of support have been explored for TiO₂ photocatalysts, which include soda lime glass (Chung et al., 2005), aluminium (Chen et al., 2000), ceramic tiles (Kemmit et al., 2004) and coated glass (Macedo et al., 2007). Since coatings are very thin, the actual active surface area of the photoreactor, compared to the overall volume, is low. It was also noted that the mechanism of TiO₂ nanofibres on consolidated support material needs more attention. Despite aforementioned drawbacks, more coated photocatalysts and immobilization techniques are still being investigated.

In view of the gaps identified in the literature review, the research presented in this thesis aims at identifying the synthesis protocol condition for producing new fashion TiO₂ immobilized on support materials, using an electro spinning technique. The integration of the immobilized TiO₂ in the reactor is still not well understood, meaning that there is a need for further work in that direction. The next chapter presents the experimental materials, setup and sample preparation together with a description of the procedures that were conducted to achieve the research objectives set for this thesis.

Chapter 3

Materials and experimental procedures

This chapter presents a detailed description of the materials and chemicals used in this study. The research approach, experimental procedures, equipment setup and characterization techniques used in the present research work are also detailed. A schematic highlighting the experimental design and procedure that was followed in the respective chapters are presented here.

3.1 Materials and chemicals

A summary of all the materials and chemicals used during the execution of the research is given in Table 3.1.

Table 3.1: Summary of chemicals used in the study without further purification

Chemical name	Purity	Supplier
Tryptone Soya Broth (TSB)	98%	Aldrich
Methanol (MeOH)	99.9%	Kimix
Methylene blue (MB)	98%	Merck
Polyacrylonitrile (PAN)	98%	Merck
N, N-dimethyl formamide (DMF)	99%	Aldrich
Titanium tetrachloride (TiCl ₄)	99%	Kimix
Acetic acid	98%	B&M Scientific
Titanium dioxide (TiO ₂) (Degussa P25)	98%	Agar Scientific
Copper (Cu) grid	N/A	Kimix
Potassium iodate (KI)	97%	Aldrich
5.5 Dimethylpyroxide (DMPO)	99%	Kimix
Tryptone Soya Agar	99.9%	Kimix
A mixture of propane and butane	97%	AFROX
Hydrochloric acid	37%	Aldrich
Sulfuric acid	99%	Aldrich
Nitrogen gas	Technical grade	AFROX

3.2 Experimental

3.2.1 Experimental setup

In the interest of achieving the set research objectives in Chapter 1 of this thesis, the experimental approach was designed in such a way to provide the answers to the predetermined research questions. The schematic diagram presented in Figure 3.1 highlights the three major parts of the experimental setup and Figure 3.2 is a photo showing the high voltage AC power supply, which is the energy source, the oscilloscope probe used for measuring the specifications, such as the voltage across the electrodes, the current and frequency, and finally, the submerged reactor in the waste water to be treated.

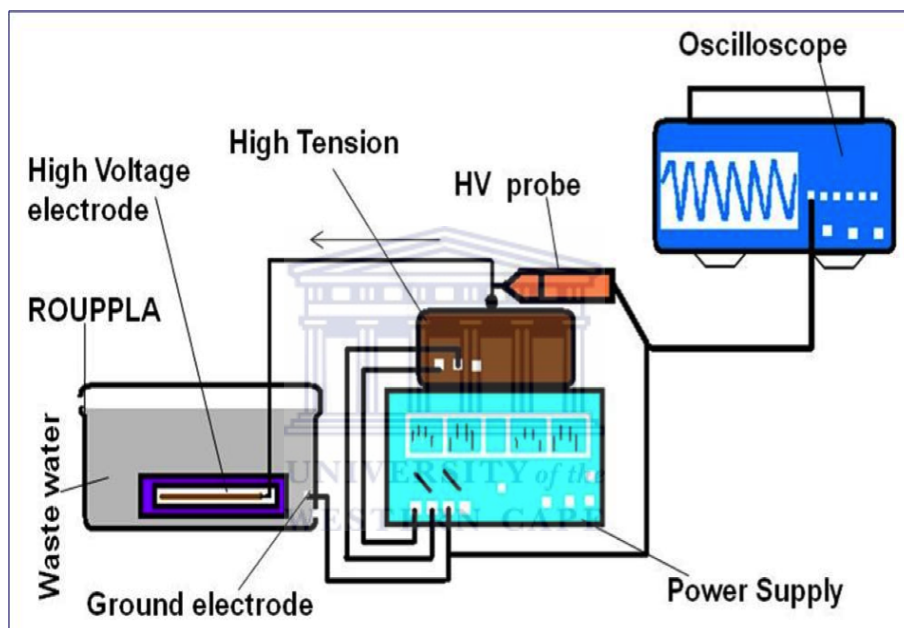


Figure 3.1: The experimental setup

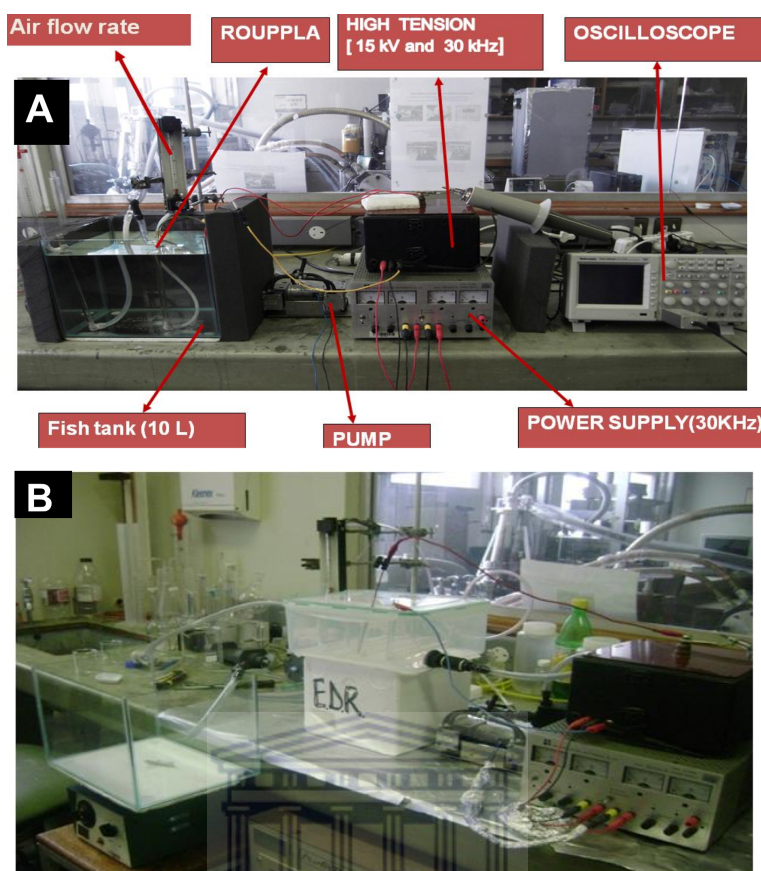


Figure 3.2: Two different photos showing (A) the uncirculated water system and (B) the circulated water experimental setup, using the same power source

3.2.2 Equipment

The different tools and materials used in the present study to fabricate the prototype reactors are listed in Table 3.2.

Table 3.2: List of design tools and supplies

Items	Supplier
Polyvinyl chloride (PVC)	Kimix Chemicals & Laboratory Supplies
Perspex	Perspex suppliers
Quartz tubes	Glass Chem., Stellenbosch
High Voltage (HV) AC supply	Electrical & Electronic Engineering, Stellenbosch
HV measuring probe	Electrical & Electronic Engineering, Stellenbosch
Oscilloscope	Electrical & Electronic Engineering, Stellenbosch
pH meter	Electrical & Electronic Engineering, Stellenbosch
Air pump	Electrical & Electronic Engineering, Stellenbosch
Flow rate meter	Kimix Chemicals & Laboratory Supplies
Copper wire	Kimix Chemicals & Laboratory Supplies
Furnace	Gallenkamp, USA

3.2.3 Designs of prototypes

Although several configurations and alternative designs were tried, ultimately three reactors were designed and built over the lifetime of this project. The first prototype reactor, called OK-1, was made with polyvinyl chloride (PVC), the second prototype reactor, called OK-2, was made with Perspex, while the third prototype reactor, called OK-3, was made with tube quartz glass. All the prototypes were designed based on the corona discharge principle, which is defined as a high electric field between two electrodes, which are separated with dielectric material and a narrow gap where air is passing through.

3.2.3.1 Prototype OK-1

The prototype OK-1 model reactor was made with PVC in a specific way, having a 200 mm long double flat glass as the dielectric material, with a water inlet and outlet as shown in Figure 3.3. The multi electrodes (5 copper) were positioned on top of the glass and the plate electrode at the bottom. The gap distance between two flat glasses is 1 cm, where water is passed through at a very slow flow rate of 100 ml/h. The samples were collected for analysis at different times, such as 0, 10, 20, 30 and 60 min.

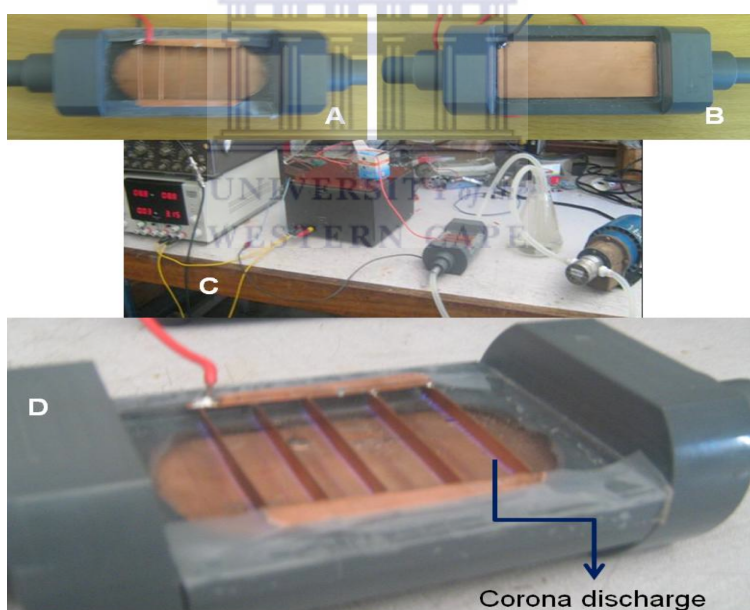


Figure 3.3: The OK-1 reactor during discharge, which produces the UV irradiation on top of the dielectric glass material, and also ozone. A) Top side picture of the multi electrodes OK-1, B) Bottom side picture with one plate copper electrode of OK-1, C) complete setup, showing all the necessary peripheral items to operate the OK-1 and to circulate the water for treatment and D) The OK-1 reactor during discharge, which produce the UV irradiation on top of the dielectric glass material, and also ozone

3.2.3.2 Prototype OK-2

A drawing of the discharge reactor OK-2 design is presented in Figure 3.4, and actual photos are shown in Figure 3.5. The prototype OK-2 was made with two Perspex blocks with a

length of 20 cm, width of 12 cm, and a thickness of 1.5 cm, with 12 machined grooves. The first groove was centred 3.4 cm from the edge of the block. The groove length was 8.4 cm, with an outside width of 0.6 cm, and was machined to a depth of 0.9 cm. Within the groove, a second channel was machined with a width of 0.25 cm, a length of 8.15 cm and a depth of 0.5 cm. Thus, the total depth of the complete groove was 1.4 cm, leaving 0.1 cm of the Perspex as a dielectric barrier between the electrodes and the water flow path. The distance between the centre of one groove to the next was set at 1.2 cm. 10 holes (0.3 cm diameter) for plastic screws were placed 0.7 cm from the edge of the block, and spaced 6.0 cm apart (edge and middle hole) and 6.6 cm apart (two middle holes) along the lengths of the block. Along the widths of the block the holes were 5.3 cm apart.

The top Perspex block had two additional holes for the entrance and exit of water. The diameter of the water holes were 0.8 cm, centred 6.0 cm along the width of the block, and 1.35 cm from the first and last grooves. A water tight seal was provided by a rubber O-ring. To control the space between the electrodes, the screws used to assemble the two blocks were adjusted until the distance was set to the desired value. The electrodes were copper plates cut to fit in the inner channel of the grooves, and the larger outer channel was then filled with wax to prevent arcing, and ozone generation on copper wires. The reactor was designed and built at Stellenbosch University in the machine workshop of the Department of Electrical & Electronic Engineering. For clarity, this second reactor was called OK-2 (Okolongo reactor-2). A CAD drawing of the design is shown in Figure 3.4.

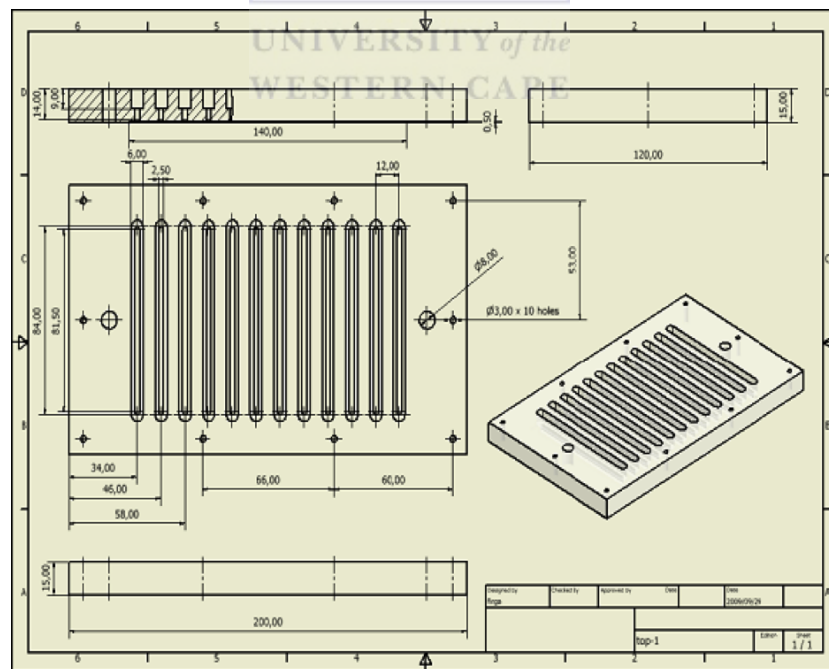


Figure 3.4: CAD drawing of the discharge reactor

Electrodes were connected in series to the power source (a 15 kV, 30 kHz, 5 mA home made power supply). Current and voltage characteristics were monitored using an oscilloscope with a high voltage probe, and a multimeter. A 2 litre beaker was used as a water

reservoir and a small aquarium water pump was used to circulate water through the Perspex discharge reactor, as can be seen in Figure 3.5.

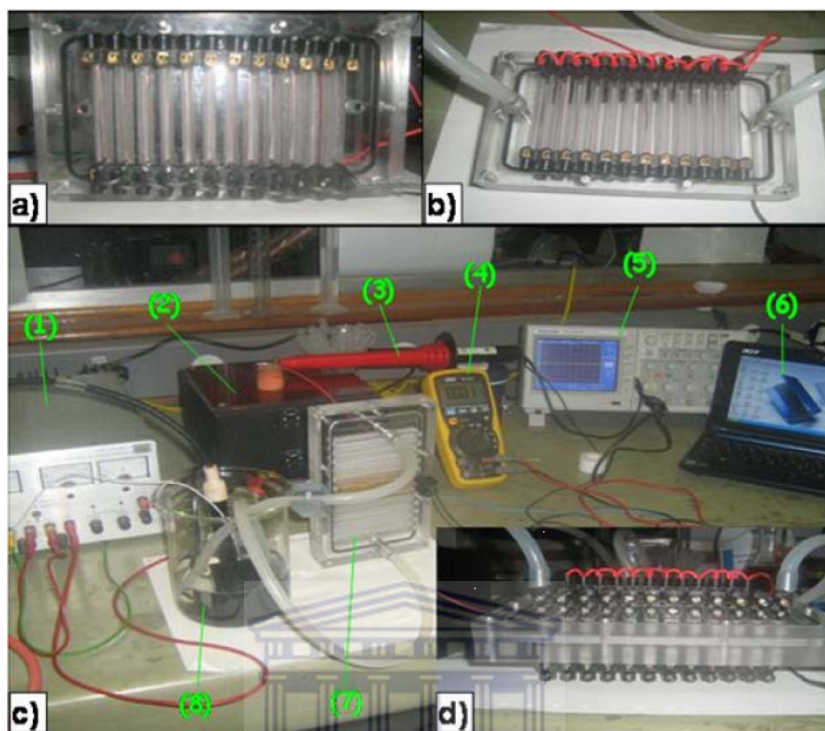


Figure 3.5: Images of OK-2, a), b) & d) are bottom, top and side views of the electrohydraulic discharge reactor, and c) is the setup used to test the reactor. (1) is the power supply for the pump, (2) is the power supply for the reactor, (3) is the high voltage probe connected to the (5) oscilloscope, (4) is the multimeter used to measure the current, (6) is the laptop for storing the data of the oscilloscope, (7) is the reactor, and (8) is a beaker with a water pump used to circulate water through the reactor.

3.2.3.3 Prototype OK-3

Electrohydraulic Discharge Reactor 3 (OK-3) consisted of a 200 mm long double cylinder with an opening on top for entrance of gas, and a fritted glass opening for dispersal of air. The cylinder consists of an inner and outer tube. The inner tube has an internal diameter of 6 mm, and an outer diameter of 8 mm. The inner diameter of the outer tube is 9 mm, and the outer diameter of the outer tube is 12 mm. Thus, the gap between both tubes is 1 mm. Gas flowed through the 1 mm gap from the opening on top, and was dispersed through the glass frit at the bottom. There were two openings on top. One formed part of the inner tube, while the second led to the gap between the two tubes. The inner tube was filled with the solution of interest, and a copper wire was dipped into the solution and was connected to the power supply. The double cylinder was placed in a beaker, which served as the "reactive zone", and the counter electrode was placed in the solution in the beaker, thus completing the circuit. The OK-3 and peripheral systems for complete operation are presented in Figure 3.6.

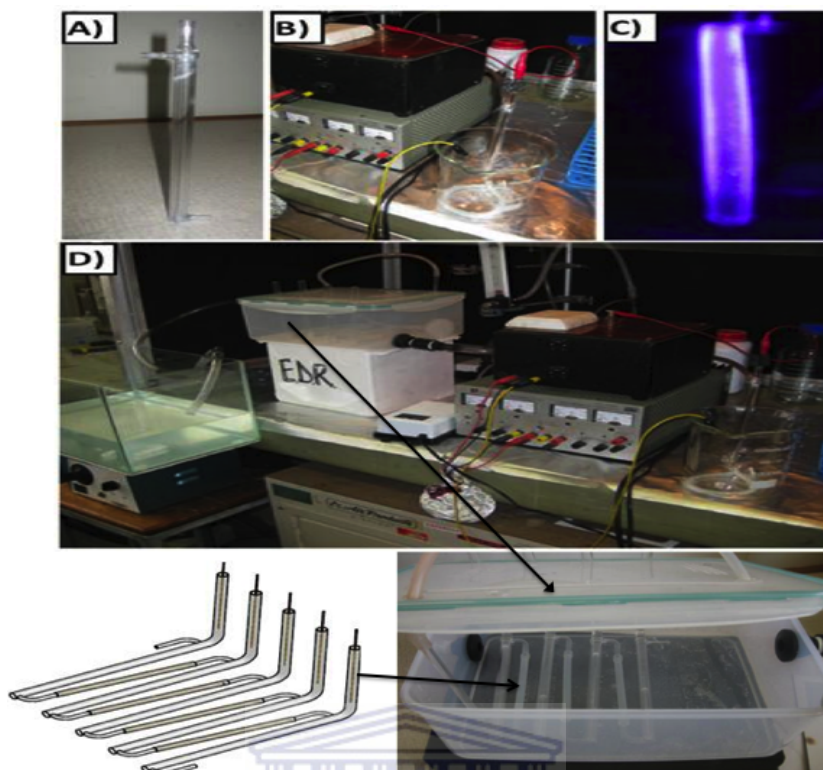


Figure 3.6: A) picture of the OK-3, B) One unit of OK-3 in a beaker and connected to the power supply, C) the OK-3 during discharge, and D) complete setup showing all necessary peripheral items to operate the OK-3 and to circulate the water for treatment.

3.2.4 Degradation of Methylene blue (MB) using OK-1 and OK-2

In order to investigate the working concept of prototypes OK-1 and OK-2, a 10 ppm solution of Methylene blue was used as model dye. Two electrodes (high voltage and ground) were used for this initial experiment, and the voltage used was 12 kV, while the measured current was 3 mA (total power = 36 W). Samples from the circulated water were taken at $t = 0$, 30 and 60 minutes, and the UV-Vis spectrum taken from 600–700 nm. Peak absorbance at 665 nm was used to determine changes in concentration. A control experiment was done with no power applied to the electrodes.

3.2.4.1 Preparation of standard solutions

Methylene blue was dissolved in a volumetric flask with ultra-pure water to the 1000 ml mark. The measured absorbance readings at 665 nm are given in Table 3.3. The standard absorbance curve for Methylene blue is shown in Figure 3.7.

Table 3.3: Methylene blue standard solutions

Sample Concentration	Absorbance at 665 nm	Methylene blue mass
X2		
0.5 ppm	0.067	0.0005g
1.0 ppm	0.128	0.0010g
1.5 ppm	0.248	0.0015g
2.0 ppm	0.330	0.0020g
2.5 ppm	0.427	0.0025g

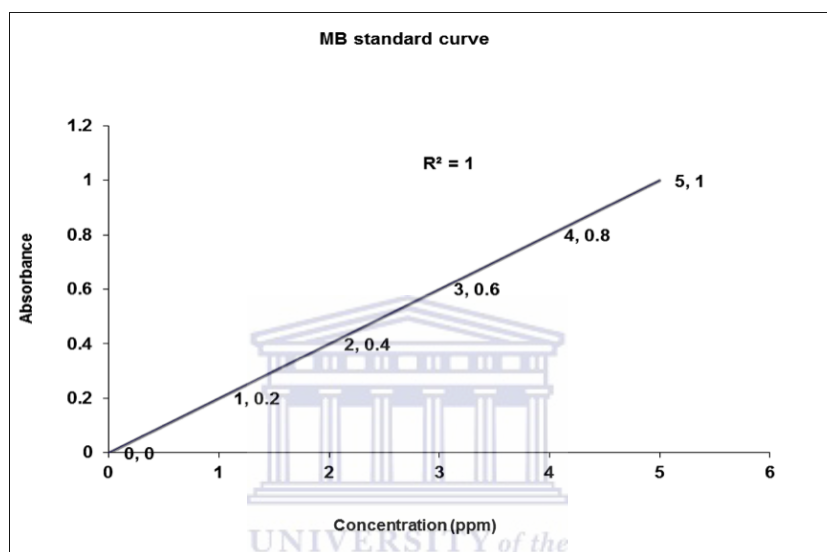


Figure 3.7: Standard curve for Methylene blue

3.2.5 Protocol for testing OK-3 with dye solutions

A 10 ppm solution of Methylene blue was prepared in deionised water. The inner tube of the reactor was filled with an aqueous electrolyte (50 mg/l sodium chloride) solution, and a copper electrode was used to connect this liquid to an AC high voltage supply. This was then submerged into the 5 l reservoir, filled with a 10 ppm Methylene blue solution. The ground electrode was submerged in the reservoir water, thus completing the circuit. The airflow rate was 2 l/min through the gap of 1mm between the inner and outer tubes of the reactor. The control experiment was done with no applied power, while the trial run was done at 12 kV and a 3 mA current, which led to a power consumption of only 36 W. Samples were collected at 0, 15, 30 and 60 min, and analysed with a UV/Vis spectrophotometer at a fixed wavelength of 665 nm. Two other dyes were tested using this OK-3 reactor, namely Rhodamine B (UV/Vis peak at 554 nm) and Acid Orange (UV/Vis peak at 485 nm). The experimental parameters used with the OK-3 reactor are listed in Table 3.4.

Table 3.4: Experimental parameters used with the OK-3 reactor

Parameters	OK-3 on	OK-3 off
Inner quartz tube	8 OD - 6 ID	8 OD - 6 ID
Outer quartz tube	12 OD - 9 ID	12 OD - 9 ID
Voltage	12 kV AC	N/A
Current	0.003 A	N/A
Energy	36 W	N/A
Reactor length	200 mm	200 mm
<i>E. coli</i> concentration	100 colonies	100 colonies
UV-Vis	665 nm	665 nm
Electrolyte (NaCl)	50mg/l	50mg/l
Wastewater	5 l	5 l
Copper wire diameter	1.2 mm	1.2 mm
Airflow	2 l/min	N/A
N of electrode	HV one wire	HV one wire
Conductivity	5 mS/cm	5 mS/cm
pH	6	6

3.2.6 Disinfection of model solutions using OK-3

The distilled water was autoclaved and then spiked with *E. coli* at a concentration of 103 bacteria/ml (this concentration of bacteria is equivalent to a faecal coliform concentration often found in heavily contaminated surface water). 4 l of the water was placed in the 5 l water chamber of the reactor, and treated for 90 minutes. 100 ml samples were collected at 15, 30, 60 and 90 min. Disinfection results were calculated from the percentage reduction on plate colony counts in experiments compared to the control plates.

3.2.6.1 Enumeration of bacteria

The method adapted is based on conventional plating techniques used for the enumeration of bacteria (Linton et al., 1997) and was carried out using the following sequences:

- 10 ml Tryptone Soya Broth (TSB) with a single colony of *E. coli* was placed in an incubator (Incotherm) and grown overnight at 37°C, using constant agitation under aerobic conditions to the log phase.
- The 10 ml culture was thoroughly mixed using a vortex mixer (Vm-300 KIMIX), and then 1 ml of the resultant bacterial culture was transferred to a 1.5 ml micro test tube, and spun down using a centrifuge (Orto Alresa, Digicen model) set at 1300 RPM for a period of 10 min.
- The bacterial pellet was then washed three times with sterile tap water. Serial dilutions, using the bacterial pellet, were then done from 10⁻¹ to 10⁻⁶ (see Figure 3.8).
- To determine whether the 10⁻⁶ dilution produced a suitable CFU count, 1 ml of the 10⁻⁶ dilution series was transferred to an agar plate and incubated at 37°C for 24

hours. The CFU was less than 100 CFU/ml. Thus, 2.25 ml was used for further experiments to ensure adequate counts.

- A negative control plate was made by taking 1 ml of the OK-3 electrolyte solution (before spiking with *E. coli*), and plating it onto agar jelly in a 20 mm petri dish.
- 2.25 ml from the 10^{-6} dilution series was then added directly to the electrolyte (~ 5 l solution of distilled water, with 50 g/l NaCl) in the OK-3, and was allowed to stand for 30 minutes. Then 0.1 ml was collected from the spiked EDR electrolytes and added to 0.9 ml of neutralized Broth (NB) solution. This sample was plated onto agar jelly in a 20 mm petri dish to make the positive control plate.
- Sample plates were made by taking 1 ml samples after 15, 30, 60 and 90 minutes of OK-3 operation, and plating them on agar. All plates were incubated upside down at 37°C and colonies were counted after 24 hours, as illustrated in Figure 3.8 below.

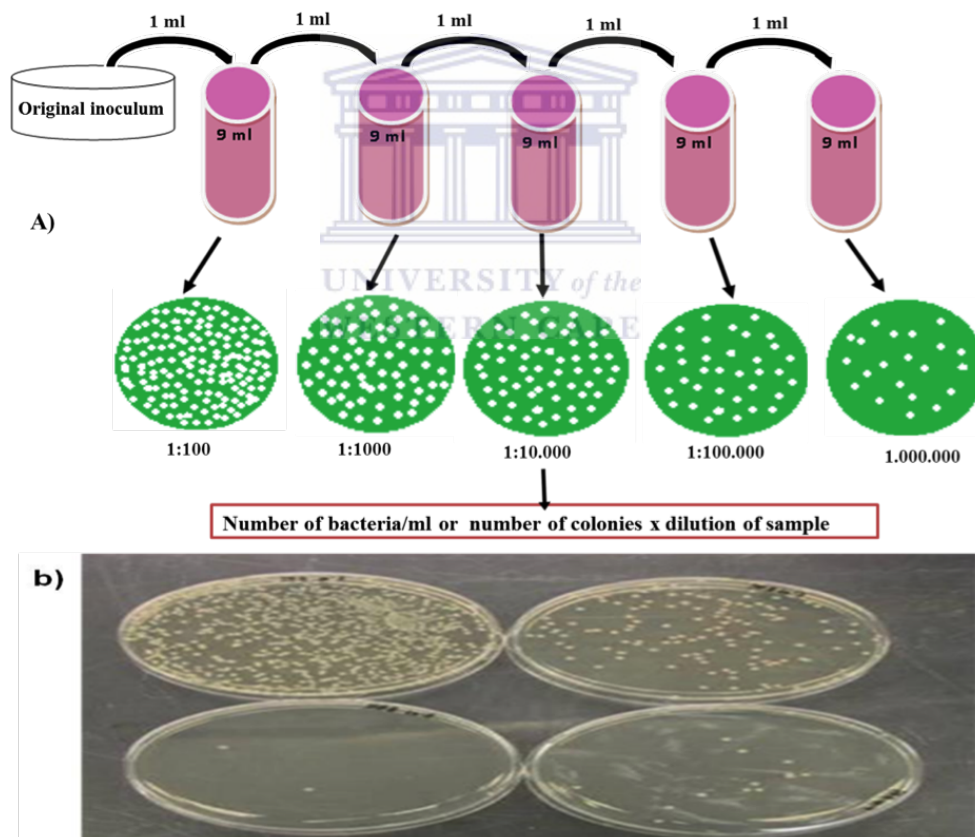


Figure 3.8: (a) Illustration of the serial dilutions used to determine suitable concentration of *E. coli* for the count number determination in subsequent plating, and (b) example of actual agar plates with *E. coli* colonies

The killing efficiency (%) in terms of the number of surviving bacteria in the sample and control plates is calculated as

$$\text{Killing efficiency} = \frac{(C - S)}{C} \times 100\% \quad (3.2.1)$$

where C is the number of colonies on the positive control plate, and S the number of colonies on the sample.

3.2.7 Solar Disinfection (SODIS)

SODIS is a drinking water treatment at point of use (POU) for the developing countries, recommended by the *World Health Organization* (WHO), UNICEF and UN to provide a safe survival level supply of drinking water from unsafe polluted water sources (Kehoe et al., 2001).

The method described is suitable for water taken from any source. A PET bottle is $\frac{3}{4}$ filled, shaken vigorously for about 20 seconds and then expose to solar irradiation for 6 hours, as shown in Figure 3.9. Like conventional ultraviolet disinfection, solar disinfection only works on water that is relatively free of suspended solids (low turbidity water). SODIS emphasizes the importance of water supply selection that is appropriate for this kind of treatment. The three effects of solar radiation, which are believed to contribute to the inactivation of pathogenic organisms are (EAWAG and SANDEC, 2002):

- Ultraviolet-A (UV-A) radiation causes damage to DNA and kills living cells.
- UV-A (wavelength 320–400nm) reacts with oxygen dissolved in the water and produces highly reactive forms of oxygen (oxygen free radicals and hydrogen peroxides), that are believed to also damage pathogens.
- Infrared radiation heats the water and causes pasteurization when the temperature is raised to 70–75°C. If the water temperature rises above 50°C, the disinfection process is three times faster.



Figure 3.9: Solar disinfection design photos (Wegelin et al., 1994)

3.2.8 Synthesis of TiO₂ nanofibres as photocatalyst

The schematic illustration of the preparation protocol which leads to the production of new photocatalyst material is presented in Figure 3.10 below. Catalysts and support materials used in this study, and how they were prepared using the sol-gel solution for electrospinning techniques, are given in Figure 3.10 and Figure 3.11.

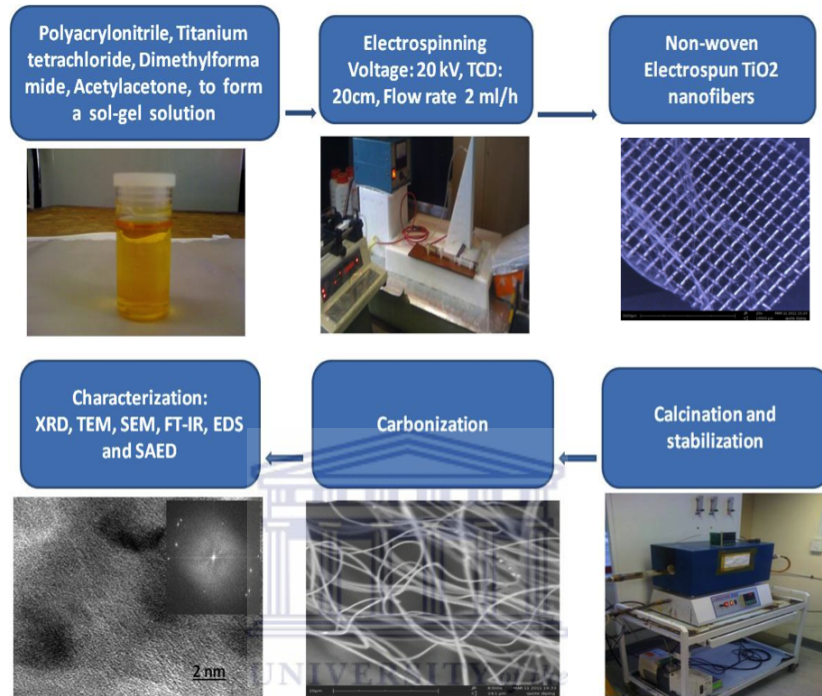


Figure 3.10: Schematic illustration of the photocatalyst preparation protocol

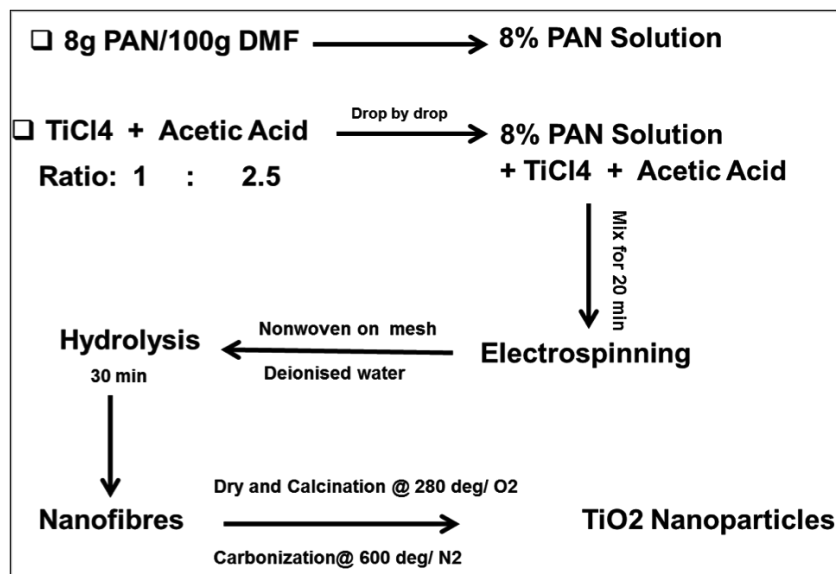


Figure 3.11: Schematic illustration of the photocatalyst preparation protocol with ratio and different temperatures

3.2.9 Preparation of electrospun nanofibres impregnated with titanium dioxide

1.5 g of Polyacrylonitrile (PAN) was added to a suitable volume of N,N dimethyl formamide (DMF), with magnetic stirring, to make an 8% PAN solution. A separate solution of 1.35 M titanium tetrachloride in a mixture of DMF and acetic acid was prepared. The molar ratio of the titanium precursor, acetic acid, was kept at 1:2.5. The precursor solution was then slowly added to the PAN solution, drop by drop, under magnetic stirring. After 15 minutes the mixture was electrospun to produce polymer nanofibers impregnated with the titanium precursor. The as-spun nanofibers were then immersed in deionised water to bring about hydrolysis of the titanium precursor.

3.2.10 Electrospinning process

The electrospun nanofibers were prepared using the setup shown in the Figure 3.10, Figure 3.11 and Figure 3.12 below. In a typical run, the prepared solution of interest was transferred to a borosilicate Pasteur pipette, and one end of a copper wire (electrode) was connected to a high voltage supply, while the other electrode was placed into the solution. Aluminium foil was used as the collection plate and grounded electrode. The distance between the tip of the Pasteur pipette and aluminium foil was fixed at 20 cm. A potential of 20 kV was applied for electrospinning at room temperature.

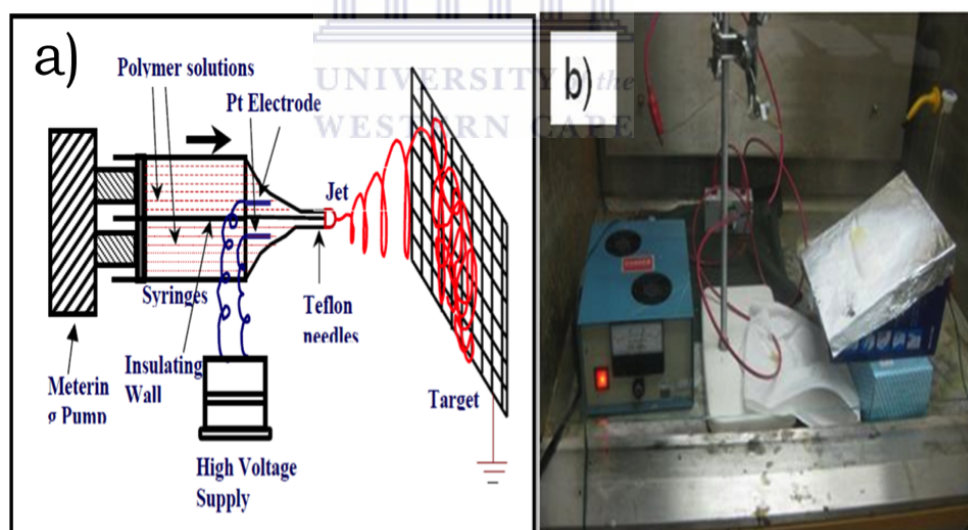


Figure 3.12: Image (a) is a schematic of the electrospinning setup, and (b) is a photograph of an experimental run

Samples for SEM, TEM and XRD studies were collected on an aluminium foil and the samples for immersion in deionized water to evaluate the photocatalytic activity were collected on a stainless steel mesh. After drying the composite fibres (in air), the samples were immersed in deionized water to hydrolyze the titanium tetrachloride precursor before the calcination.

3.2.11 Calcination of nano composite fibres

The dried TiO₂/PAN composite nanofibres were heated in air at a rate of 1°C/min and a final temperature of 280°C. Samples were maintained at the final temperature for 2 hrs.

3.2.12 Carbonization of nano composite fibres

The calcinated nanofibre composite (discussed in Section 3.2.11) were carbonized by heating the composites in a nitrogen atmosphere, using a heating rate of 5°C/min up to the final temperature of 600°C, and then held at the final temperature for 2 hrs, using the furnace shown in the Figure 3.13.

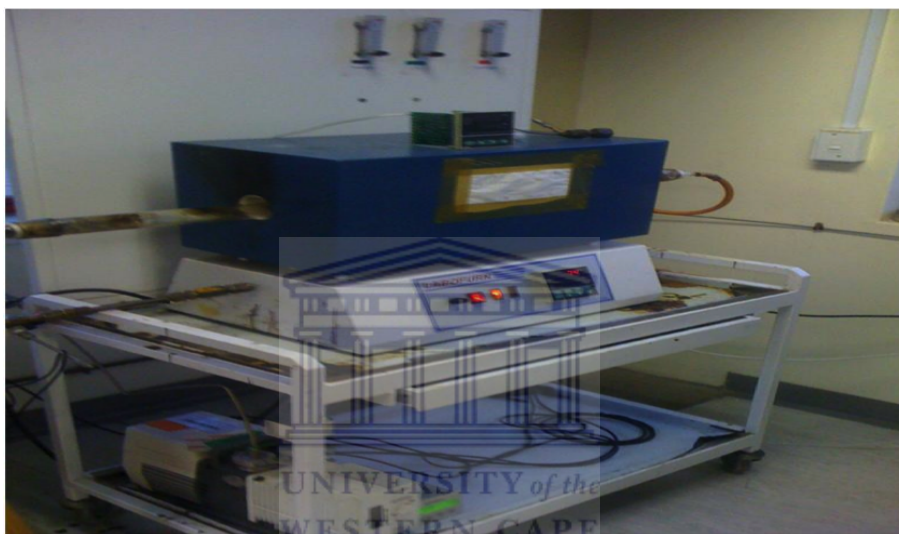


Figure 3.13: Furnace used for the carbonization of fibres

3.2.13 Sputter deposition and incorporation in the prototype OK-3

The experiment was designed in order to compare the efficiency of the as-received nanomaterial with the synthetic TiO₂ nanofibres, both incorporated in the prototype reactor OK-3 for the photocatalysis process, separately, as indicated in Figure 3.14 and 3.15.

Sputtering is a process whereby atoms are ejected from a solid target material due to the bombardment of the target by energetic particles (Behrish et al., 1981). TiO₂ (Degussa) was sputtered onto wet fibres to maximize the surface particles of the consolidated material, in order to have more UV light exposure, leading to the promotion of active species in the solution. The drawback is that there will be some nanoparticles released in the water, which leads back to the post treatment that should be avoided by using immobilization.

3.2.13.1 Methodology

Sol-gel is prepared with a 8% PAN solution. The distance between the tip of the syringe and the collecting foil material is reduced from the initial 20 cm to 12 cm. The sol-gel solution is then poured into the syringe, followed by the high voltage connection to initiate the electro

spinning process. Finally, P-25 (Degussa) powder is sputtered onto the wet electro spun fibres for 5 min. The photographs in Figure 3.14 and 3.15 show the experimental setups for the incorporation of TiO₂ nanofibres on the rig prototype OK-3. The purpose of these experiments were to explore the photocatalytic activities of the nanofibre samples without TiO₂, with TiO₂ (P25) and no carbonization, and with TiO₂ inside and carbonized in nitrogen at 600°C.

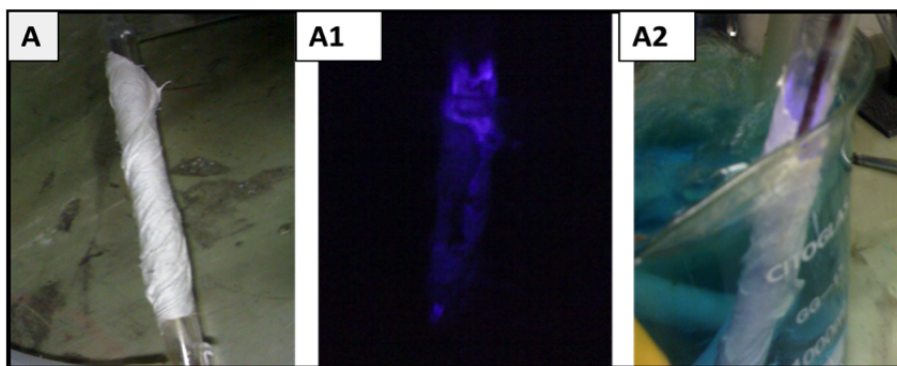


Figure 3.14: Photographs of the electrospun nanofibres without carbonization (A) wrapped on an outer tube of the rig system, (A1) connected to the high voltage power supply, and (A2) the wrapped rig submerged into the contaminated water with MB (10 ppm).

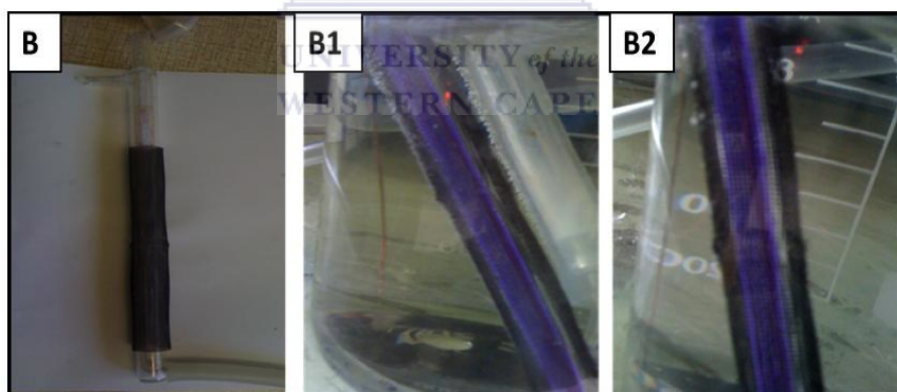


Figure 3.15: Photographs of the TiO₂ nanofibres electrospun on grid supporting material and carbonized in nitrogen at 600°C, (B) bent on the outer tube of the rig system, (B1) connected to the high voltage power supply, and (B2) the rig submerged in the contaminated water with MB (10 ppm).

3.3 Physical characterization techniques and experimental details

3.3.1 Introduction

Various techniques were used to characterize the synthesized catalysts. The aim of these characterization methods was to study the physical and chemical properties of the materials. These techniques that were used are High Resolution Scanning Electron Microscopy (HRSEM), Energy Dispersive Spectroscopy (EDS), Brunauer-Emmett-Teller N₂ Adsorption

(N₂BET), High Resolution Transmission Electron Microscopy (HRTEM), Selected Area Electron Diffraction (SAED), X-ray Diffraction (XRD). A summary of the analytical techniques used and the information they provide is given in Table 3.5 below.

Table 3.5: Summary of characterization techniques used during catalyst development

Method	Function
Fourier Transform Infrared Spectroscopy (FTIR)	Identification of hydroxyl peaks present
X-Ray Diffraction (XRD)	Crystallinity, particle size and phase analysis
High Resolution Transmission Electron Microscopy (HRTEM)	Crystallinity and particle size
Scanning Electron Microscopy (SEM) & Energy Dispersive Spectroscopy (EDS)	Surface morphology and elemental composition
Selective Area Electron Diffraction (SAED)	Crystallinity and crystal symmetry
Braunner-Emmet-Teller (N ₂ BET)	Surface area, pore diameter and pore size distribution

3.3.2 Fourier Transform Infra-Red Spectroscopy

3.3.2.1 Experimental details: Sample preparation

10 to 15mg of the sample was subjected to FTIR analysis. The sample was placed directly over the FTIR probe. The sample was placed directly over the FTIR probe and the FTIR spectrum of the particular sample was obtained. The experimental conditions are given in Table 3.6.

Table 3.6: FTIR experimental instrument conditions

Instrument Name	Perkin Elmer Spectrum 100 series FT-IR
Range	380–4000 cm ⁻¹
Scan number	4
Units	Absorbance
Resolution	4 cm ⁻¹

3.3.3 X-Ray Diffractometer

3.3.3.1 Experimental details: Sample preparation

The powder material was mounted on a sample holder, levelled using a spatula and then put into the X-ray diffraction instrument. The instrument specification is listed in Table 3.7.

Table 3.7: The Siemens D8 Advance XRD operational parameters

Parameter	Conditions
X-ray detector	Copper tube with Cu-K α
Generator voltage	40 kV
Generator current	40 mA
Scanning range	2 θ angle
Scan type	Locked coupled
Scan speed	60 s/step
Scan time	6 hrs
Step size	0.2°
Wavelength	1.54 Å

3.3.4 High Resolution Scanning Electron Microscopy (HRSEM)

The nanophase material of interest was supported on double-sided conductive carbon tape and mounted on a sample stub. No sputter-coating was required, as all the nanophase material in the study were electron-conductive. Samples were fitted into the vacuum chamber of the microscope (HRSEM, Zeiss Ultra 55 Field Emission – In-lens detection). High Resolution Scanning Electron Microscopy was used to probe the surface micro- and macro structure, and determine the degree of agglomeration.

3.3.4.1 Experimental details: Sample preparation

15 mg of the sample was placed in a specially designed sample holder and this was mounted in the HRSEM instrument. The experimental conditions are listed in Table 3.8.

Table 3.8: HRSEM instrument experimental parameter settings

Parameter	Conditions
Accelerating Voltage	30 kV
Current	10 nA
Emitter	Thermal field emission type
Aperture	0.4 mm
Resolution	1 nm
Standard detector	ESB with filtering grid
Magnification	900K

3.3.5 High Resolution Transmission Electron Microscopy (HRTEM)

3.3.5.1 Experimental details: Sample preparation

The HRTEM samples were prepared by dispersion of a spatula-tip of the catalyst of interest in a 5 ml methanol solution, followed by sonication of the suspension. One drop of the suspension was deposited on holey carbon grids and allowed to dry for 15 minutes. The

methanol was allowed to evaporate at room temperature. Samples were mounted in a sample holder that was introduced into the shaft of the electron microscope. The experimental conditions are listed in Table 3.9.

Table 3.9: HRTEM instrument experimental conditions

Name of instrument	Tecnai G2 F20 X-Twin Mat FEGTEM
High tension	200 kV
Extraction voltage	3950 V
FEG emission current	54 μ A
Condenser aperture	3 mm
Objective aperture	2 mm
Gunlens	1 nm
Spot size	3 nm
Imaging with TIA CCD camera	TIA=TEM Imaging and Analysis

3.3.6 Brunauer-Emmet-Teller (BET) N₂ adsorption

3.3.6.1 Experimental details: Sample preparation

The surface area, pore volume and pore size distribution of the samples were determined by means of the Brunauer-Emmet-Teller (N₂ BET) technique, using a Micrometrics Accelerated SA and Porosimetry (ASAP) 2010 system. Approximately 100 mg of the sample was transferred and sealed in a sample tube.

The samples were degassed and dried at 90°C for 2 hrs, and at 2000°C overnight in nitrogen in order to remove moisture and to free the pores of any particles. The experiment was conducted isothermally at -196°C with a constant N₂ flow applied during the analysis.

3.3.7 Energy Dispersive Spectroscopy (SEM-EDS)

The elemental composition of the catalysts was investigated using energy dispersive spectroscopic (EDS) emission analysis with a Hitachi X-650 SEM. Relative element concentrations were estimated using GENESIS software. Every sample was scanned five times to obtain the average wt. % of the metal. The operating parameters of the SEM are described in Table 3.10.

The conductive powders of the catalytic samples were dispersed upon the carbon stick tabs and mounted on an aluminium stub holder. After that, the holder was loaded into the spectrometer.

Table 3.10: Hitachi X-650 SEM operational parameters

Parameter	Setting
Accelerating voltage	25 keV
Tilt angle	0°
Aperture	0.4 mm
Resolution	3 nm
Working distance	15 mm
Magnification	50k

3.4 Measurement of photocatalytic activity

Catalysts speed up chemical processes and photocatalysts must also be able to absorb the irradiation from the sunlight. The emphasis in this research is not to rely on sunlight or any UV lamps, but the irradiation from a novel designed reactor, based on corona discharge principles. Upon doing so, the light energy causes the excitation of electrons. The electrons are more reactive after excitation, which is why they leave electron 'holes' (Hoefelmeyer et al., 2011).

In this study the simple reactor arrangement is based on a high voltage of 15 kV at a frequency of 30 kHz. UV irradiation, as described in Section 3.2.3.3, was used for the photocatalytic degradation of Methylene blue (MB). UV-Vis spectrometry was thereafter used to determine the extent of MB dye degradation by photocatalysis on the prepared TiO₂ nanofibers catalysts, as described in Section 3.2.8. Photo-degradation, pH, time, airflow in the reactor and dye concentration studies were carried out as reported in Sections 3.4.1 – 3.4.3, respectively.

3.4.1 pH

The measurement of pH was done using a HANNA HI 991301 portable pH/EC/TDS (Hanna Instruments, RSA). The pH meter was calibrated according to the manufacturer's instructions before use.

The experiments were carried out to find the optimal pH of the reaction mixture for optimum photocatalysis. A 50 mg/l concentration of MB dye solution was degraded using the OK-3 reactor. The examined range of pH was from 0 to 14, with a reaction time of 60min. The pH was adjusted using a solution of 0.1M NaOH or 0.1M H₂SO₄.

3.4.2 Concentration of the dye

Experiments were carried out with different MB concentrations, expressed in ppm (15, 30, 60 and 100), with TiO₂ NF carbonized at 600°C and pH=8. The experiments were carried out in duplicate.

3.4.3 Analysis of the catalytic degradation achieved

The Spectronic 20 UV-Vis Spectrophotometer (GxP, USA) was used to measure the absorbance (Abs) of the solution recorded after the photocatalytic degradation experiments, as specified in previous sections. The absorbance of MB at various concentrations was measured at a fixed wavelength (665 nm). The concentrations

$$c = \frac{\text{Abs}}{\text{Slope of calibration curve}} \quad (\text{ppm}) \quad (3.4.1)$$

were then calculated for each sample and expressed in ppm.

The % MB removal obtained was calculated from

$$\% \text{ Removal of MB} = \frac{c_0 - c}{c_0} \times 100\% = \left[1 - \frac{c}{c_0}\right] \times 100\% \quad (3.4.2)$$

where c_0 is the initial concentration of the Methylene blue and c is the concentration of the Methylene blue after the photocatalytic reaction. Therefore, if standard MB used is 10 ppm, then $c_0=10$ ppm.

3.5 Detection of chemicals from the aliquots

In order to determine what the killing factors in the solution were, electron spin resonance (ESR) and methanol were used as detection methods for OH radicals. Ozone detection was done using the iodometric method and hydrogen peroxide was detected by the colorimetric method proposed by Eisenberg.

3.5.1 Sample preparation for ESR detection of hydroxyl and superoxide radicals

For ESR spin trapping of hydroxyl and superoxide radicals, TiO₂ nanofibres were deposited on the grounded grid using the electrospinning process and the produced fibres were then wrapped around the outer tube of the reactor, which generated UV irradiation, and which was submerged in artificially contaminated water. The standard commercially available spin trap, 5, 5-dimethylpyrroline-1-oxide (DMPO), from Sigma, was used for the ESR detection of hydroxyl and superoxide radicals. The obtained stock solution of 0.5 M DMPO in ultra-pure water was stored at -20°C. Immediately before performing the ESR measurements, 1 ml of the water aliquot was collected and mixed with 2 drops of DMPO stock solution to achieve the final spin trap of radicals. Subsequently, the 1 ml aliquot of UV exposed water was transferred to a small quartz capillary disposable micropipette with ring mark from VitroCom, NJ, USA (sample height of 25 mm) and sealed on the top end. ESR experiments were carried out at room temperature, using an ESP300E spectrometer (Bruker BioSpin GmbH), equipped with a standard rectangular mode TE102 cavity. Routinely, for each experimental point, five-scan field-swept ESR spectra were recorded. The typical instrumental setting were: microwave frequency 9.38 GHz, microwave power 2 mW, sweep width 120 G, modulation frequency 100 kHz, modulation amplitude 0.5 G, receiver gain 4×10^4 , time constant

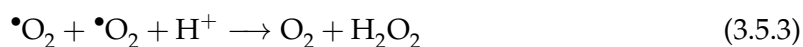
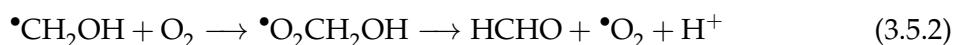
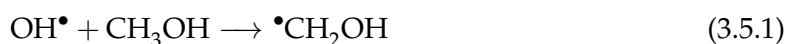
20.48 ms, conversion time 40.96 ms and time per single scan 41.9 s. Measured ESR signals revealed the presence of the characteristic signal of DMPO-OH only when TiO₂ nanofibres were exposed to UV light. Figure 3.16 shows a photograph of the ESR apparatus used.



Figure 3.16: Photograph of the ESR apparatus used in this study for OH radical detection

3.5.2 Methanol as OH radical scavenger

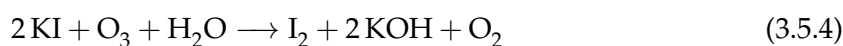
Methanol can be used as an OH radical scavenger (Popov et al. 2010). However, methanol will react with other radicals generated, or any methanol type radicals generated will react with other radical species. According to previous studies of photocatalytic methanol oxidation, formaldehyde was the only stable product formed initially under reaction conditions employing an excess of methanol and hydroxyl radicals (Sun et al. 1996). Consequently, the amount of methanol oxidized is identical to that of the detected formaldehyde concentration (ratio 1:1). The mechanism reaction of hydroxyl radical scavenged by methanol to form the formaldehyde is as follows:



In order to elucidate the main factors affecting the activity of these radicals, additional experiments at higher methanol concentrations were carried out, using the disinfection method of *E. coli* microorganism analysis, according to the protocol experiment in discussed in Section 3.2.6.1.

3.5.3 Ozone detection

Ozone (O_3) is a very strong oxidising agent, corrosive and can be produced by flowing air through the corona discharge area. It can easily be detected using the iodometric method, that involves bubbling the effluent gas from the discharge through a 0.1M aqueous solution of potassium iodide. To assess the total amount of ozone produced during the streamer discharge in this case, the ozone was collected in a gas plenum above the reactor and ventilated through a bottle filled with an iodide solution. The ozone reacts with the potassium iodide solution and forms a yellow iodine complex.



The solution changes from a yellow colour to dark orange as the ozone concentration increases.

Preparation of KI solution: 0.1M of KI was mixed in 1 l of Millipore water, stirred and kept in the dark.

Experimental method: The formation of the iodine complex is determined by measuring the absorbance of a sample in a cuvette with a photo spectrometer. The ozone concentration trapped in a 10 ml volume of the KI solution was determined. This measurement can only give a rough estimate of the ozone leaving the reactor, since the gas retention time is too short to lead to a complete reaction between the saturating ozone and the KI solution. Figure 3.17 shows the setup used for ozone and hydrogen peroxide detection, where only the electrolyte needs to be changed, respectively.

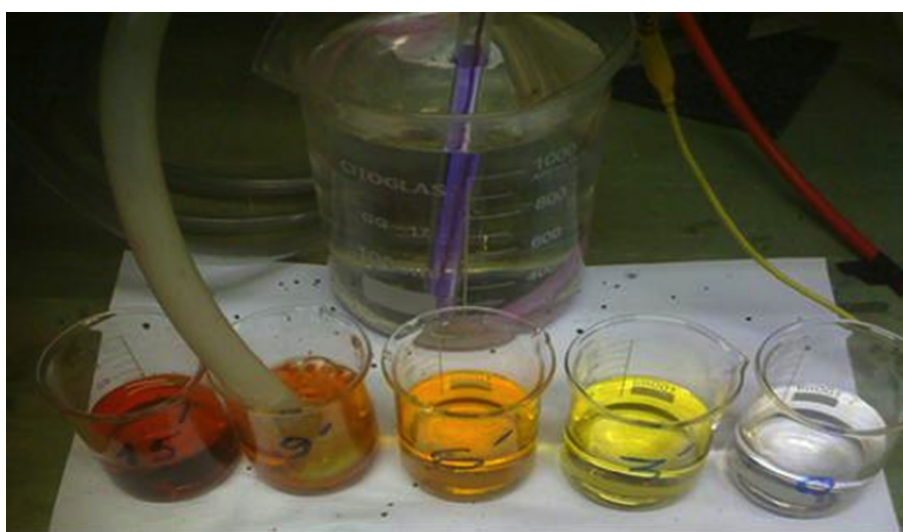
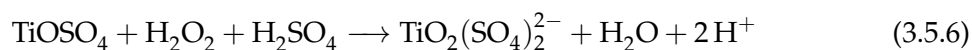


Figure 3.17: Setup for the detection of ozone and hydrogen peroxide

3.5.4 Hydrogen peroxide detection

The most stable and abundant oxidant appearing in corona discharge is hydrogen peroxide (H_2O_2). Due to their short lifetime, OH radicals have to be detected during streamer discharge, before they combine to form more H_2O_2 . In contrast, the determination of H_2O_2 can be performed during the discharge phase. H_2O_2 plays an important role in the disinfection of water. In the bulk solution it can react with other species and produce OH radicals. The Eisenberg method was used to determine the production of hydrogen peroxide in the electrohydraulic corona discharge reactor OK-3.

The well-known colorimetric method proposed by Eisenberg (Eisenberg et al., 1943) is based on the photometric analysis of the intense yellow-orange colour appearing in a solution containing hydrogen peroxide, after the addition of titanium sulphate. The yellow colour produced is due to peroxotitanylsulfonic acid. The reaction of H_2O_2 with the reagent takes place as follows:



3.5.5 Ion Chromatography (IC)

Ion chromatography (IC) is a form of liquid chromatography that uses ion-exchange resins to separate atomic or molecular ions based on their interaction with the resin. Its greatest use is for the analysis of anions for which there are no other rapid analytical methods. Ion chromatography is used for analysis of aqueous samples in parts-per-million (ppm) quantities of common anions, such as fluoride, chloride, nitrite, nitrate and sulphate, and common cations such as lithium, sodium, ammonium, and potassium, using conductivity detectors. The chromatograph also has the capability to analyze aqueous samples in parts-per-billion (ppb) quantities. Ion chromatography is a form of liquid chromatography, where retention is predominantly controlled by ionic interactions between the ions of the solute and counter ions that are situated in, or on, the stationary phase. For example, to separate organic acids, it is the negatively charged acid ions that need to be selectively retained. It follows that the stationary phase must contain immobilized positively charged cations as counter ions to interact with the acid ions to retain them. Conversely, to separate cations, the stationary phase must contain immobilized anions as counter ions with which the cations can interact. Ion exchange stationary phases are available in mainly two forms. One form (probably the most popular) consists of cross-linked polystyrene polymer beads of an appropriate size, which have been suitably treated to link ionic groups to the surface. The other form is obtained by chemically bonding ionic groups to silica gel by a process similar to that used to produce bonded phases. These materials are called ion exchange media, a term which has given rise to the term "ion exchange chromatography" as an alternative to ion chromatography. Ionic substances can also be adsorbed on the surface of reverse phase media and act as an adsorbed ion exchanger. The mobile phase is made to contain a small percentage of soluble organic ionic material (e.g. tetrabutyl ammonium dihydrogen phosphate or n-octyl sulphonate). These substances are adsorbed onto the surface by dispersive interactions be-



Figure 3.18: Photograph of the Ion Chromatograph used in this study

tween the alkyl groups of the agent and those of the bonded phase, and act as counter ions. In general ion chromatography is one of the more difficult types of liquid chromatography to exploit and is most often used for analysis of anions for which there are no other rapid analytical methods (Dionex et al., 1998).

3.5.5.1 Procedure

The treated water, collected after passing through the reactor, was filtered through a $0.45\ \mu\text{m}$ membrane filter to remove suspended solids and then diluted with de-mineralized water to obtain EC values of between 50 and $100\ \mu\text{S}/\text{cm}$. SO_4^{2-} , Cl^- , NO_3^- and PO_4^{3-} were analysed in the leachates, using a Dionex DX-120 ion chromatograph, as shown below in Figure 3.18, with an Ion Pac AS14A column and AG14-4 mm guard column.

Chapter 4

Results of prototype design

This chapter starts by presenting a brief motivation for conducting studies on the design and construction of an electrohydraulic discharge system that promotes the in-situ production of active species, such as OH radicals, ozone and hydrogen peroxide, to avoid handling chemicals and cost. The physicochemical properties, based on water conductivities, pH and UV irradiation are presented. A step-wise optimization process for the degradation of dyes, such as Methylene blue, Rhodamine blue and acid orange are presented. The characterisation results on the total degradation of Methylene blue, using UV spectroscopy, FT-IR, LC-MS and NMR are also presented and discussed. The results for microbial analysis on river water and microbial disinfection efficiency of the prototype OK-3, compared to solar disinfection (SODIS), are also presented and discussed.

4.1 Motivation

As indicated in the introduction of this study, conventional water and wastewater treatment processes have been long established in removing many chemical and microbial contaminants of concern for the improvement of living conditions of the population in developing countries. However, the effectiveness of these processes has become limited over the last two decades, due to the identification of more and more emerging contaminants, rapid growth of the population, industrial activities, and the diminishing availability of water resources. This constitute new challenges for drinking water supplies (Langlais et al., 1991; Mallevalle et al., 1996). The first experimental investigations on dielectric-barrier discharge were reported by Siemens et al. (Siemens et al., 1857). They concentrated on the generation of ozone. This was achieved by subjecting a flow of oxygen or air to the influence of a dielectric-barrier discharge (DBD), maintained in a narrow annular gap between two coaxial glass tubes by an alternating electric field of sufficient amplitude. Other researchers concentrated their research on corona discharge for water treatment (Lukes et al., 2001), (Mayank et al., 2006), (Gupta et al., 2007). It is important to mention that most of the aforementioned studies either produced ozone with high energy consumption or were not suitable for industrial applications, because they required high activation temperatures. It is on this basis and understanding that studies presented in this chapter was pursued to design a novel

prototype reactor, based on same corona discharge, using a submerged electrode configuration, in order to promote the in-situ production of a cocktail of active species, such as ozone, hydroxyl radicals, hydrogen peroxides and others at low energy consumption.

4.2 Degradation of Methylene blue using different prototypes reactors

Generally, three different prototype reactors were designed, one at a time, each based on the same corona discharge principles, but having different configurations and materials. The changes in the reactor designs were made after testing them for the degradation of dye, as well as establishing their individual limitations. This led to the modifications, in order to try to avoid the identified drawbacks.

The identified conditions for continuous UV irradiation further built a platform for an in-depth study aimed at understanding and applying a catalyst for the photocatalysis process, to improve the system by the formation of more active species (to be presented in Chapter 5). Out of the many known prototypes that have been designed by other researchers, as presented in a review article (Locke et al., 2006), the main reason for identifying the prototype OK-3 as the design target, was based on its huge commercial importance in applications such as catalysis for water treatment. The results and limitations of the prototype reactors are highlighted in Sections 4.2.1, 4.2.2 and 4.2.3.

4.2.1 Prototype made with PVC (OK-1)

The reactor OK-1 has three principal components. The first is an AC power supply connected in series to different electrodes (see Section 3.2.3.1 and Fig. 3.3). It is geometrically designed in such way that the high voltage electrodes were on top of the glass and the ground plate was positioned on the other side of the glass. A small pump was used to allow water circulation passing through a 1 cm gap between two glass plates, and lastly a 5l discharge chamber that contained the solution to be treated. The electrode gap in the reaction chamber was typically 1 cm and could be varied from 1 to 5 cm gap length with an adjustable electrode assembly.

4.2.1.1 Results on the effectiveness of OK-1

As indicated in Section 3.2.4 and Table 3.3, the degradation experiment of 10 ppm MB took place under the following conditions: 12 kV at 3 mA (36W power), a flowrate of 100 ml/min and a pH of 6, with a running time of 60 minutes. The control experiment, without power, showed no decrease in the Methylene blue concentration after 60 minutes. In contrast, with the power switched on, the concentration in Methylene blue decreased by 10% in 30 minutes, but no further decrease was observed from 30 minutes to 60 minutes, as shown in Figure 4.1 below.

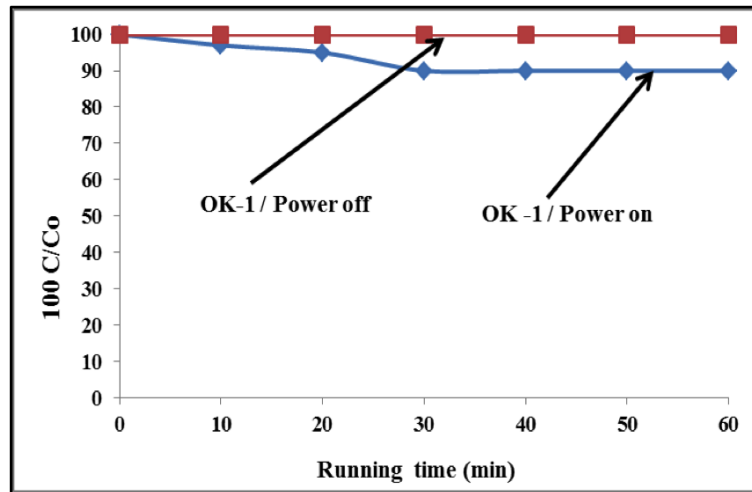


Figure 4.1: The measured degradation of MB (10 ppm) using OK-1, under the following conditions: 12 kV at 3 mA, pH 6, flowrate of 100ml/min

The poor degradation of Methylene blue using OK-1 could be attributed to the fact that the ozone that was produced at the contact of the electrode with air, producing ozone which spread outside in the air, without entering the water to be treated. All the ozone produced was thus emitted into the air, and not in the water, due to the position of the electrodes outside in the air. This led to the poor energy consumption.

Thus, the reason for pursuing and implementing a new design (i.e. prototype OK-2) was due to the limited degradation of Methylene blue after 60 minutes of continuous operation, and the large heat generation was used as an indirect indication of the reactor's inefficiency.

4.2.2 Prototype made with Perspex (OK-2)

As indicated in Section 3.2.3.2, Figure 3.4 and 3.5, the OK-2 design was made based on corona discharge principles discussed in the review, using perspex to machine down grooves to the desired gap distance (i.e. 1 mm) between two electrodes, thus avoiding the limitations from prototype one. It is well known that the gap between the electrodes and the dielectric material is among the most important parameters for efficient electrical discharge. It is also important to note that, in this design, the electrodes were covered by bees wax on each groove, as indicated in Section 3.2.3.2, to overcome energy wastage. Methylene blue (10 ppm) was used as model pollutant to check the degradation effectiveness of the OK-2 reactor under the following operating conditions: 12 kV at 3 mA (36W power), a flowrate of 100 ml/min and a pH of 6, with a running time of 60 minutes.

4.2.2.1 Results on the effectiveness of OK-2

From an engineering point of view, this prototype satisfies the entire requirement to overcome all drawbacks from prototype OK-1, to produce active species and a high electric field to be used for water treatment. Using the same parameters and conditions as previously

used for prototype OK-1, the experiment was carried out with a power supply, and without one as controlled experiment.

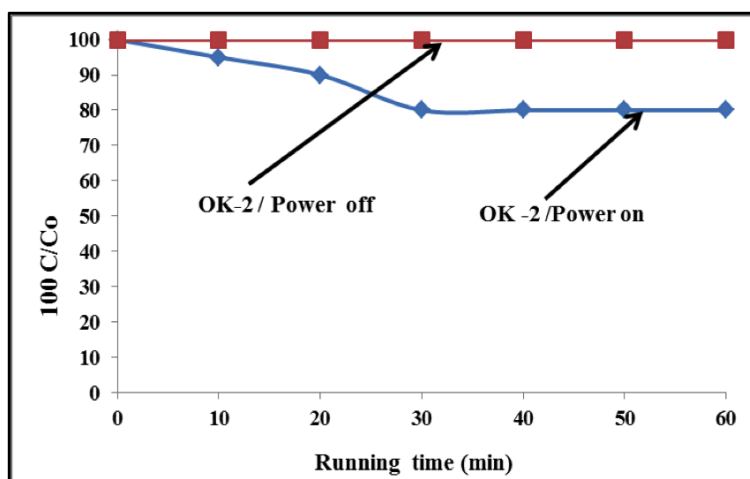


Figure 4.2: The measured degradation of MB (10 ppm) using OK-2, under the following conditions: 12 kV at 3 mA, pH 6, flowrate of 100 ml/min.

The control experiment, without power, showed no decrease in Methylene blue concentration after 60 minutes. In contrast, with the power switched on, the concentration in Methylene blue decreased by 20% after 30 minutes, but no further decrease was observed after 60 minutes. However, the Perspex cell began to melt due to the excessive heat generated by the high voltage electrodes during the application of power to the system, leading to a high electric field (Locke et al., 2006). When melting, water flows through the electrodes in the groove, stopping any electric discharge that produce plasma, which has the role of splitting water to active species, to attack and destroy organics, even microorganisms.

Thus, the reason for pursuing and implementing a new design (i.e. prototype OK-3) was due to the limited degradation of Methylene blue after 60.0 minutes of continuous operation. The excessive heat generated on the electrodes was also a problem, as it led to the melting of the Perspex components, indicating the reactor's inherent design inefficiency. Compare to OK-1, OK-2 showed slightly better MB degradation. This was due to the fact that in the electric discharges were total, leading to the full electric field across the water to be treated, without losses of energy in the closed environment. The goal of this study was to find a prototype with a total degradation of dye and inactivation of microorganisms.

4.2.3 Prototype made with quartz glass (OK-3)

As indicated in Section 3.2.3.3, Figure 3.6, Table 3.4 and the effectiveness Section 3.2.5 in Chapter 3, under the same parameters and conditions as in OK-1 and OK-2, the design was made based on corona discharge principles, using a quartz glass tube as dielectric material for UV transparency to allow the recovery of the ozone and to diffuse it into wastewater. Methylene blue was used as pollutant model to check the degradation effectiveness of the OK-3 prototype reactor. The identified conditions for continuous UV irradiation

further built a platform for an in-depth study aimed at understanding and applying a catalyst for the photocatalysis process, to improve the system by the formation of more active species. This novel prototype reactor OK-3 was able to run for several hours without any further damage or drawbacks, as compared to OK-1 and OK-2. The use of quartz glass enabled the emission of UV irradiation and produced in-situ ozone, OH radicals, hydrogen peroxide and others, in cocktail form, to attack and kill organics, microorganisms etc.

4.2.3.1 Effectiveness of OK-3 with dye solutions

From an engineering point of view, this prototype satisfies all the requirements to overcome the drawbacks of prototype OK-1 and OK-2. To test the efficiency of prototype OK-3, the same parameters and conditions as previously used were chosen to conduct the experiment, with a power supply and without, as control experiment. Methylene blue, Rhodamine blue and acid orange were used as model pollutants to check the degradation effectiveness of the OK-3 reactor under the following operating conditions: 12 kV at 3 mA (36W power), a flowrate of 2l/min and a pH of 6, with a running time of 60 minutes.

Control experiments, without power, showed no decrease in dye concentrations. All three dyes were completely decolorized after 30 minutes, with power supplied, as shown in Figure 4.3. FTIR runs on samples after the various experimental decomposition times did see a significant decrease or disappearance in the characteristic peaks for the respective dyes. This does suggest that the dyes were decomposed and did not simply undergo a simple redox reaction to make them inactive in the UV/Vis region. Further tests to determine whether the dyes did decolorize or demineralize, were done using LC-MS. With LC-MS, Methylene blue and Rhodamine B were easily detected in the control runs. However, after 30 minutes, using NMR, no carbon compounds were found in the sample. This strongly suggests that the samples were completely decomposed i.e. converted to carbon dioxide, water, and the respective elements and compounds (e.g. nitrogen, NO_x, or SO_x).

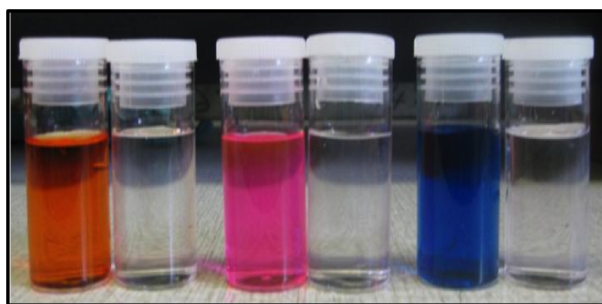


Figure 4.3: Degradation of acid orange, Rhodamine blue and Methylene blue (respectively from left to right) under the following conditions: 12 kV at 3 mA, pH 6, flowrate of 2l/min

UV-Vis measurements were taken for each dye after 30 min of running time and the results are presented below in Figures 4.4, 4.5 and 4.6. The purpose of these experiments was to show the performance of the designed reactor OK-3, regardless of the nature and composition of the dyes as pollutants.

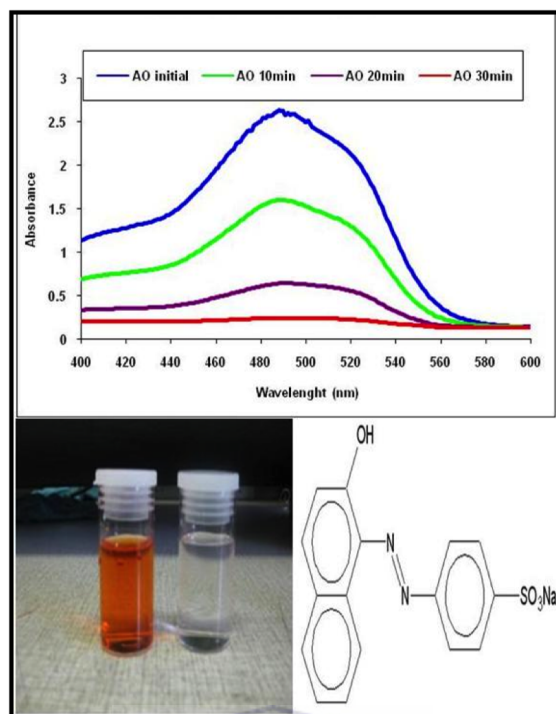


Figure 4.4: UV-Vis result of the degradation of acid orange (4-(2-Hydroxynaphthylazo) benzenesulfonic acid sodium salt) (λ_{max} = 485 nm)

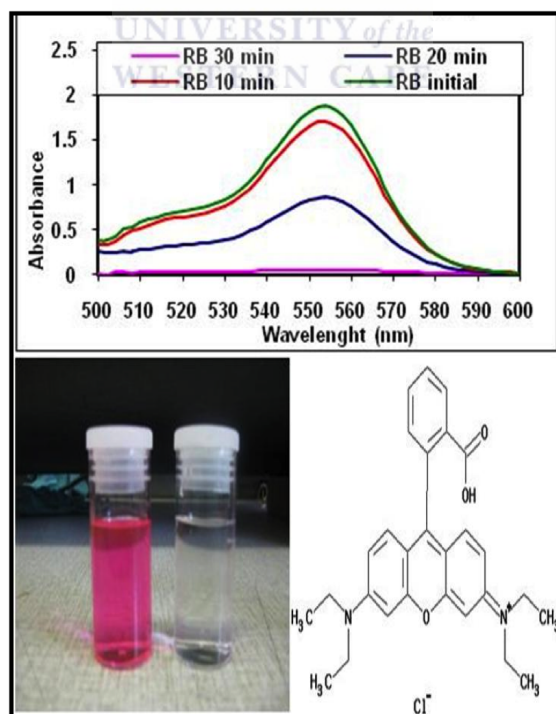


Figure 4.5: UV-Vis result of the degradation of Rhodamine blue(3', 6'-Bis (diethylamino) spiro[isobenzofuran-1(3H), 9'-[9H]xanthene]-3-one) (λ_{max} = 554 nm)

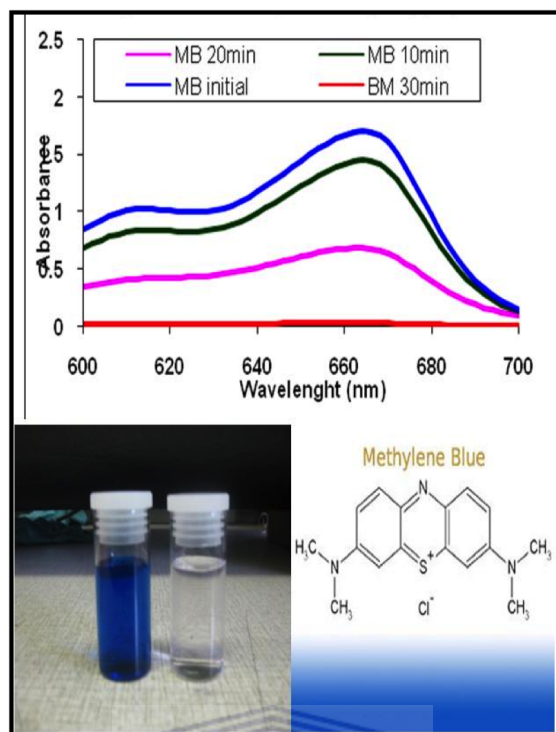


Figure 4.6: UV-Vis result of the degradation of Methylene blue (3,7-bis(Dimethylamino)-phenothiazin-5-ium chloride) ($\lambda_{max} = 665 \text{ nm}$)

4.2.3.2 Influence of water conductivity

During electric discharge, where corona energizes the plasma that ionizes and splits water, leading to the formation of UV and active species, the conductivity of the water is very important (Locke et al., 2006). The purpose of this experiment was to identify which dielectric material would maximize the UV light exposure, based on the conductivity of the water to be treated. The electrolytes used were NaCl and CuSO_4 , while using quartz and Pyrex glass as dielectric material. For the in-situ production of oxidants, the conductivity and dielectric material play a key role. It was observed that the UV irradiation from the streamer in water depends upon the water conductivity and also on the nature of the dielectric material. Due to the polarization effects and streamer formation, as a function of time, during corona discharge, the conductivity of water may change. To see the effects of streamer formation on the signal shape, one unit setup reactor has been used at a constant AC voltage of 15 kV. The measured results are shown Figure 4.7 and 4.8.

As shown in Figure 4.7 and 4.8, the increase of discharge light above the water is due to an increase of KCl salt concentration $C1 [0.1\text{M}] > B1 [0.01\text{M}] > A1 [0.001\text{M}]$. The increase of UV radiation is due to an increase of KCl salt concentration $C [0.1\text{M}] > B [0.01\text{M}] > A [0.001\text{M}]$. This observation leads to the conclusion that more salt in the water will increase the discharge above the water, and also increase the UV light, which is important for the photocatalysis process without relying on sunlight or on UV lamps. The observations shown in Figure 4.7 and 4.8 correlate well with the findings of other researchers (Lukes et al., 2001).

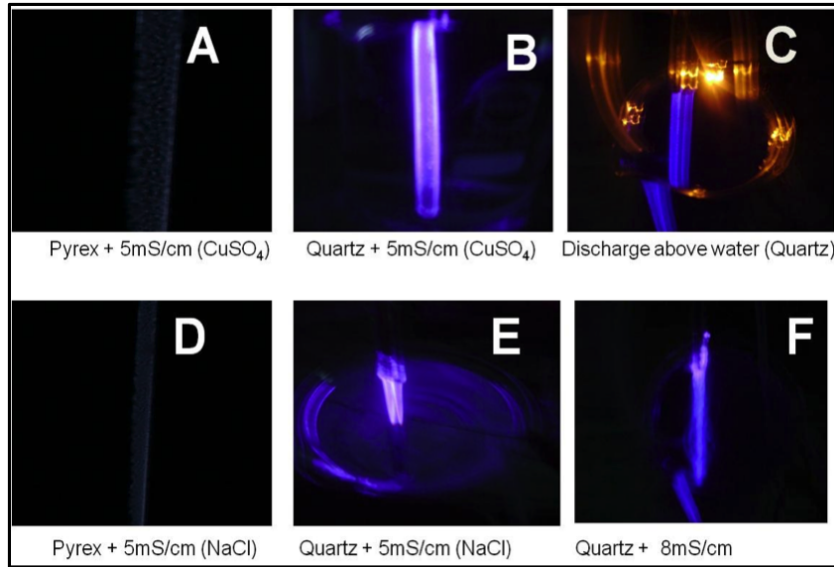


Figure 4.7: Dependence of UV transparency on dielectric materials, such as Pyrex and Quartz, using different electrolytes such as NaCl and CuSO₄

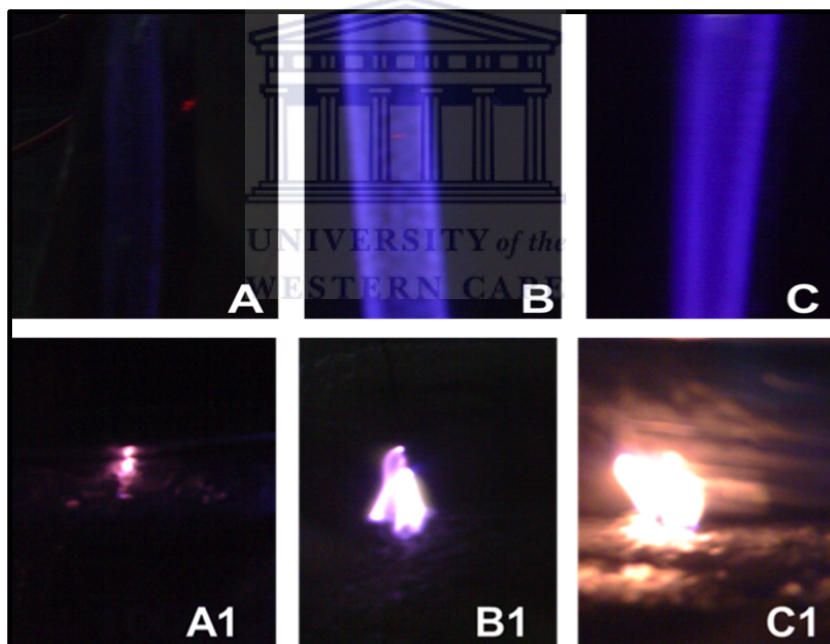


Figure 4.8: Influence of electrolyte on the UV irradiation and discharge light above the water

4.2.3.3 Corrosion

The purpose of this experiment was to see whether deterioration or mass loss, in other words the erosion of the copper electrodes, occurred after a long period of electric discharge. The prototype reactor OK-3 was used at an AC voltage of 15 kV at 3 mA and a frequency of 25 kHz. The conductivity was kept at 5 mS/m and 5 l of water was used. Based on the principle of thermal conduction, copper was chosen as the material for the high current discharging electrode. Experimental results indicated that the mass loss and surface erosion morphology of the electrodes are related to the electrode material (conductivity σ and thermal capacity

c) and the impulse transferred charge (or energy) per discharge for the same total impulse transferred charge. The electrode erosion mechanism under high energy impulse arcs on the tip was analyzed briefly and it is suggested that, by selecting a highly conductive metal or metal alloy as the electrode material for a high energy impulse spark gap switch, and selecting a highly corrosion resistant material for the tip of the electrode, the mass loss of the electrode can be reduced and the life of the switch prolonged.

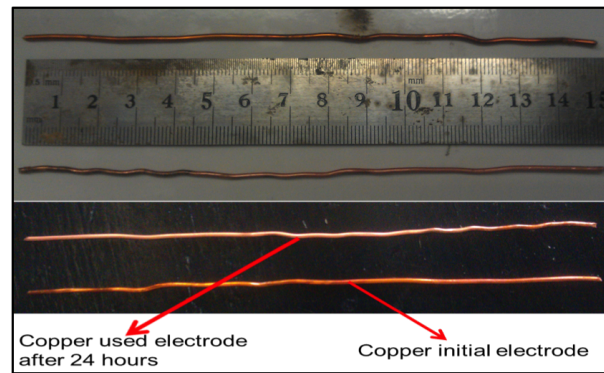


Figure 4.9: Photograph of the initial copper electrode and after 24 hours of use

Regardless of the electric discharge due to the high voltage between the two electrodes, and the high conductivity of the water to be treated in the reactor, it was found that the electrodes did not suffer from corrosion or mass loss during the tested time, as highlighted by others researchers (Gupta and Bluhm, 2007, Locke, et al., 2006).

The following results indicate the dependency of pH and the conductivity of the water on electric discharge, as shown in Figure 4.10.

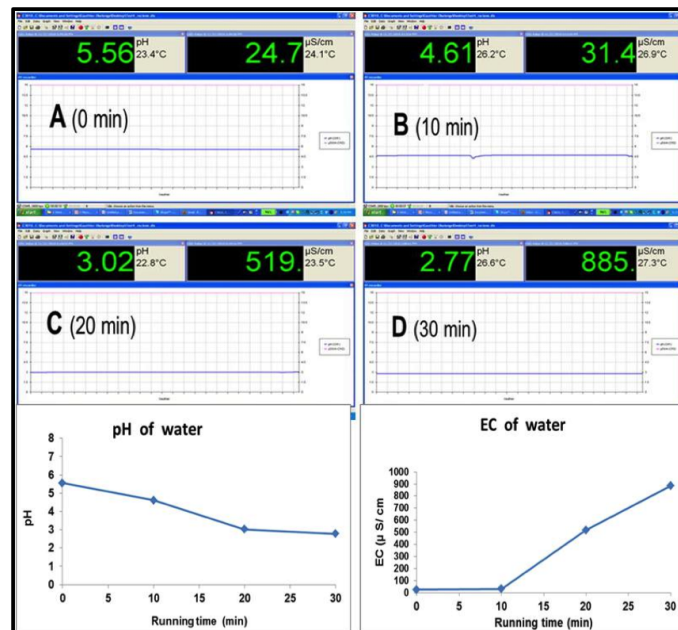


Figure 4.10: Dependence of the pH and conductivity on running time

It was observed (Figure 4.10) that the pH decreased from 5.56 to 2.77 with an increase in running time. The conductivity also increased considerably from 24.7×10^{-6} to 885×10^{-6} S/cm. This can be explained by the fact that the water splitting produces more ions, which increases the conductivity of the solution on one hand, and on the other hand, the discharge of air through the corona produces ozone and nitrogen is transformed to NO in water. (Locke et al., 1995).

In order to investigate the effect of UV irradiation on MB degradation, without active species produced, when the air flows in the system, Figure 4.11(A) shows UV only in the left beaker and UV with bubbled air in the righthand image. To investigate the degradation of MB under UV irradiation from the OK-3 system, with and without airflow, the following conditions were used: 10 ppm MB, pH 6, 15 kV, 25 kHz. . It is observed that a slight change occurred using just UV, whereas a total colour change occurred in the right beaker when the air was flowed, as shown in Figure 4.11(A1) and 4.12 (B1).

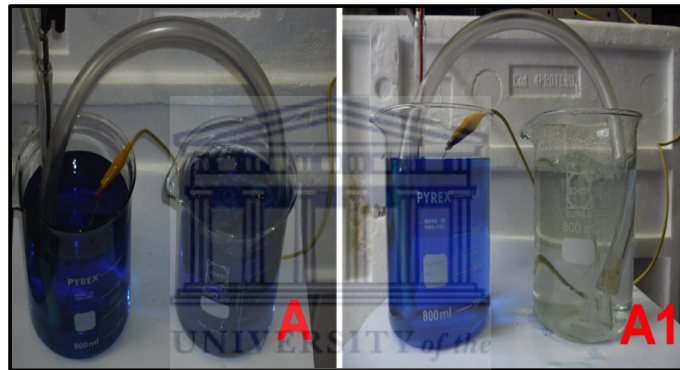


Figure 4.11: (A1) The decoloration of MB after 48 min using the dissolved ozone from OK-3 and (A) no significant color change without ozone



Figure 4.12: (B1) The decoloration of MB after 30 min, using the dissolved ozone from OK-3, UV and other species (B)



Figure 4.13: The degradation of MB after different running times (0, 10, 20 and 30 minutes)

The degradation of MB was then tested at different running times (0, 10, 20 and 30 minutes) as shown in Figure 4.13. A total volume of 5 l of dye solution was circulated through the reactor, using a peristaltic pump at a flow rate of 100 ml/min. The initial concentration of Methylene blue was 10 mg/l. The conductivity of the solution was adjusted to 5 mS/cm by adding KCl. The initial pH values of the solution were adjusted to 3.5, 7.5 and 10.3 by adding HCl or KOH. Air was supplied at a flowrate of 2 l/min. The concentration of the Methylene blue solution was quantitatively analysed by spectrophotometric methods.

The concentration of the Methylene blue solution was monitored using a Vis-723G visible spectrophotometer at a wavelength of 665 nm, and the functional groups of the products were determined with a V33 Fourier transform infrared spectrometer (FT-IR). The complete de-mineralization of Methylene blue was determined by using liquid chromatography mass spectrometry (LC-MS), and nuclear magnetic resonance (NMR).

4.2.3.4 Results and discussions

Figure 4.14 shows the changes of the spectrum of Methylene blue solution after 0, 10, 20 and 30 min discharge plasma treatment, where the applied voltage and the initial pH were 12 kV and 6, respectively. Control experiments, without power, showed no decrease in dye concentration. The maximum absorption of Methylene blue in the aqueous solution is 665 nm. The change of the concentration of Methylene blue during plasma treatment could thus be determined by measuring the variation of its absorbance at 665 nm. However, the disappearance of the peak at 665 nm could simply be an indication that the system only decolorizes the Methylene blue. To investigate that, the samples were also examined with FT-IR, as shown in Figure 4.15.

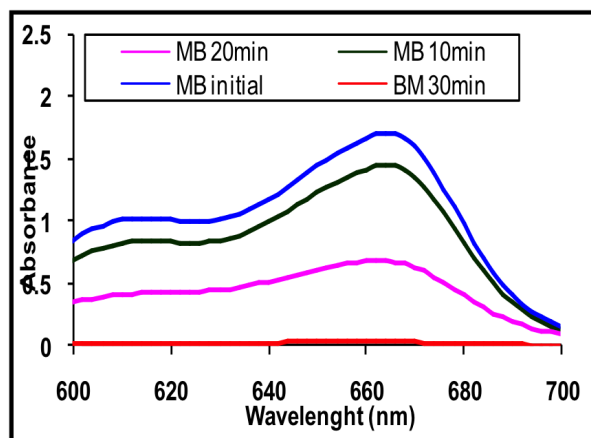


Figure 4.14: The measured change of the spectrum of Methylene blue solution after 0, 10, 20 and 30 min of discharge plasma treatment (applied voltage = 12 kV, treatment time = 30 min)

The typical IR spectra of Methylene blue are shown in Figure 4.15, both before and after 10, 20 and 30 min of treatment. The decrease in the intensity of certain peaks demonstrate that the dye was degraded to carbon dioxide and water.

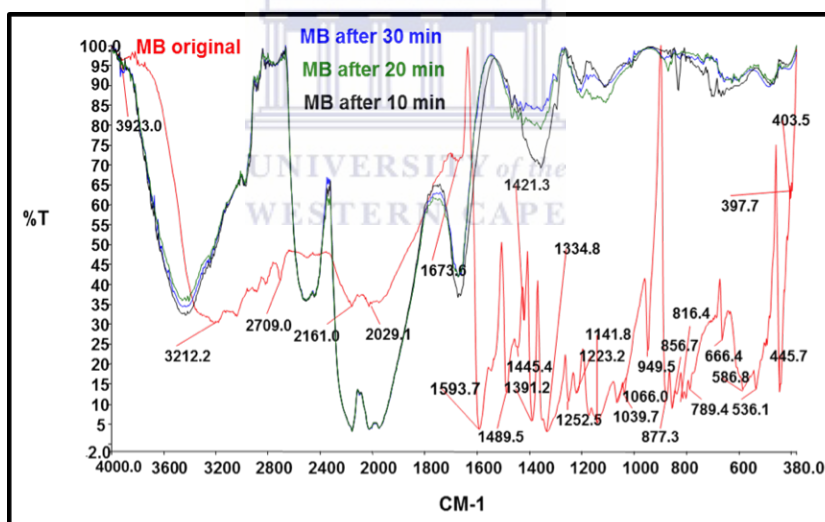


Figure 4.15: Changes in the FT-IR peak spectra during degradation of MB at different running time

The IR spectrum exhibits one aromatic ring C-H stretching vibration peak at 3144 cm^{-1} and three aromatic ring C=C stretching vibration peaks at 1640 cm^{-1} , 1493 cm^{-1} , and 1530 cm^{-1} , respectively. After treating the Methylene blue in a continuous mode, these peaks decreased in intensity to very low levels, which indicates that the aromatic ring of the dye molecule was successfully degraded. In addition, the peaks at 1610 cm^{-1} and 1331 cm^{-1} are due to the -N=C- bond and the C-N stretching band of dye molecules, respectively. The disappearance of these two peaks is associated with destruction of the [3, 7-bis (Dimethylamino)-phenothiazin-5-ium chloride] (Sugiarto et al., 2000). Although the intensity of the critical peaks was significantly reduced, LC-MS measurement results, shown in

Figures 4.16, 4.17, 4.18 and 4.19, and NMR measurement results, shown in Figure 4.20, further confirmed that the process did not produce residual pollutants.

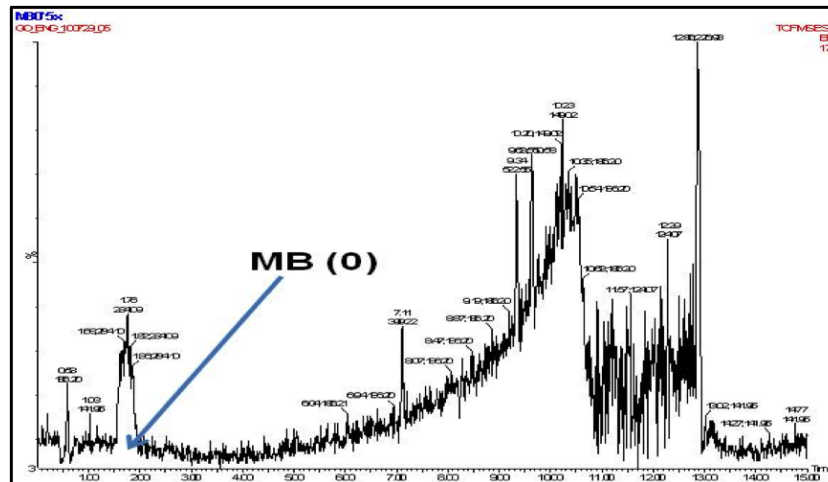


Figure 4.16: Presentation of the mass extraction of the initial MB solution when the power was off

From Figure 4.16, the peak at $m/z=284$ corresponds to the M^+ molecular ion of Methylene blue. The mass integration peak of MB, which is observed in Figure 4.17, disappeared after 30 min of treatment, as shown in Figure 4.19. This correlates strongly with the FTIR data, demonstrating that the target compound was de-mineralized by the process. Further confirmation was seen with the NMR results, shown in Figure 4.20 below.

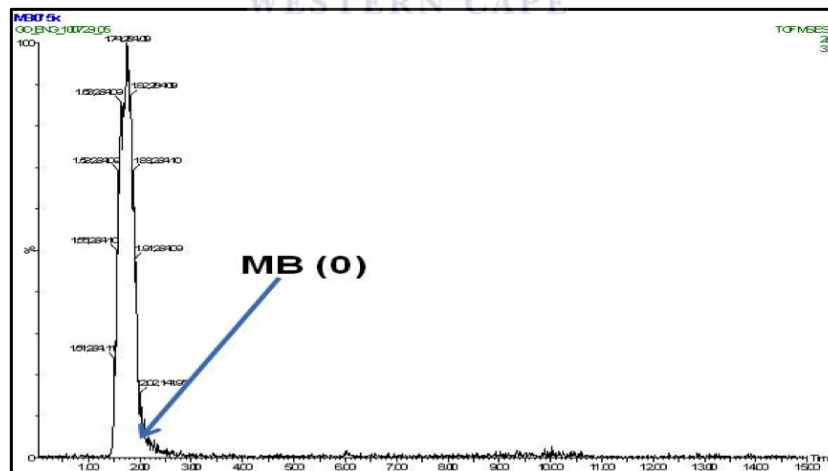


Figure 4.17: Presentation of the peak area integration of the initial MB solution when the power was off

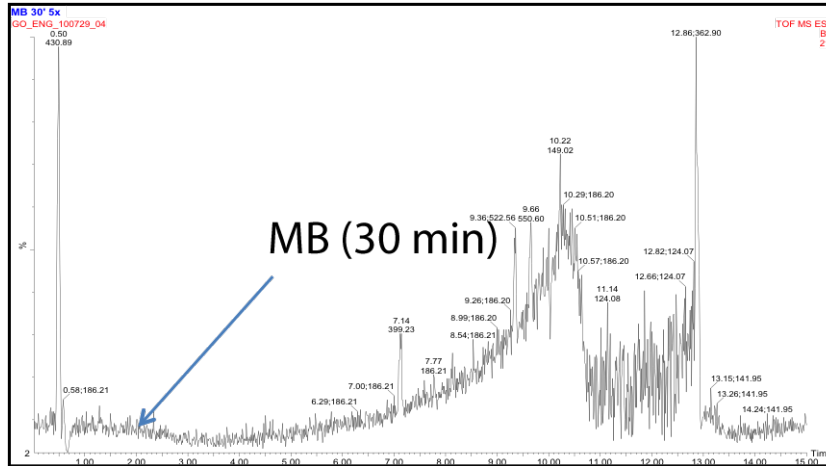


Figure 4.18: The shifting peak of mass extraction of MB after 30 min running time

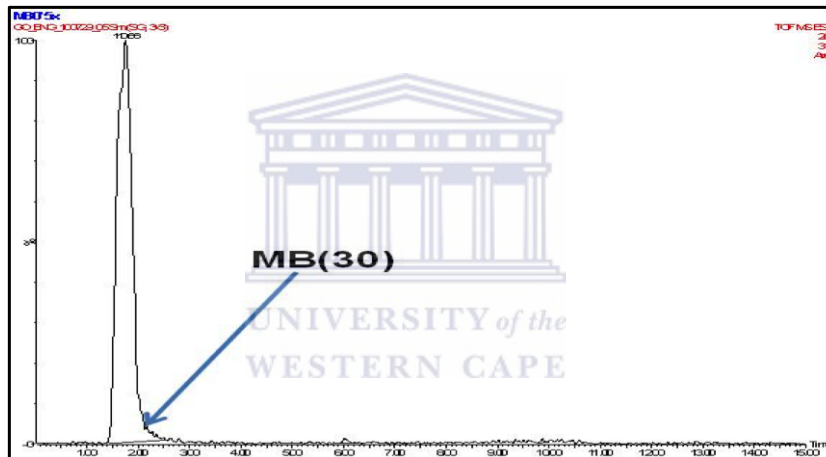


Figure 4.19: The shifting peak area integration of MB after 30 min running time

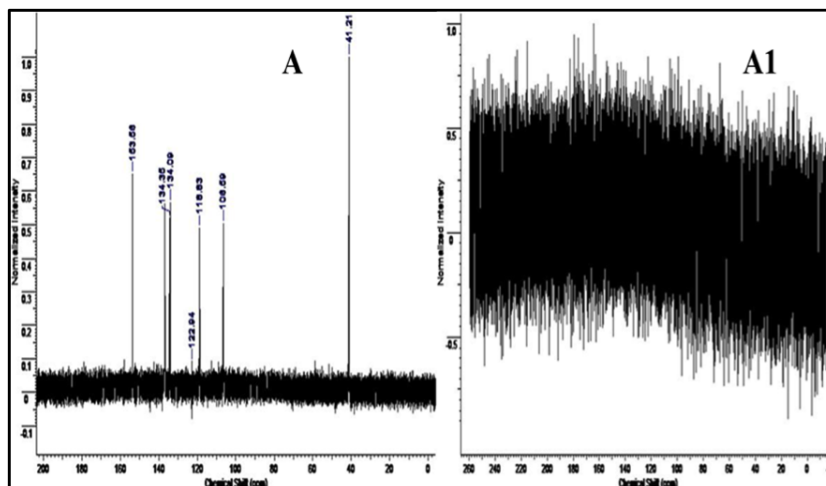


Figure 4.20: The measured change in carbon NMR of MB (A) before and (A1) after 30 min

As reported in some papers (Locke et al, 1995), corona discharge plasma in water can lead to the formation of active species such as $\cdot\text{OH}$, $\cdot\text{O}$, H_2O_2 , etc. Due to the high oxidation potential, especially for hydroxyl radicals, these species directly attack the organic pollutants. This suggests that the degradation of Methylene blue occurred due to the breakup of the bonds by various radicals in the corona discharge plasma region, as the NMR result confirms the non-existence of carbon peaks after 30 min running time.

4.2.3.5 Comparative results between solar disinfection (SODIS) and the OK-3 reactor using river water

In order to study the effectiveness of the designed reactor OK-3, a comparative experiment on river water disinfection was done using solar water disinfection (the SODIS method), which is a simple procedure to disinfect drinking water (see Figure 4.21). As mentioned in Section 3.2.6.1 and Figure 3.8, contaminated water is filled in a transparent pet-bottle or glass bottle and exposed to the sun for 6 hours. During this time, the UV-radiation of the sun kills diarrhoea generating pathogens. The SODIS method helps to prevent diarrhoea and thereby is saving the lives of people. The comparative results are shown in Figure 4.22.



Figure 4.21: A photo of the solar disinfection model (SODIS)

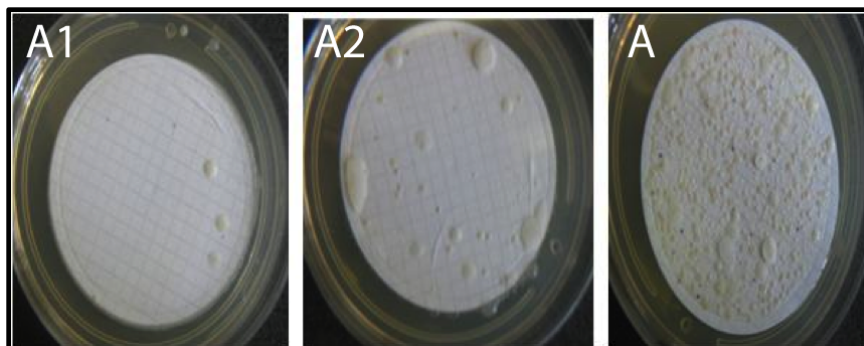


Figure 4.22: The inactivation of microbes from contaminated river water: (A) Control plate with initial concentration, (A1) the prototype OK-3 and (A2) the solar disinfection method (SODIS)

The standard plate count attempts to provide a standardized means of determining the density of bacteria in water, as described in Section 3.2.6.1. Bacteria occur singly or in pairs, chains, clusters or packets, and no single method, growth medium, or set of physical conditions can satisfy the physiological requirements of all bacteria in a water sample. However, the heterotrophic plate count is a good measure of water treatment plant efficiency, after growth in agar plates, and the general bacterial composition of source water. It was observed with the naked eye, using a magnifying glass or bacteria colony counter, that the inactivation results of microbes from contaminated river water of the sample analysed for (A1) the prototype OK-3, presented a significantly better bacteria killing efficiency than (A2) the solar disinfection method, when compared with (A) the control plate.

4.2.3.6 Summary conclusion

An electrohydraulic system was designed, assembled and tested as a water treatment rig prototype (OK-3). The system successfully mineralized a model dye, Methylene blue, within 30 minutes. Analyses with FT-IR, LC-MS and ^{13}C NMR confirmed that no residual organic pollutants were present after 30 minutes. The design does not suffer from electrode corrosion, and uses a low power system for the treatment of water, which may be integrated with solar panels or other decentralised power options, for application in rural areas.

The next chapter discusses the results obtained during the search for the optimum synthesis conditions of TiO_2 nanofibres, using electrospinning and a sol-gel solution. The study aimed at the incorporation of the TiO_2 nanofibres in the prototype (OK-3) in order to promote a cocktail of active species for water treatment, without adding chemicals.

Chapter 5

Results of synthetic TiO₂ nanofibres and its degradation efficiency

This chapter presents the characteristic results of the synthesis of TiO₂ nanoparticles, obtained by the electro spinning method (on a stainless steel grid). Synthesized TiO₂ nanofibres were compared to commercially available powder TiO₂ P-25 with regard to their efficiency as photocatalyst in the designed electrohydraulic discharge reactor (OK-3). Different characterization techniques, such as XRD, BET, FTIR, SEM, SAED, HRTEM and EDS were used to probe the properties that are important when determining the characteristics of the TiO₂ nanoparticles. Secondly, the results of studies conducted by the incorporation of the new nanocatalyst, the TiO₂ nanoparticles, in the reactor (see Chapter 3, Section 3.2.13) are compared with Degussa P-25 as baseline. Thirdly, the active species, such as OH radicals, ozone and hydrogen peroxide, that are responsible for the degradation of organics and inactivation of microorganisms in water, are identified.

5.1 Comparison between TiO₂ nanofibres and commercial TiO₂ nanoparticles (Degussa P-25)

In this section the characterization of commercial TiO₂ Degussa P-25, and synthesized TiO₂ nanofibres (NF), using XRD, FTIR, SEM and BET, are discussed. Structural changes and phase formation, using XRD and FTIR, are presented first. The morphology of the material, using HRSEM, is then presented, followed by the surface area and porosity of the materials, using N₂ BET. Morphological studies of all the samples were performed using Scanning Electron Microscopy (SEM, Philips XL30), as well as High Resolution Transmission Electron Microscopy (HR-TEM) and Selected Area Electron Diffraction (SAED) (see Chapter 3, Section 3.3). The specific surface area of the TiO₂ nanofibres was determined using the Brunauer-Emmett-Teller (BET) method (Micrometrics Gemini). The results are presented in the figures and tables below.

5.1.1 Structural changes and phase formation of TiO₂ nanofibres and baseline material by XRD

XRD spectra of all the samples were obtained according to the procedure described in Chapter 3, Section 3.3.3. The XRD experiments were performed on the Advance D8 from Bruker AXS, at high 2θ angles, to assess the mineral phases present in the baseline materials, and to assess whether the TiO₂ nanofibres had retained their structure after carbonisation at 600°C. Figure 5.1 shows the measured XRD pattern of the commercial TiO₂ sample, as baseline.

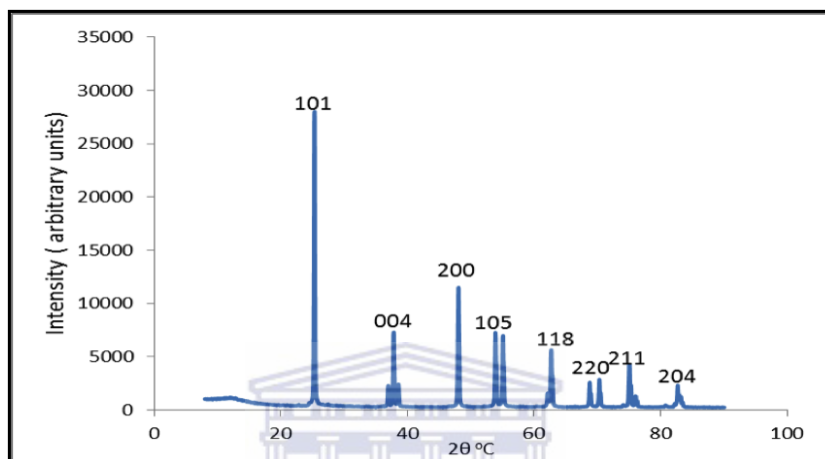


Figure 5.1: XRD phase identification of commercial TiO₂ as baseline material

The diffraction patterns of commercial TiO₂ powder (Figure 5.1) correspond to anatase TiO₂. The strongest diffraction peaks at $2\theta=25.3^\circ$ can be well indexed as the (101) reflection of anatase, and the other peaks at $2\theta=37.75^\circ$, 48° , 54° and 63.7° correspond to the (004), (200), (105) and (118) reflections of anatase (An et al., 2007). All the peaks observed were in good agreement with the standard anatase spectrum (Wang et al., 2008). Further comparison of XRD results obtained for the TiO₂ nanofibres calcined at 600°C, is shown in Figure 5.2.

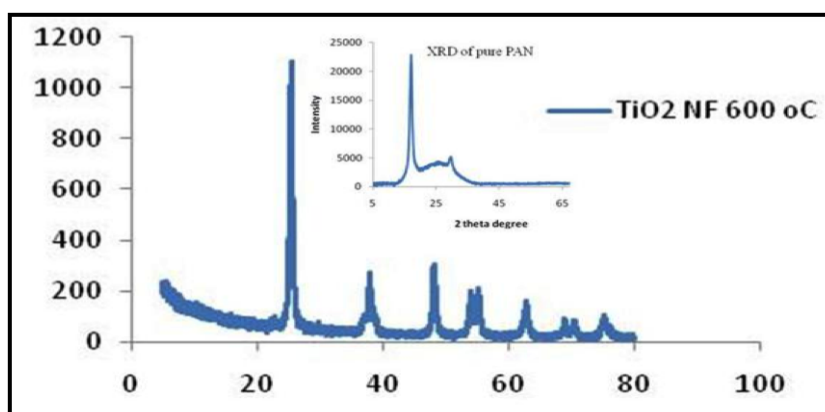


Figure 5.2: XRD analysis of pure PAN and TiO₂/CNF catalysts synthesized by the electrospinning method and carbonised at 600°C in N₂

It can be seen from the XRD pattern in Figure 5.2 that the expected TiO₂ peaks were identified, indicating that the composite materials prepared are crystalline, and the expected metal phases are present on the surface of the CNF substrate, showing the successful formation of the TiO₂/CNF composite. XRD results of the prepared sample revealed several peaks that are characteristic of anatase and rutile, which are the crystalline form of TiO₂. The anatase peaks were identified at 25.2, 37.8, 53.9° 2 θ , and rutile peaks were identified at 65.45° 2 θ . However, the most crystalline composite sample was TiO₂/CNF prepared at 600°C. The observed trends were also also evident from the BET data, when compare with the P-25 Degussa in Table 5.1.

5.1.2 Surface area and pore size distribution of the synthetic and baseline material

The surface area, pore volume distribution and particle sizes of the synthetic nanomaterial and baseline material were studied by N₂BET, using the Micrometrics Accelerated SA and Porosimetry (ASAP) 2010 system, as described in Chapter 3, Section 3.3.6. The N₂BET surface areas and micropore area of commercial TiO₂ and synthesized TiO₂ nanofibres, using the electrospinning method, are listed in Table 5.1.

Table 5.1: BET surface area and micropore area of synthetic TiO₂ nanofibres and commercial TiO₂

Samples	Particle size (nm)	Surface area (m ² /g)
TiO ₂ CNF / 600°C	5.75	58.94
P-25(Degussa)	21	50.7

The BET surface area of commercial TiO₂ has a specific surface area of 50 m²/g, and a particle size of 21 nm (Iran et al., 2011). On the other hand, the synthesized TiO₂ nanofibres have a specific surface area of 58.94 (larger than commercial TiO₂) and a particle size of 5.75 nm (smaller than commercial powdered TiO₂), which leads to higher activity. These results corroborate work reported by Slimen et al. (Slimen et al., 2011) for the degradation of Methylene blue. It is expected that an increase in the surface area will lead to an increase in the amount of TiO₂ that can be supported on the substrate, which may be beneficial for enhancing the photocatalytic activity. The N₂ adsorption-desorption isotherm of the CNF/TiO₂ sample shown in Figure 5.3 was identified as the Type IV isotherm, with a hysteresis loop due to capillary condensation, which indicates that the TiO₂/CNF nanocomposite catalysts are mesoporous.

Brunauer-Emmett-Teller (BET) adsorption analysis of the nanocomposite materials (Figure 5.3) shows the incremental volume adsorbed at each pore diameter for a selected sample of CNF/TiO₂, carbonized at 600°C, as compared with the commercial TiO₂ P-25 Degussa shown in Figure 5.4.

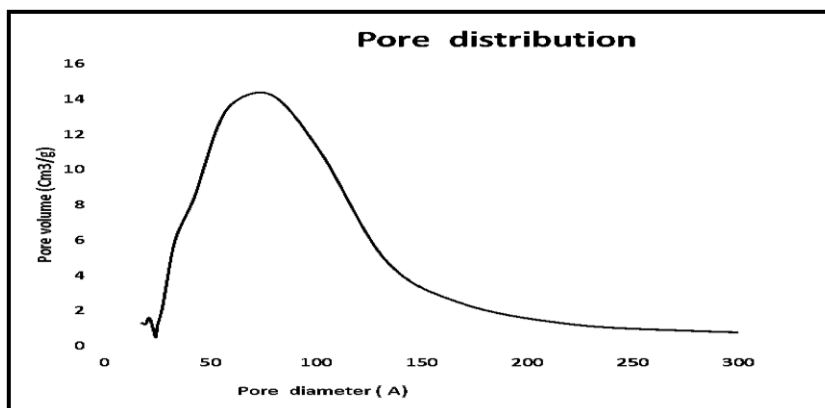


Figure 5.3: CNF pore-size distributions of TiO₂ CNF at 600°C

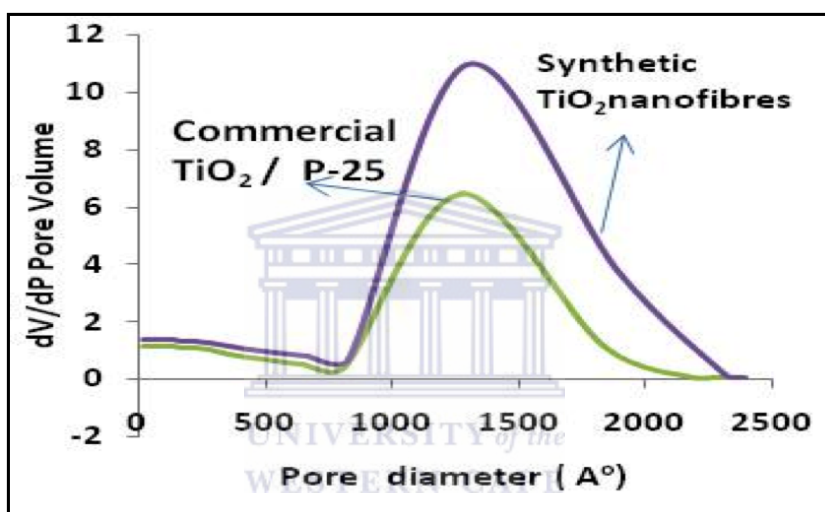


Figure 5.4: The pore size distribution of commercial TiO₂ particles and TiO₂ CNF at 600°C

The N₂ adsorption and desorption isotherm of the synthetic TiO₂ nanofibres and that of the commercial powdered TiO₂ P-25 is presented in Figure 5.5.

Figure 5.5 shows the Brunnauer-Emmett-Teller (N₂BET) analysis of the nitrogen sorption isotherms of commercial TiO₂ particles. The TiO₂ material isotherm belongs to the isotherms classified as Type IV with a hysteresis loop associated with capillary condensation of gases within the mesopores (2-50 nm). This hysteresis loop typically belongs to the H₂ type, which is consistent with pores that have narrow necks and wider bodies (Ryn et al., 1999).

The comparison results in Figure 5.5 shows H₂-like hysteresis loops, pointing towards pores that are slit-like. These isotherms show high absorption at high relative pressures, approaching 1. This is in accordance with a diverse mesopore size distribution associated with intra- and inter-aggregation of nanocrystals with non-uniform size (Sing et al., 1985). This indicates that the synthetic TiO₂ nanofibre materials have large mesoporous and macro pores on the external surface area of the fibres. This is an indication that the synthetic nanomaterials were well prepared, as is also evident of the structural functional group in the next section.

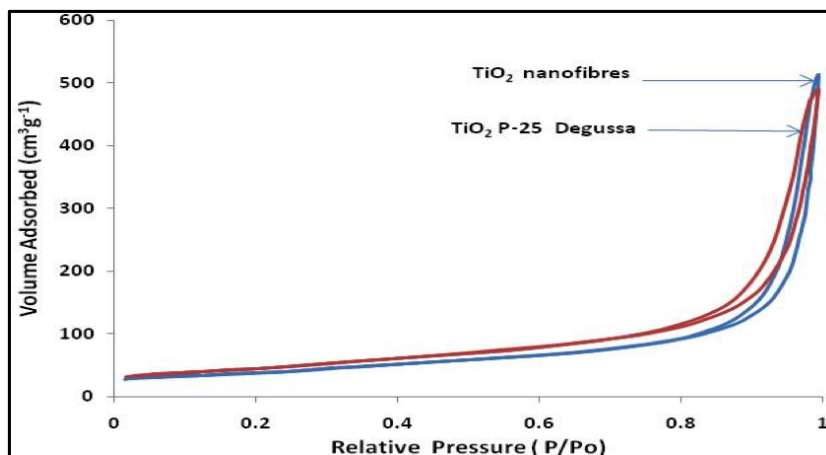


Figure 5.5: N₂ adsorption-desorption isotherm of commercial TiO₂ particles compared to synthetic TiO₂ nanofibres, using N₂BET

5.1.3 Structural changes and functionalization of TiO₂ nanofibres

The FTIR spectral data was recorded on Perkin-Elmer equipment, as described in Section 3.3.2, and is presented in Figure 5.6, which presents the spectra of unstabilized TiO₂ and stabilized TiO₂ nanofibres.

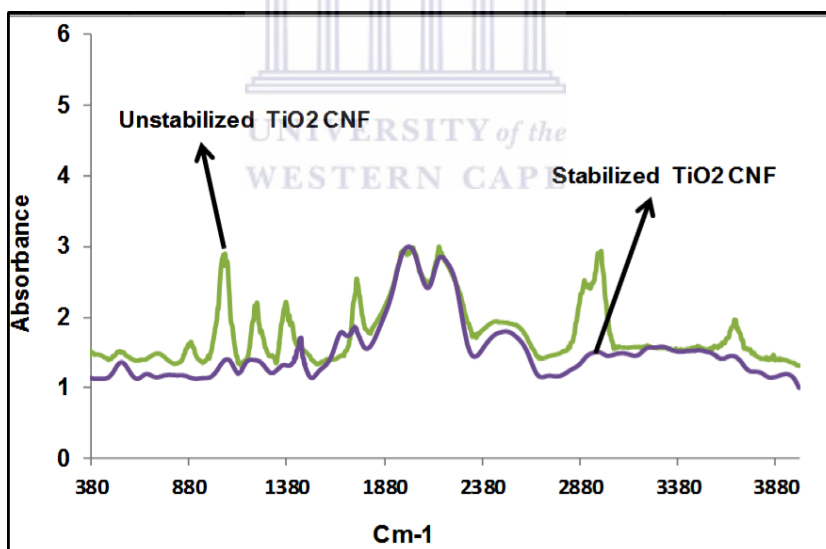


Figure 5.6: The FTIR spectra of unstabilized TiO₂ and stabilized TiO₂ nanofibres

In the FTIR spectrum of unstabilized PAN/TiO₂, the peak at 1642 cm⁻¹ is due to the -C = C- bond. The peaks at 1171 cm⁻¹ and 1734 cm⁻¹ are probably due to C=O of the residual DMF, since these peaks disappear in the spectrum of the stabilized PAN. The results are similar to FT-IR of TiO₂ nanofibres as reported by (Deng et al., 2003) and Figure 5.7 highlights the trend.

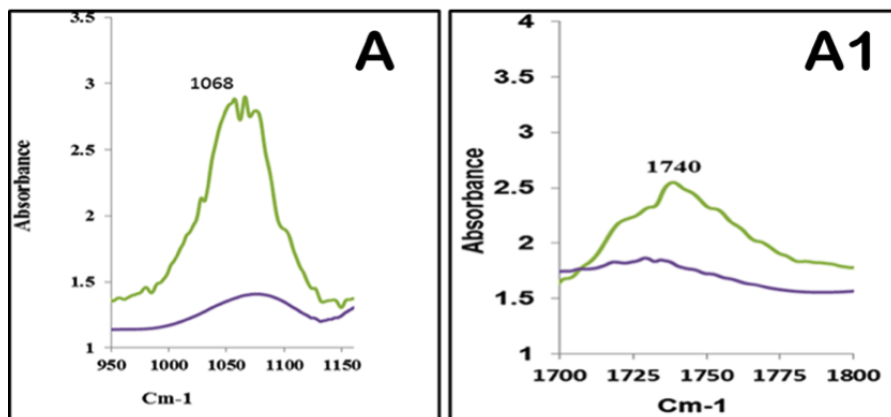


Figure 5.7: The specific FTIR peak area of (A) unstabilized TiO₂ and (A1) stabilized TiO₂ nanofibres

A stretching vibration band at 1740 cm⁻¹, that was observed in the peak area between 1660-1745 cm⁻¹, confirms the presence of the carbonyl group C=O from PAN copolymer, which was higher initially and almost disappeared after stabilization. The absorption intensity peak at 1740 cm⁻¹ is attributed to symmetric stretching of carbonyl groups from PAN, which decreases significantly after heating the synthesis material up to 600°C in air, followed by N₂. The decrease of functional groups of carbonyl and carboxylic acid can increase the number of active sites and, therefore, be beneficial for the photo catalysis process (Alvies et al., 2009).

5.1.4 High Resolution Scanning Electron Microscopy (HRSEM)

Morphological analysis is a useful characterization technique that is highly valued during the investigation of crystalline processes of nanofibres, since it can be used to examine the quality of the synthesis product. This section presents the SEM images and their SAED of the synthetic nanofibres that were electrospun and carbonized at 600°C in nitrogen. The HRSEM was conducted on a Hitachi X 650 Scanning Electron Microscope according to the procedure described in Section 3.3.4. Figure 5.8 shows HRSEM images of (a) the synthetic TiO₂ nanofibers and (b) commercial TiO₂.

Commercial TiO₂ (Figure 5.8b) shows a spherical and globular shape and this is indicative of particulate TiO₂ materials. TiO₂ nanofibres (Figure 5.8a) show the immobilised crystalline carbon nanoparticles supported on a stainless steel grid, possessing crystallites of a wide variety of length ranges, with lengths ranging from 2-30 nm to several tens of micrometres. As mentioned by Vasilev et al. (Vassilev and Vassileva 2007), SEM analysis falls in the category of techniques that are highly recommended and mostly used for chemical and physical characterization of nanomaterials. Figure 5.9 presents the SEM images that were taken from the synthetic nanofibre sample before and after the carbonization process at 600°C for 3 hours at different magnification levels.

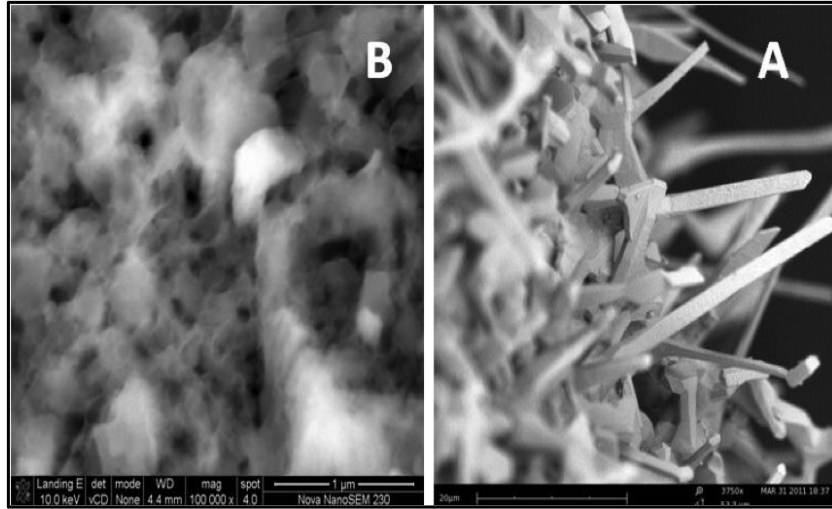


Figure 5.8: HRSEM images of (b) commercial TiO_2 (a) TiO_2 nanofibres stabilized at 600°C in nitrogen

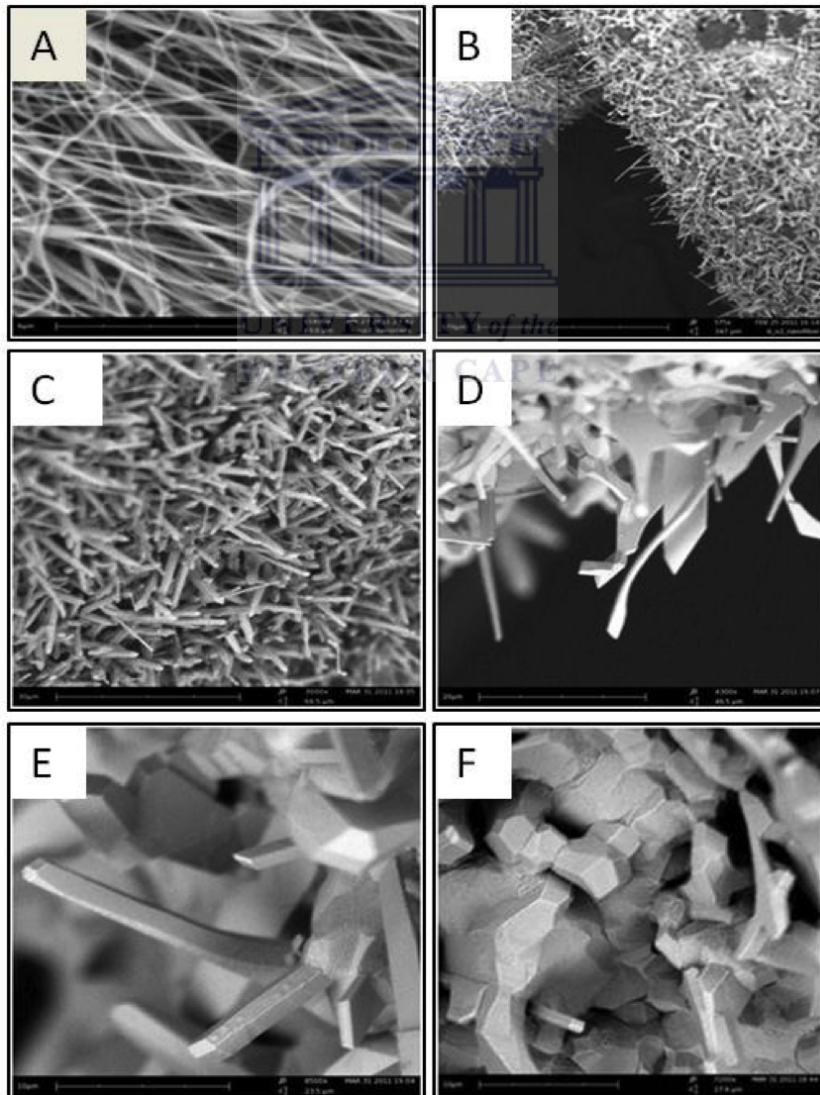


Figure 5.9: SEM images of electrospun TiO_2 nanofibres: (a) As-electrospun TiO_2 fibre; (b) After carbonization at 600°C in nitrogen for 3 hours; (c) magnification $5000\times$ $30\ \mu\text{m}$ (d) magnification $4300\times$ $20\ \mu\text{m}$ (e) magnification $8500\times$ $10\ \mu\text{m}$ after 10 min of sonication (f) magnification $7200\times$ $10\ \mu\text{m}$ after 10 min of sonication

After carbonization, as shown in the Figure 5.9, the SEM micrographs revealed a distinct change in the morphology of the samples. At low magnification, the characteristic long fibrous mat structure, typically seen with nanofibres, changed to a branch-like layer, with short and randomly orientated crystals. At higher magnification, these branches were decorated with needle-like structures. The reasons for this transformation are unclear, since the literature shows the carbonization of similar structures simply changed the diameter of the nanofibers, and not the overall morphology of the sample (Kim and Lim 2008). However, the reference used TiO₂ powders, whereas this method used a sol-gel of Titania that could have introduced surface areas that may have affected the carbonisation of the sample. The following SEM images in Figure 5.10 show the non-woven on grid supporting material, before and after calcination in nitrogen at 600°C in the furnace (see Section 3.2.11 and Figure 3.13).

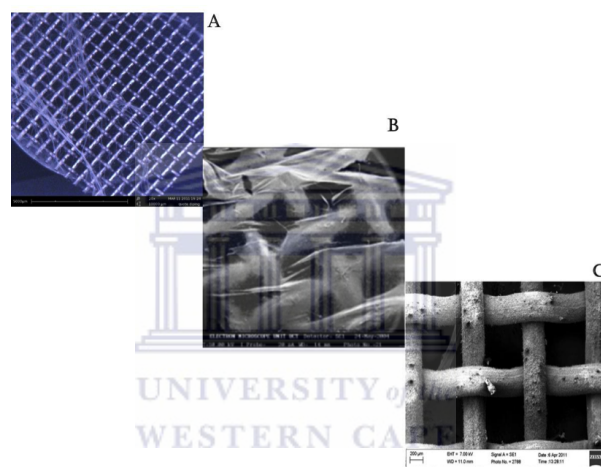


Figure 5.10: The non-woven on grid supporting material before (A and B) and after calcination (C)

As indicated in the problem statement, there is a need for a flexible supporting material to avoid post-treatment separation of nanoparticles from treated water. The immobilization of nanoparticles with a new process is the best way to overcome the limitation of photocatalytic processes for water treatment.

The SAED measurement results of the synthetic, new fashion TiO₂ nanofibres, are shown in the SEM results in Figure 5.11, after sonication for 15 min. The use of sonication on the TiO₂ nanofibres demonstrate clearly that the immobilization of nanoparticles on supporting grid was successfully deposited. The SEM images were taken from the sample that was prepared using the procedures discussed in Sections 3.2.8 to 3.2.11.

The morphology observed in Figures 5.9 and 5.11 of the TiO₂ nanofibres was found to be, after a thorough literature search, new nanomaterials. There was no published evidence that has reported the synthesis of this unique morphology of TiO₂ nanofibres grown from a sol-gel method, using an electrospinning process.

Figure 5.12 shows SEM images that were taken from a sample that was prepared with the same procedures discussed in Sections 3.2.8 to 3.2.11. The only difference was that no

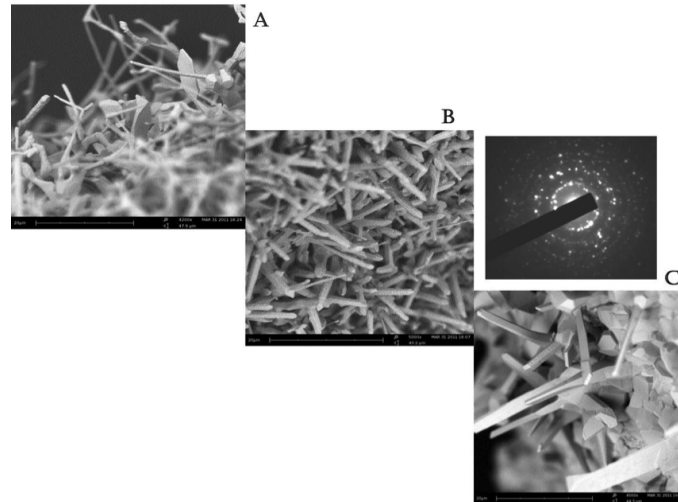


Figure 5.11: SEM images of new fashion electrospun TiO₂ nanofibres (A, B and C) after hydrolysis, at different magnifications, carbonized at 600°C in nitrogen, and SAED of the same sample.

hydrolysis was used and the fibres were thus dry at room temperature before carbonization was done in the furnace. This was done to investigate the changes in the morphology of dry fibres, when compared with the wet fibres.

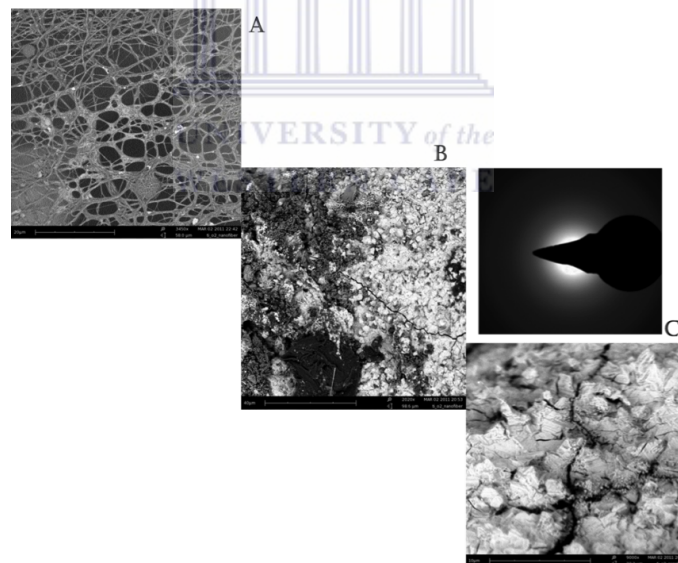


Figure 5.12: SEM images of electrospun TiO₂ nanofibre (A) TiO₂ fibres on the grid (B) Same sample without hydrolyzed before carbonization at 600°C in nitrogen. (C) Same sample magnified at 1 μm and SAED image of the same sample.

The images in Figure 5.12 show that the hydrolysis step was necessary, as without it the TiO₂ crystals were not uniform, nor in the nanometer range.

The results in Figure 5.13 show the SEM images of TiO₂ obtained from a combination of techniques, such as electrospinning and sputtering of TiO₂ P-25 on top of wet electrospun fibres, as indicated in Section 3.2.3. The idea behind this experiment was to have more

nanoparticles on the surface of nanofibres, thus enhancing the photodegradation of dye. It was reported in the literature (Sakhtievel et al., 2004) that more nanoparticles on the surface of supporting material will lead to more photodegradation of pollutants. This was the reason for the experiment, using the sputtering of TiO₂ P-25 on wet electrospun fibres, by reducing the distance between the tips of syringe and the collecting vase, as indicated in Section 3.2.13 and Figure 5.13.

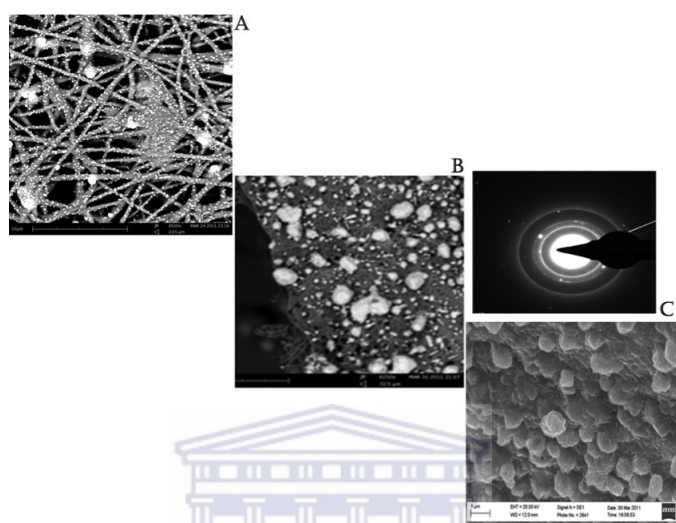


Figure 5.13: SEM images of a sample prepared as in Section 3.2.13 with a combination of sputtering and electrospinning techniques. (A) As wet electrospun fibres; (B) Magnified; (C) Calcinated and its SAED image.

The powder TiO₂ sputtered onto the fibres appears to be randomly distributed throughout the sample as titanium dioxide deposits, and this was confirmed by surface area Energy Dispersive Spectroscopy (SAED) spot analysis. SAED spectra of the sample identified the crystallinity of the material. It was noticed that both the TiO₂ CNF obtained from the sputtering method (see Figure 5.13) and the one from the non-hydrolysed nanomaterial (see Figure 5.12) would be able to release particles in the treated water, after 10 min of sonication, turning it to a white colour. Therefore, the immobilization on grid and calcination after hydrolysis of the electrospun TiO₂ CNF (see Figure 5.11) was found to be an ideal nanomaterial to investigate, checking its characterization and performance on the photodegradation of pollutants.

The synthesis and immobilization of nanomaterials or porous materials have been of intense scientific and technological interest, because the presence of tailored micro-, meso- and macro pores at different scales have the potential of solving the well-known problems of diffusional constraints and mass transfer limitations, or recombination, that are often associated with the internal micropores in photocatalysis (Chen et al., 2009; Mao et al., 2007).

The formation of this hierarchical nanomaterial, using the electrospinning method, without requiring the use of additional ingredients or post-synthesis treatment, is advantageous compared to the complicated procedures that are reported in the literature, that are either

based on chemical or physical techniques, that are discussed in detail in a recent review by Yang et al. (2009).

The following characterization results are based on the newly synthesized nanomaterial. It is important to emphasize that no additional steps were added in the synthesis of the TiO₂ nanofibres, apart from the hydrolysis of the electrospun non-woven fibres, before carbonization, that was used during the immobilization step on the supporting material.

5.1.5 High Resolution Transmission Electron Microscopy (HRTEM)

In order to study nanoparticles in general, and catalysts in particular, transmission electron microscopy is a useful technique that can be used, in three different ways, as described below. Firstly, when the specimen is of substantial macroscopic size, so that electron beam penetration is impossible. Secondly, the direct observation of specimen morphology when the specimen is a powder or some other sort of material in a state of subdivision, which lies beyond the resolution of optical microscopy. Estimation of average metal particle size and particle size distribution in dispersed metal catalysts is an example of this application. Thirdly, the use of HRTEM lies in the observation and interpretation of contrast features, which occur within specimen images, extension contours, various sorts of phase contrast features and lattice images, which all can give information about specimen structure (Anderson et al., 1988).

HRTEM samples were prepared by dispersion of a spatula-tip of the catalyst of interest in a 5 ml methanol solution, followed by sonication of the suspension. One drop of the suspension was deposited, as discussed in Section 3.3.5, on carbon grids and allowed to dry for 15 minutes. Samples were mounted in a sample holder that was introduced into the shaft of the electron microscope. The following TEM images were taken from the prepared samples.

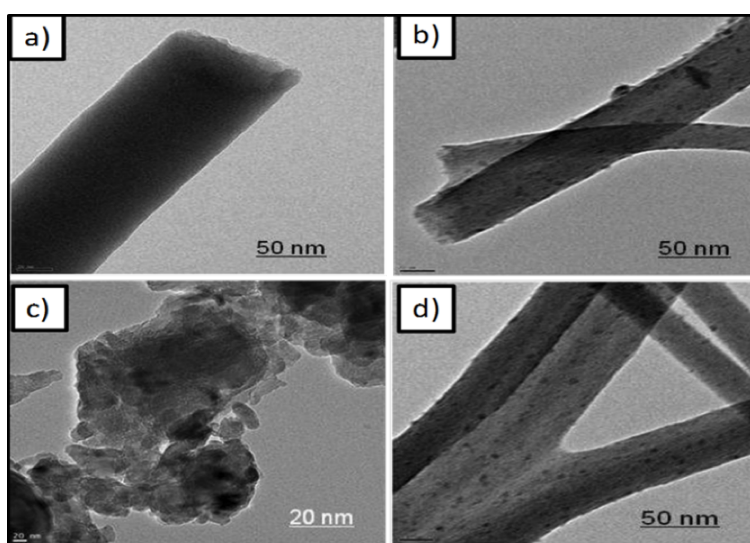


Figure 5.14: Selected HRTEM images of electrospun TiO₂ nanofibres at different magnifications.

HRTEM examination of the carbonized samples showed some interesting features. Some clearly observed examples are highlighted in Figure 5.14, such as filled nanofibres, (Figure 5.14(a)), partially hollow nanopipes (Figure 5.14(b) and (d)), Y-branched carbon nanostructures (Figure 5.14(d)), and titania agglomerates (Figure 5.14(c)).

From the HRTEM analyses, TiO₂ was identified on both the large agglomerates and on the individual nanofibres. In Figure 5.14(b) and (d) the dark spots decorating the carbon nanofibres were shown to contain Ti when EDS spot analyses were done, and SAED patterns did show ring-like structures and intense spots, characteristic of such materials. The SAED pattern of TiO₂/CNF carbonized at 600°C, obtained from the 20 nm HRTEM image, is shown in Figure 5.14 and the pattern obtained shows the crystalline nature of the composite. The mineral phases were confirmed, using the XRD pattern to distinguish whether TiO₂ is in the anatase or rutile phase.

The EDS analysis in Figure 5.15 show the presence of Ti, although it is not an accurate measure of the amount of each element, as it is not a bulk quantitative technique, but merely a method of ascertaining an element's presence. This is due to the large inconsistencies in analyses at the nanoscale. However, it should be noted that, from the SEM images, the sample TiO₂/CNF catalysts, carbonized at 600°C, showed the highest crystallinity (see XRD results in Figure 5.2), which seemed to be dominated by the anatase phase, which is the TiO₂ crystalline phase, as proved by the EDS analysis.

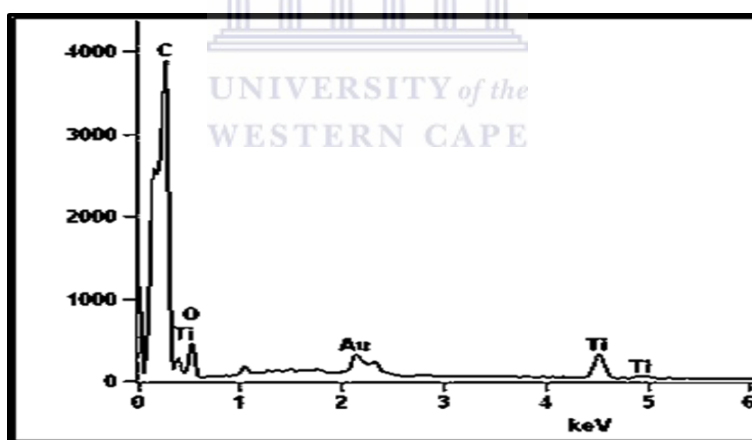


Figure 5.15: EDS pattern of the synthetic TiO₂/CNF.

In summary, the OK-3 prototype was tested with E.Coli solutions, and effectively disinfected the model solutions. The development of a composite supported TiO₂ nanostructured material was achieved. Titanium dioxide (TiO₂) nanofibres in the anatase structure were successfully prepared by an electrospinning technique, followed by calcination process. The morphologies, crystal structure, surface area and the photocatalytic activity of the resulting TiO₂ nanofibres were characterized by field emission scanning electron microscopy (FE-SEM), transmission electron microscopy (TEM), X-ray diffraction (XRD), nitrogen sorption and UV-Vis spectroscopy. The results revealed that the hydrolysed step before calcination had greatly influenced the morphologies of TiO₂ nanofibres.

The following sections describe the incorporation of the novel nanostructured supported TiO₂ material into the electrohydraulic discharge reactor, in order to make use of the UV radiation that accompanies the discharge during operation. This is envisaged to enhance the kill factor without the addition of chemicals. Also, the photocatalyst activity can be used without the problem of trying to separate the nanoparticles from the water, after decomposition of the organics, as the new composite material was shown to be very robust, containing the TiO₂ in a crystalline nanofilm upon the stainless steel mesh.

5.2 Integration of nanomaterials into the reactor

This section covers the results and discussion of the integration of the newly synthesized nanomaterials as catalyst into the OK-3 reactor. The electrohydraulic discharge reactor OK-3 produces UV radiation, which allows for the photodegradation activity of Methylene blue, as model pollutant dye. In this section the results of how the pH, dye concentration, the flow of gas in the system and different catalysts can influence the photo degradation, are given. The presence of killing factors, such as OH radicals, hydrogen peroxide and ozone in the water due to the photocatalysis activity, will be also presented.

5.2.1 Photocatalytic activity

Recently, TiO₂ has been used regularly in the photocatalyst field, due to its excellent photo activity, high stability and low cost (Kanjwal et al., 2010). In this study a simple reactor arrangement, utilizing a high voltage of 15 kV at a frequency of 30 kHz, and generating UV irradiation as described in Section 3.2.3.3, was used for the photocatalytic degradation of Methylene blue (MB). UV-Vis spectrometry was thereafter used to determine the extent of the MB dye degradation (see Section 3.2.8).

5.2.1.1 Effect of different catalysts on photocatalytic activity of MB without dissolved ozone

For comparison purposes the degradation of Methylene blue was done using nanofibres only, nanofibres TiO₂ (P-25) without carbonization and TiO₂ nanofibres, carbonized at 600°C. These experiments were conducted to understand whether TiO₂ nanofibres were the sole cause of the photocatalytic degradation, or whether the nanoparticles had the most noticeable effect, as shown in Figure 5.16 below. The experiments were performed in the OK-3 reactor in duplicate at room temperature, using a 50 mg/l initial concentration of Methylene blue, with a pH of 8, for 60 min, without flowing air through, to avoid the presence of dissolved ozone.

The results shown in Figure 5.16 demonstrate that the photodegradation of Methylene blue, using nanofibres only, did not show any change in MB concentration, whereas the run performed with commercial powdered TiO₂ P-25, sputtered upon the PAN electrospun fibres without carbonization, was very low. These materials were used as blank controls in trying to find out whether the new TiO₂ supported nanofibre catalyst was indeed the

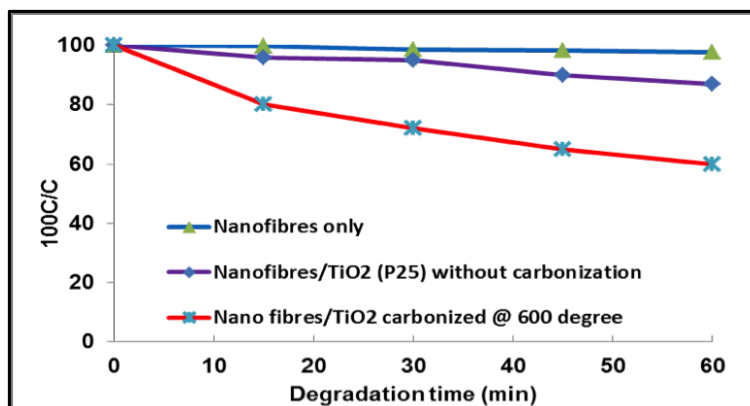


Figure 5.16: The photo degradation effect of different catalyst nanomaterials on Methylene blue (MB) (50 mg/l) over time, without air flowing through the system.

primary source of degradation. The recorded degradation of 40%, using the synthetic nano-material, was the highest, followed by P-25 without carbonization, resulting in a 16% degradation. These results show that nanofibres on their own and TiO₂ nanofibres (P-25) cannot be compared with the synthesized nanomaterials that were fabricated by an electrospinning method followed by calcination.

5.2.1.2 Effect of pH on photodegradation

Experiments were carried out in different pH conditions (3, 7 and 10). The results are given in Figure 5.17 and show that, as pH is increased, the efficiency of the catalyst for degrading MB dye also increased.

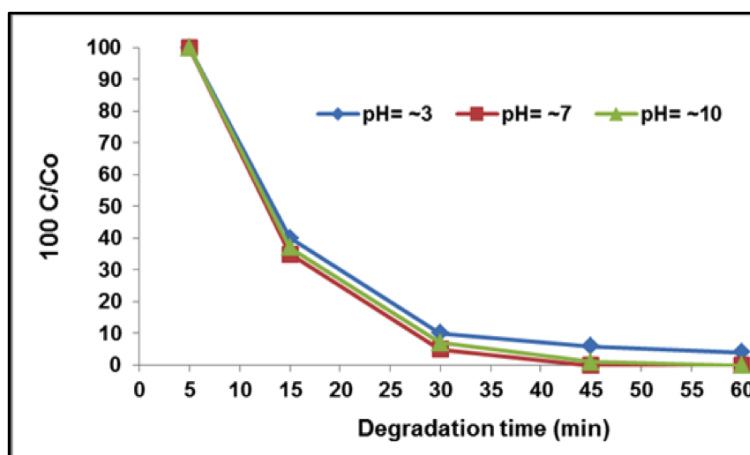


Figure 5.17: The effect of pH change on the degradation of MB (50 ppm MB, 15 kV, 30 kHz).

As shown in Figure 5.17, the degradation rate of MB increased with an increase in pH. However, the difference was not significant between pH values of 9 and 10. Consequently, pH=7 was selected as the optimum value. Optimum pH values for photocatalytic degradation, according to different studies, have been reported as between 1.5 and 11 (Akpan et al., 2006). Akpan stated that, for an alkaline condition, OH radicals are easier to be generated by

oxidizing the OH available on the TiO₂ surface, and therefore the efficiency is increased. On the other hand, under more alkaline conditions, there is a coulomb repulsion between the negatively charged surface of photocatalyst and the hydroxide anions. This could prevent OH radical formation and therefore inhibit the photo oxidation process.

5.2.1.3 Effect of MB concentration on photodegradation

Experiments were carried out in different MB concentrations (15, 30, 60 and 100 ppm respectively), with TiO₂ NF carbonized at 600°C and pH=7. The results are given in Figure 5.18 and show that, as the MB concentration was increased, the efficiency of the catalyst for degrading the MB decreased as well.

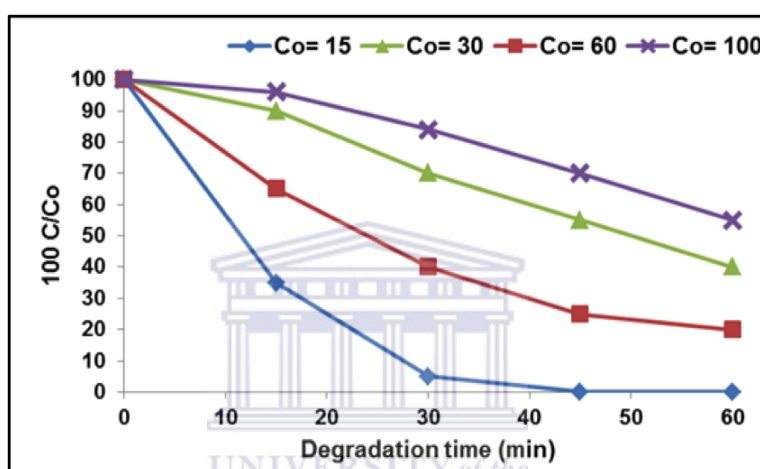


Figure 5.18: The effect of different MB concentrations on the photodegradation efficiency of catalysts (15 ppm MB, 20 kV, 25 kHz).

As is shown in Figure 5.18, with increasing MB concentration the efficiency of the catalyst for degrading dye decreased. When the dye concentration increases, the number of dye molecules absorbed on the catalyst surface increases too (Lee et al., 2003). Also, an increased concentration results in the reduction of UV radiation on the photocatalyst particles and also a reduction in production of OH[•], which, finally, causes reduced efficiency of dye removal (Toor et al., 2006).

5.2.1.4 The effect of air flowing through the system on the photodegradation of MB

Experiments were carried out using TiO₂ NF, carbonized at 600°C with pH=7, and UV with and without air flowing through. The results are given in Figure 5.19 and show that the air flowing through the discharge area that produces the ozone, contributes significantly to the degradation of MB.

As shown in Figure 5.19, the aeration rate helped to increase the efficiency of the process by the creation of UV, the formation of ozone through electrical discharge, more mixing through the diffuser and better reaction of the photocatalyst with the dye. In photocatalytic

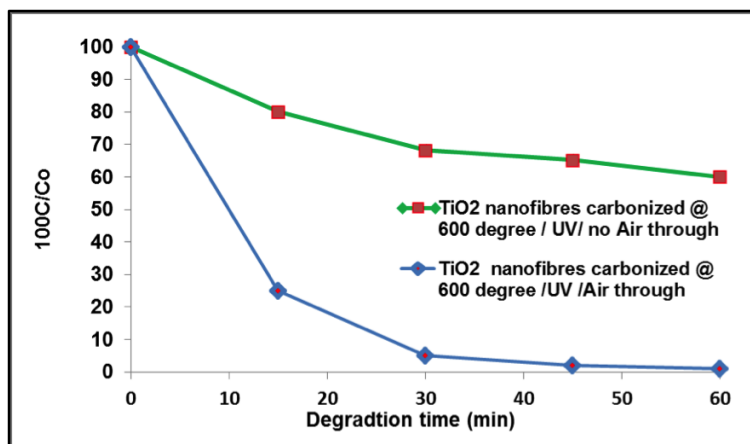


Figure 5.19: The effect of airflow on dye removal efficiency (TiO₂ NF at 600°C, MB concentration 50 ppm, pH=7, 20 kV and 25 kHz).

processes, electrons are produced by optical photons and the creation of holes on the photocatalyst surface. Concerning hydroxyl radical formation, it has been proved that the creation of electron holes and the production of free electrons are the main reasons for the formation of these active radicals. The available oxygen in the solution increases the production of hydroxyl radicals (Carp et al., 2004).

5.2.1.5 The effect of TiO₂ nanofibres on the photodegradation of Methylene blue

Experiments were carried out using the full OK-3 setup, with and without TiO₂ NF carbonized at 600°C and pH=7. The purpose of these experiments was to emphasize the benefit of the catalysts on the generation of radicals to enhance photo degradation of dyes beside ozone and hydrogen peroxide produced from OK-3. Results are given in Figure 5.20 and show that, apart from the ozone in the solution, there are other species generated by the supported photocatalyst that enhance the photo degradation of MB, reducing the running time from 30 to 15 minutes.

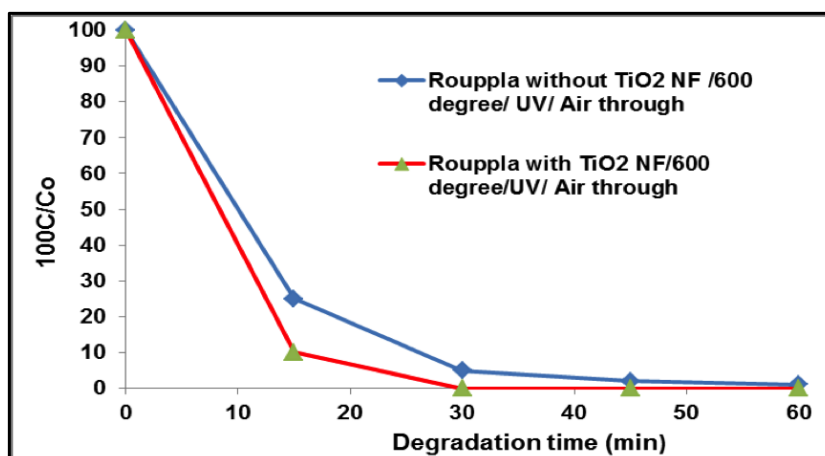


Figure 5.20: Catalytic effect of TiO₂ nanofibres, carbonized at 600°C, on MB degradation (20 kV, 25 kHz, MB concentration 50 ppm and pH=7).

Titanium dioxide composites were successfully prepared and immobilized on carbon nanofibres by electrospinning and annealing the PAN/TiO₂ composite. The nanoparticles were found to be fairly uniformly loaded on all the nanofibres. The photocatalytic activity was tested using a Methylene blue solution as a model pollutant, and it was found that CNF/TiO₂ exhibited a higher photoactivity than P-25/TiO₂ and PAN/TiO₂. The explanation is that, the smaller the particle (5.75 nm for the synthetic CNF), the higher the photocatalytic activity, compared to commercial P-25 (21 nm). The low photoactivity of PAN/TiO₂ is due to poor crystallinity. Calcination at high temperatures is a way of improving the crystallinity and this has a beneficial effect on the photoactivity of TiO₂. The photocatalytic properties of TiO₂ nanofibres, obtained by calcination at 600°C for 3 hours, exhibited the best photocatalytic activity. A novel and simple method to fabricate TiO₂ with high photocatalytic activity was presented. A novel and simple method to fabricate TiO₂ with high photocatalytic activity was presented.

The next section will focus on the detection of active species that target and destroy organic and microorganisms in polluted water.

5.3 Detection of active species

This section covers the results of the investigation and detection of OH radicals (using Electron Spin Resonance (ESR)), ozone (using the KI colorimetric method) and hydrogen peroxide (using the colorimetric method with titanyl ions) produced by electrohydraulic discharge. It is important to emphasize that the detection in these species were not quantitative, due to their short lifetime. The technology and methodologies were thus only used as proof of concept.

5.3.1 ESR spin-trapping experiments under UV light for OH radical detection

As indicated in Section 3.5.1, spin trap 5, 5-dimethyl-1-pyrroline N-oxide (DMPO) is widely used to provide evidence for the involvement of free radicals in many chemical and biological reactions (Noda et al., 1993). In particular, DMPO reacts with OH radicals and superoxide O₂ radicals, thus leading to the formation of the complexes DMPO-OH and DMPO-OOH, respectively. Both products are paramagnetic and can easily be detected by ESR (Fu et al., 2006). ESR spin trapping was used with DMPO to detect the formation of OH and O₂ radicals, under illumination of TiO₂ nanofibres with the UV light from the electrohydraulic reactor OK-3 (Rouppla). A summary of the results is given in Figure 5.21.

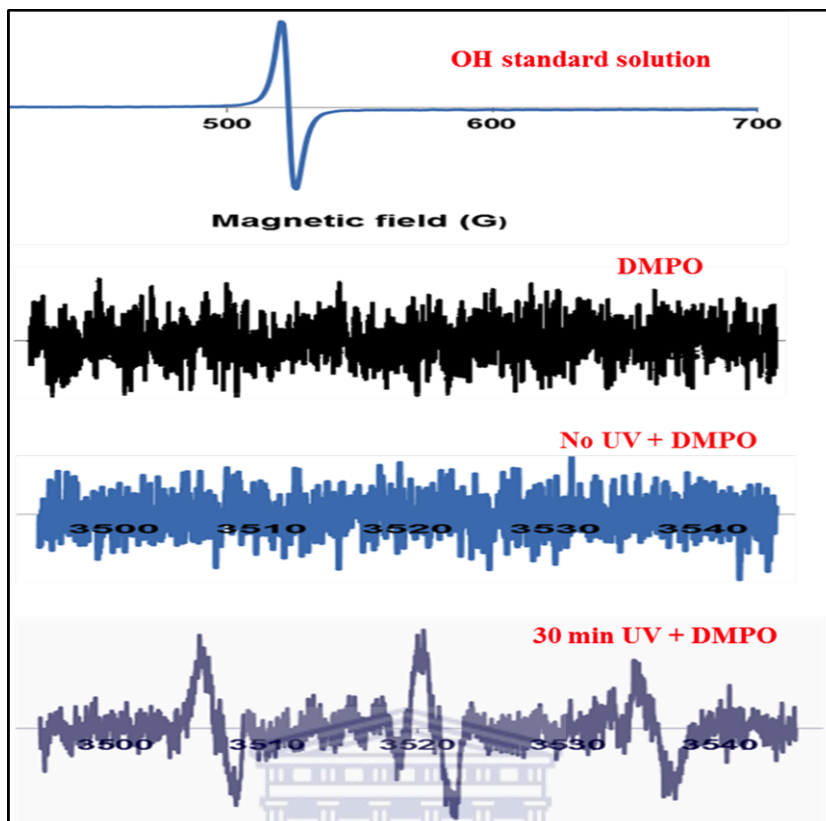


Figure 5.21: Summary of the results of OH radical detection using ESR.

From the OH radical standard solution, the ESR intensity peak is observed between the magnetic field values 500 to 550 G. The DMPO solution did not show any intensity peak, but just noise. The sample with DMPO mixed with treated water in the circulated system, but with the power switched off, thus with no UV light generation, again showed just noise. The last result was obtained after running the full OK-3 prototype system, mixed with DMPO, for 30 minutes, according to the protocol described in Section 3.5.1. The results in Figure 5.21 show that OH radicals were successfully detected. For additional clarity regarding the proof of concept, methanol was used as OH scavenger in addition to the solution. Figure 5.22 shows a summary of the results obtained with methanol added to the DMPO reagent in the water aliquot. The ESR spectrum of the DMPO-OH adduct was observed after 30 minutes of UV illumination from OK-3 for ROS reactive spin trapping with DMPO, in the presence of TiO₂ nanofibres, carbonized at 600°C in nitrogen (see Section 3.5.2).

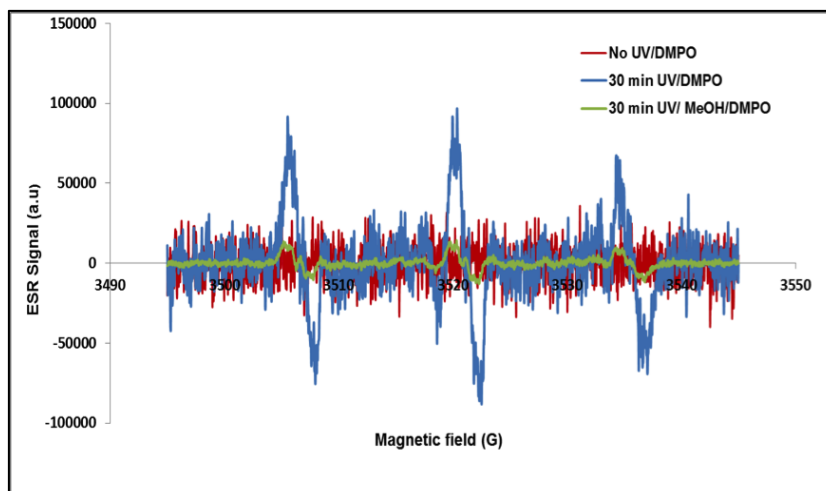


Figure 5.22: Compilation of ESR peak spectra of DMPO-OH adduct observed before and after power on.

To determine whether OH radicals were present in electrolyzed water as indicated in Section 3.5 and 3.5.2, samples from the aliquot water were collected during electrolysis and immediately mixed with DMPO with or without methanol. The DMPO-OH spectrum (in red) characteristic of OH radicals was not observed in the sample collected from the OK-3 reactor, with power off (no UV irradiation). The spectrum (in blue) characteristic of OH radicals was observed with the high peaks in the sample collected from the OK-3 reactor, with power on after 30 minutes running time, without methanol. Finally, the spectrum (in green) characteristic of OH radicals was observed with reduced peaks after the same running time (30 minutes) in the sample mixed with methanol, which inhibits the process collected from the OK-3 reactor, with power on. It is well established that OH radicals are generated through the OK-3 reactor and indirectly detected using ESR and methanol as scavenger. Methanol can serve as an alternative spin trapping compound to detect OH radicals in illuminated TiO₂ nanofibres by electron paramagnetic resonance (Schwarz et al., 1997).

After OH radical detection, the next active species to detect was O₃ (ozone). The technique or methodology that was used as proof of concept was discussed in Section 3.5.3.

5.3.2 Ozone detection

It is well-known that ozone is produced through the electric discharge from corona, as was discussed in the literature review. The ozone generated by oxygen or air flowing through the electric discharge area of the OK-3 prototype reactor can be detected using a titrimetric technique that involves bubbling the effluent gas through an aqueous solution of potassium iodide. The photograph in Figure 5.23 shows the change of colour due to the contact of ozone and a 0.1 M solution of KI, which indicates the presence of ozone formation by the prototype OK-3.

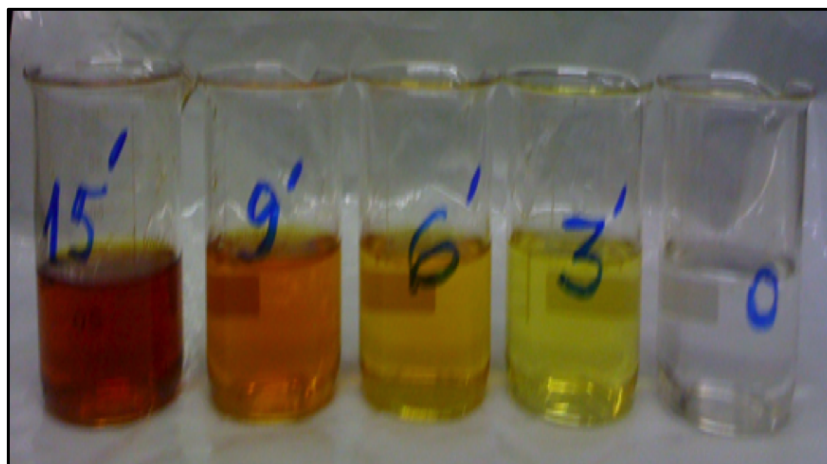


Figure 5.23: The change of colour when ozone is bubbled in a 0.1M solution of KI.

As indicated in Section 3.5.3, to assess the total amount of ozone produced during the streamer discharges, the ozone was collected in a gas plenum above the reactor and ventilated through a bottle filled with an iodide solution. The ozone reacts with the potassium iodide solution and forms a yellow iodine complex (Gilbert et al., 1970).

5.3.3 Hydrogen peroxide detection

This section involved the detection of the third active species, hydrogen peroxide (H₂O₂), using a colorimetric method with titanyl ions, as described in Section 3.5.4. This well-known colorimetric method was proposed by Eisenberg (Eisenberg et al., 1943) and is based on the photometric analysis of the intense yellow-orange colour appearing in a solution containing hydrogen peroxide, after the addition of titanyl sulphate. The yellow colour produced is due to peroxotitnylsulfonic acid. The reaction of H₂O₂ with the reagent takes place as follows:

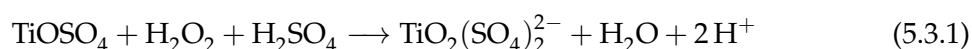


Figure 5.24 shows the colour change from colourless to yellow, as stated by the Eisenberg method, which confirmed the presence of hydrogen peroxide as proof of concept.

The detection of OH radical signals using TiO₂ nanofibres in the prototype OK-3 (Rouppla) system indicates the performance of the photocatalyst induced during UV irradiation. On the other hand, the colour changes observed during the contact of gas from the electrohydraulic discharge reactor OK-3 with 0.1M KI, indicate the presence of ozone. In addition, the interaction with the titanyl sulphate solution indicate the presence of hydrogen peroxide. This means that a cocktail of active species, which target and destroy the organic compounds in polluted water, was produced, which was the main purpose of this project.

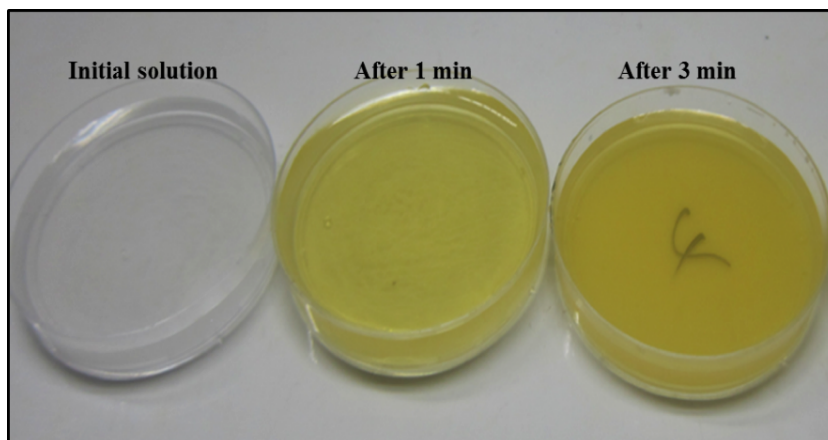


Figure 5.24: The colour changes that occur when hydrogen peroxide reacts with titanyl sulphate.

5.4 Ion Chromatograph-Mass Spectra (IC-MS) results

This section presents the results obtained from studies on the identification and the cause of the pH decrease that was observed when the prototype OK-3 was running up to 60 minutes. The experimental procedures are as indicated in Section 3.5.5 and the observed results of the pH decrease are shown in Figure 4.9. The IC-MS experiment was conducted to determine the chemical elements in the treated water, which caused the decrease in pH from 6 to 2. The hypothesis was that water splitting produced more ions, which increased the conductivity of the solution. On the other hand, the discharge of air through the corona produced the ozone, and nitrogen was transformed to NO in water (Locke et al., 1995). The NO that is formed is easily oxidized to NO₂, and when the gas from the OK-3 reactor is transferred to the wastewater, NO₂, coexisting with ozone, is dissolved to form nitric acid and nitrous acid, as reported by Sathiamoorthy et al. (1999). Figure 5.25 shows the chemical elements that were detected, such as fluoride, chloride, nitrite, nitrate and sulphate, after different running times.

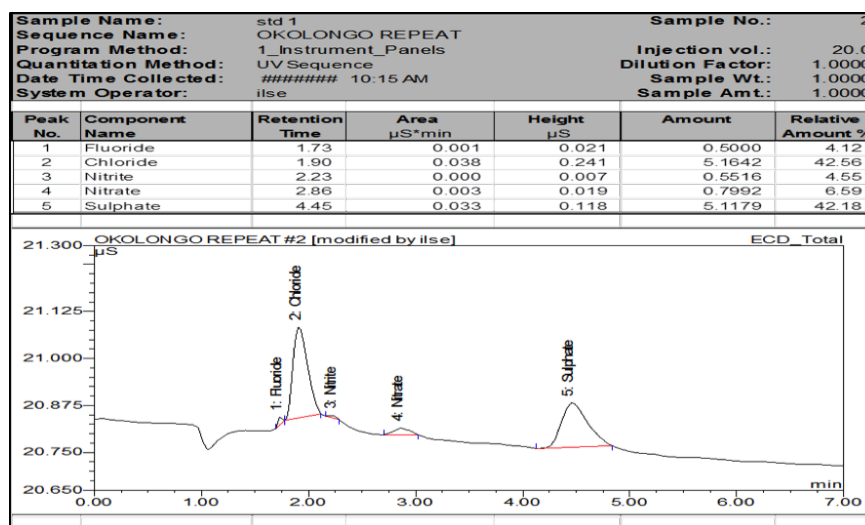


Figure 5.25: The intensity peaks of different standard solutions.

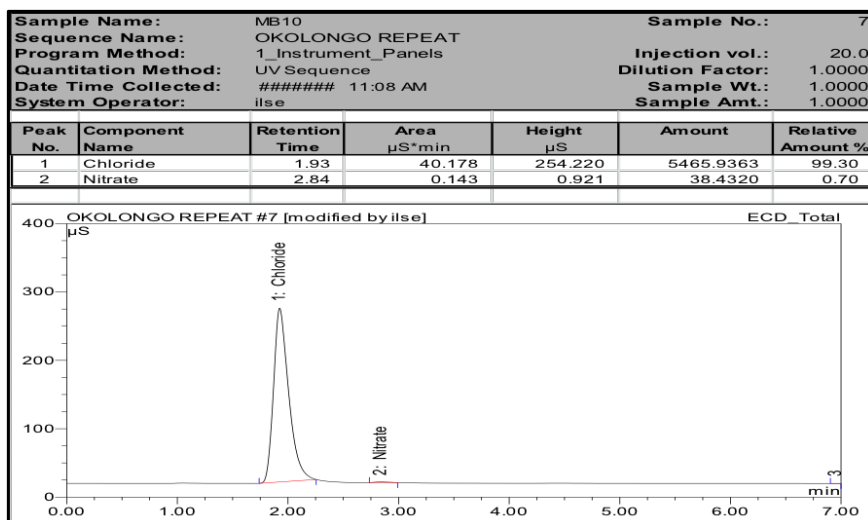


Figure 5.26: The intensity peaks of the MB solution after 10 minutes.

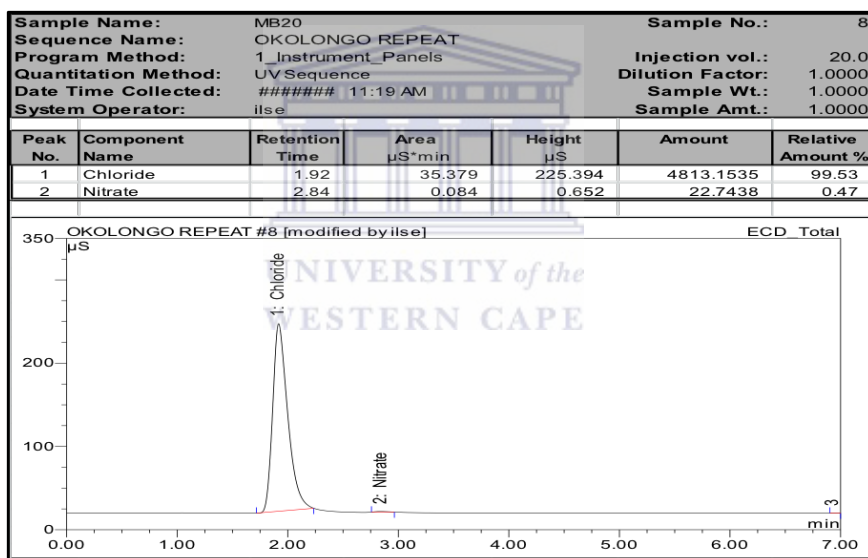


Figure 5.27: The intensity peaks of the MB solution after 20 minutes.

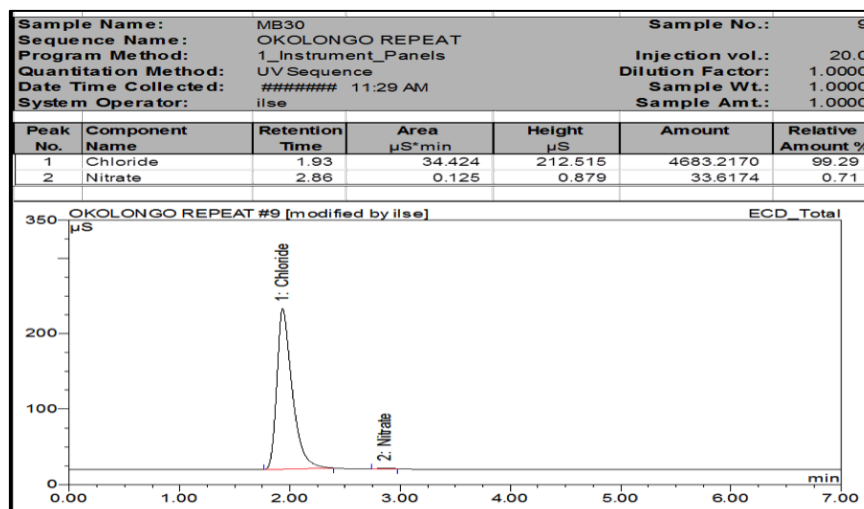


Figure 5.28: The intensity peaks of the MB solution after 30 minutes.

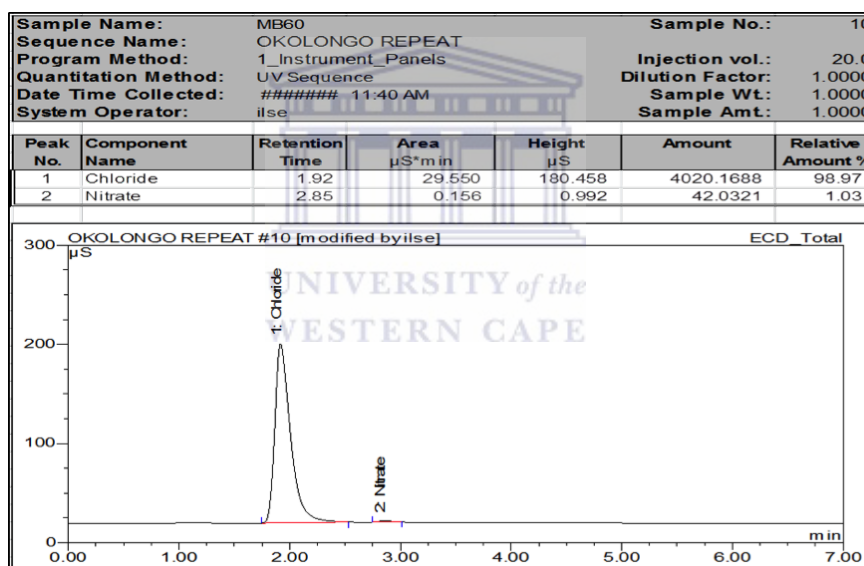


Figure 5.29: The intensity peaks of the MB solution after 60 minutes.

Looking at Figures 5.25 to 5.29 it is evident that the pH decrease was not caused by the air flowing through the discharge reactor, which could lead to the formation of nitric acid, since nitrate was not detected. The pH decrease was probably caused by the plasma, which led to ionisation or water splitting, that produced more ions, thus increasing the conductivity of the solution.

Chapter 6

Conclusions and Recommendations

This chapter summarizes the findings of this thesis by presenting an overview of the achievements of the research objectives, a discussion of the importance and contributions of the results from a scientific and industrial point of view, and provides recommendations for future work.

6.1 Introduction

The aim of this work was threefold. Firstly, to design the concept for a scalable electrohydraulic discharge reactor based on corona discharge for a water treatment system. Secondly, to establish a suitable, simple method to fabricate composite TiO₂ nanofibres immobilised on a metal grid in the anatase structure, using an electrospinning technique, and thirdly, to integrate the synthetic immobilized TiO₂ nano photocatalytic material in the prototype reactor, for the production of active species such as OH radicals, ozone and hydrogen peroxide, as a cocktail to clean polluted water without the addition of chemicals.

6.2 Conclusions

Initially electrohydraulic discharge reactors were designed, based on corona discharge principles, using different prototype configurations, namely OK-1, OK-2 and OK-3, to check their performance and limitations as described in Sections 3.2.3.1, 3.2.3.2 and 3.2.3.3 respectively.

A prototype OK-3 reactor was found to be the best configuration. It was not only a source of active species produced in-situ in the water zone for water treatment, but also a continuous source of UV irradiation, to initiate the photocatalysis process if catalysts are exposed to it. This increased the photo-degradation of Methylene blue (MB), the model water pollutant chosen, within 30 minutes. The UV-Vis, NMR, FT-IR and HPLC results showed that MB was completely mineralized to CO₂ and H₂O by the attack of active species, such as ozone, OH radicals and H₂O₂. It was found that the UV irradiation had a close relationship to the initial discharge from the power supply, as well as the conductivity of

the water to be treated. The result showed that the UV light increased with an increase of conductivity.

It was also found that a novel and simple method to fabricate composite TiO₂ nanofibres, immobilised on a metal grid, in the anatase structure, was devised using an electrospinning technique, followed by a calcination process. The crystal structure, morphologies, surface area and the photocatalytic activity of synthesized TiO₂ nanofibres were characterised by X-ray diffraction (XRD), transmission electron microscopy (TEM), scanning electron microscopy (SEM), Brunauer-Emmett-Teller (BET), nitrogen adsorption desorption isotherm, and UV-Vis spectroscopy.

The results revealed that hydrolysis of electrospun fibres, followed by carbonization at specific temperatures, had greatly influenced the morphologies and immobilization of TiO₂ nanofibres on the supported material. The composite anatase nanocrystals formed were stable, even after 10 minutes of sonication. The photocatalytic activities of the TiO₂ nanofibres and anatase nanocomposites were evaluated by photocatalytic degradation of Methylene blue (MB), in water, under UV light irradiation originating from the electrohydraulic discharge. It was observed that the TiO₂ nano-crystalline composites obtained by calcination at 600°C for 2 hours, exhibited higher photocatalytic activity than the commercial powder Degussa P-25.

The best degradation and inactivation results of my system were achieved with 36 W compared to 200 W used by Lihua Xu's research (Lihua et al., 2010) and 500 W used by Holger Krause's research (Krause et al., (2009), and Vanessa Joubert's research (Joubert et al., (2013).

This combined advanced oxidation design and the integration of synthetic TiO₂ nanofibres in the OK-3 reactor have great commercial potential in realizing low cost and low power consumption water purification without the addition of chemicals. It was found that the production of reactive oxidants like OH radicals, ozone and H₂O₂, combined with the appearance of UV radiation, and a strong electric field, enhanced the disinfection and photo degradation efficiency. Mainly by using suitable chemical probes, it has been possible to successfully detect the formation of OH radicals, ozone and H₂O₂ as a cocktail. It has been shown that an electrohydraulic discharge reactor has great potential as a water disinfection method, compared to the solar disinfection method (SODIS), internationally recommended to the developing countries. It also has a more powerful effect than many other conventional technologies.

6.3 Significance of the current study to the scientific and industrial community

Existing methods for water disinfection cannot always be used, because they are either too expensive, have unwanted by-products or simply do not work. One promising approach is to create various active species in-situ, so that transport losses and handling of chemicals can be avoided. Within this context, great attention has been given to so-called "Advanced

Oxidation Processes" (AOP). AOP are defined as water treatment processes that involve an input of energy (either chemical, electrical or radiative) into the water matrix to produce highly reactive species as intermediates, which then attack and destroy the target in water. When a strong electric field is applied to water, i.e. electrohydraulic discharge, there are a variety of chemical and physical reactions that can take place, as one of AOP processes.

Electrohydraulic discharges have been studied for many years. However, the integration of innovations in nanoscience and nanotechnology has been incorporated into this area of work on a very limited scale. The present project was focused on the development of a unique electrohydraulic discharge reactor in which multiple electrodes across the water flow path were incorporated. TiO₂ nanofibres, immobilized on a grid, were integrated into the reactor to enhance the photocatalysis process and the production of OH radicals by using the permanent UV radiation from the corona discharge.

Some of the anticipated outcomes from the current approach include:

1. Decreased discharge load on each electrode for the generation of the plasma.
2. Generation of active species (e.g. hydroxyl radicals) across multiple electrodes, and with the use of the nanowire arrays, a decrease in the overall power consumption of the system.
3. The lower discharge load per electrode should enhance the erosion resistance of the system as whole, and will increase the lifetime of the system considerably.
4. Due to the short lifetime of the radicals produced, such as hydroxyl radicals, the multiple electrodes in the system will provide several sources of active species along the water flow path, and thus maximize microorganism exposure and eventual removal. The synergetic combination of physical and chemical effects will play the major role in the very effective destruction of microorganisms in the water.

The novel findings from this thesis are of importance to both the scientific and industrial community. The significance of the contributions from this research can be summarized as follows:

1. It was shown that the unique prototype OK-3, configured with multiple electrodes across the water flow path, performed better in the degradation and inactivation of organic dyes and microorganisms from drinking water, respectively. It also used a very low potential (12 kV) compared to other prototypes, mentioned previously in the literature. This should stimulate interest by the water sector industries to optimize the conditions that were identified for treating water without adding chemicals. It was also shown that the prototype produced permanent UV radiation with specific parameters.
2. The identified synthesis route, leading to the formation of the novel morphology (hierarchical) of TiO₂ nanofibres immobilized on a grid supporting material, using an

electrospinning method, without requiring additional ingredients or post synthesis treatment, but just the hydrolysis of the nano-woven material before calcination, is advantageous compared to the existing, complicated procedures to make hierarchical catalysts which are reported in literature, that are based either on chemical or physical techniques. This quick synthesis route is expected to be a low cost alternative to the commercial P-25 Degussa, which is used as slurry, leading to costly post treatment to separate nanoparticles from the treated water.

3. The integration of TiO₂ nanofibres, immobilized on grid, into the electrohydraulic discharge reactor OK-3, enhances the photocatalysis process and OH radical production, using the permanent UV radiation from the corona discharge. Consequently, the degradation and inactivation were performed with an effective power supply consumption of 36W, compared to the 200W and 500W reported in the literature by other researchers, as mentioned previously.

6.4 Recommendations for future work

As stated previously, there remains a significant amount of uncertainty regarding the technical and economic effectiveness of AOPs for removing pollutants from drinking water under a variety of water quality scenarios. More pilot- and field-scale studies need to be conducted to determine the removal efficiencies that can be achieved under different water quality conditions and operational parameters. Therefore, a new, detailed design made in collaboration with engineering students from Cape Peninsula University of Technology (CPUT) and a design company can be found in Appendix B.

In addition, the following specific topics warrant further research:

1. Optimization of sol-gel solutions with regards to the ratio concentration of precursors, solvents, conductivities and viscosity for the electrospinning process.
2. Optimization of the calcination and carbonization of nanofibres, changing the different rates and temperatures for the proper formation of nanoparticle crystals.
3. Optimization of the reactor configuration, using copper wire electrodes, and then the replacement of the initial conventional electrodes with nanowire arrays will be the overall aim for optimizing energy consumption.
4. Carbonization of TiO₂ nanofibres at higher temperatures (more than 1000°C). Flowing nitrogen through the furnace might lead to a doping process and the formation TiN, which could be beneficial.
5. Quantification of active species production from an electrohydraulic discharge reactor in order to optimize the production conditions and parameters.

Appendices



UNIVERSITY *of the*
WESTERN CAPE

Appendix A

Summary of Advanced Oxidative Processes

AOP Technology	Brief Description	System Components	Advantages	Disadvantages
Emerging Technologies continued				
Sonication/ Hydrodynamic Cavitation	Sonication or hydrodynamic processes induce the formation of cavitation microbubbles. These bubbles implode violently after reaching a critical resonance size and generate high temperatures and highly reactive radicals. Removal of organics occurs by thermal decomposition at the bubble-water interface and by reaction with the radicals. Oxidation by cavitation is enhanced by the addition of O_3 or H_2O_2 .	<ul style="list-style-type: none"> Hydrodynamic/Ultrasonic Cavitation Generator Reactor Chamber Chemical Feed Tanks and Pumps Power Source Temperature Controller Supply and Discharge Pumps and Piping Monitoring & Control Systems 	<ul style="list-style-type: none"> Simple design resulting in minimal maintenance costs. Energy usage comparable to AOPs using UV. No bromate formation potential if O_3 is not added. Less heat transfer relative to UV system. No off-gas treatment required if O_3 is not used. 	<ul style="list-style-type: none"> No full-scale applications exist. Supplemental oxidants such as O_3 and H_2O_2 may be required to achieve target removal efficiencies, resulting in increased costs.
TiO₂-Catalyzed UV Oxidation	When TiO_2 is illuminated by UV light, valence band electrons are excited to the conduction band, resulting in the formation of holes. These holes react with water molecules to produce hydroxyl and other radicals that in turn oxidize organic compounds. Formation of H_2O_2 intermediate can also assist the overall oxidation process.	<ul style="list-style-type: none"> TiO_2 Slurry Injection and Extraction System (Option-1) TiO_2 Impregnated Resin Fluidized Bed Reactor (Option-2) Ultraviolet Lamps, Lamp Sleeves, and Lamp Cleaning System Static Mixer Supply and Discharge Pumps and Piping Monitoring & Control Systems 	<ul style="list-style-type: none"> No potential for bromate formation. Can be performed at higher (300-380 nm) wavelengths than other UV oxidation processes. No off-gas treatment required. 	<ul style="list-style-type: none"> No full-scale applications exist. Pre-treatment necessary to avoid fouling of the TiO_2 catalyst. If TiO_2 is added as a slurry, then a separation step is required. Potential for rapid loss of TiO_2 activity, requiring catalyst on-site storage or regeneration method. Rigorous studies needed to determine the optimum TiO_2 dose. May require oxygen sparging. Reaction efficiency is highly pH-dependent, requiring close monitoring and control.
Fenton's Reaction	Radicals, including $\bullet OH$, are produced when $Fe(II)$ reacts with H_2O_2 . Destruction of organic matter occurs by reaction with these radicals. Iron acts as a catalyst for this reaction.	<ul style="list-style-type: none"> $Fe(II)$ and Hydrogen Peroxide Storage and Injection Systems Completely Stirred Tank Reactor pH Controllers Iron Removal System Supply and Discharge Pumps and Piping Monitoring & Control Systems 	<ul style="list-style-type: none"> No potential for bromate formation. Not an energy intensive process compared to AOPs that utilize O_3 or UV. No off-gas treatment required. 	<ul style="list-style-type: none"> No full-scale applications exist. Requires iron extraction system. Very low pH (< 2.5) is required to keep the iron in solution. pH adjustment will increase operation and maintenance costs.

<p>TiO₂-Catalyzed UV Oxidation</p>	<p>When TiO₂ is illuminated by UV light, valence band electrons are excited to the conduction band, resulting in the formation of holes. These holes react with water molecules to produce hydroxyl and other radicals that in turn oxidize organic compounds. Formation of H₂O₂ intermediate can also assist the overall oxidation process.</p>	<ul style="list-style-type: none"> • TiO₂ Slurry Injection and Extraction System (Option-1) • TiO₂ Impregnated Resin Fluidized Bed Reactor (Option-2) • Ultraviolet Lamps, Lamp Sleeves, and Lamp Cleaning System • Static Mixer • Supply and Discharge Pumps and Piping • Monitoring & Control Systems 	<ul style="list-style-type: none"> • No potential for bromate formation. • Can be performed at higher (300-380 nm) wavelengths than other UV oxidation processes. • No off-gas treatment required. 	<ul style="list-style-type: none"> • No full-scale applications exist. • Pre-treatment necessary to avoid fouling of the TiO₂ catalyst. • If TiO₂ is added as a slurry, then a separation step is required. • Potential for rapid loss of TiO₂ activity, requiring catalyst on-site storage or regeneration method. • Rigorous studies needed to determine the optimum TiO₂ dose. • May require oxygen sparging. • Reaction efficiency is highly pH-dependent, requiring close monitoring and control.
<p>Fenton's Reaction</p>	<p>Radicals, including •OH, are produced when Fe (II) reacts with H₂O₂. Destruction of organic matter occurs by reaction with these radicals. Iron acts as a catalyst for this reaction.</p>	<ul style="list-style-type: none"> • Fe(II) and Hydrogen Peroxide Storage and Injection Systems • Completely Stirred Tank Reactor • pH Controllers • Iron Removal System • Supply and Discharge Pumps and Piping • Monitoring & Control Systems 	<ul style="list-style-type: none"> • No potential for bromate formation. • Not an energy intensive process compared to AOPs that utilize O₃ or UV. • No off-gas treatment required. 	<ul style="list-style-type: none"> • No full-scale applications exist. • Requires iron extraction system. • Very low pH (< 2.5) is required to keep the iron in solution. • pH adjustment will increase operation and maintenance costs.

<p>TiO₂-Catalyzed UV Oxidation</p>	<p>When TiO₂ is illuminated by UV light, valence band electrons are excited to the conduction band, resulting in the formation of holes. These holes react with water molecules to produce hydroxyl and other radicals that in turn oxidize organic compounds. Formation of H₂O₂ intermediate can also assist the overall oxidation process.</p>	<ul style="list-style-type: none"> • TiO₂ Slurry Injection and Extraction System (Option-1) • TiO₂ Impregnated Resin Fluidized Bed Reactor (Option-2) • Ultraviolet Lamps, Lamp Sleeves, and Lamp Cleaning System • Static Mixer • Supply and Discharge Pumps and Piping • Monitoring & Control Systems 	<ul style="list-style-type: none"> • No potential for bromate formation. • Can be performed at higher (300-380 nm) wavelengths than other UV oxidation processes. • No off-gas treatment required. 	<ul style="list-style-type: none"> • No full-scale applications exist. • Pre-treatment necessary to avoid fouling of the TiO₂ catalyst. • If TiO₂ is added as a slurry, then a separation step is required. • Potential for rapid loss of TiO₂ activity, requiring catalyst on-site storage or regeneration method. • Rigorous studies needed to determine the optimum TiO₂ dose. • May require oxygen sparging. • Reaction efficiency is highly pH-dependent, requiring close monitoring and control.
<p>Fenton's Reaction</p>	<p>Radicals, including •OH, are produced when Fe (II) reacts with H₂O₂. Destruction of organic matter occurs by reaction with these radicals. Iron acts as a catalyst for this reaction.</p>	<ul style="list-style-type: none"> • Fe(II) and Hydrogen Peroxide Storage and Injection Systems • Completely Stirred Tank Reactor • pH Controllers • Iron Removal System • Supply and Discharge Pumps and Piping • Monitoring & Control Systems 	<ul style="list-style-type: none"> • No potential for bromate formation. • Not an energy intensive process compared to AOPs that utilize O₃ or UV. • No off-gas treatment required. 	<ul style="list-style-type: none"> • No full-scale applications exist. • Requires iron extraction system. • Very low pH (< 2.5) is required to keep the iron in solution. • pH adjustment will increase operation and maintenance costs.

Appendix B

Details of the new design reactor (OK-3)

Even though all the initial objectives that were set for this study were achieved, there are still some other aspects which were not within the scope of this study, either due to time or resource constraints, that were not fully explored and could serve as areas of future investigations. As supported and sponsored by the Water Research Commission (WRC), Project #: K5 1897 NANOTECHNOLOGY IN WATER TREATMENT, the following Figures (B-1 to B-13) are different aspects of the new design reactor, composed with 5 coppers electrodes that need more attention for the on-going research until optimisation is made toward the implementation of the system for water treatment in the rural areas.

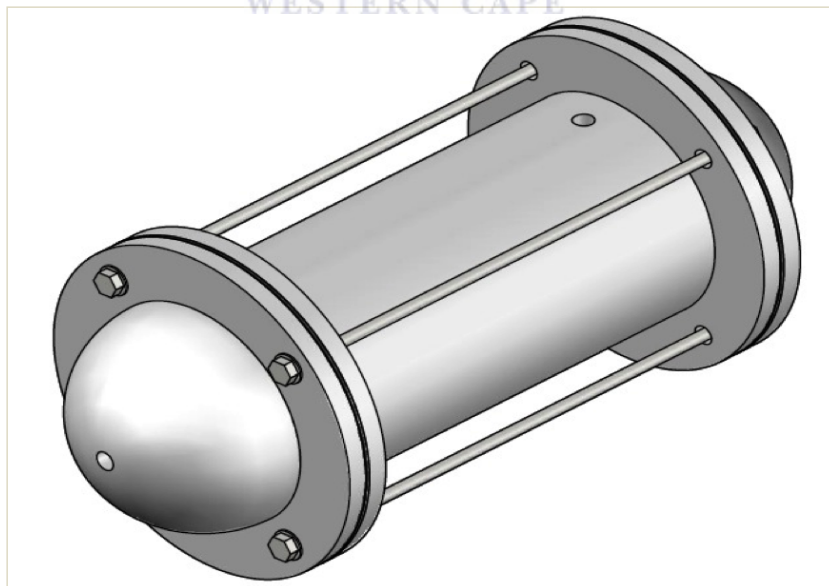


Figure B.1: Fully assembled reactor vessel

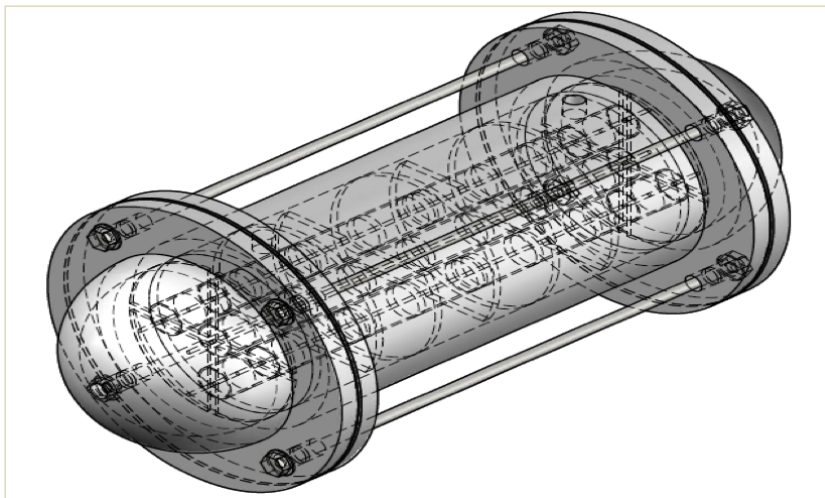


Figure B.2: Fully assembled reactor vessel (wire frame view)

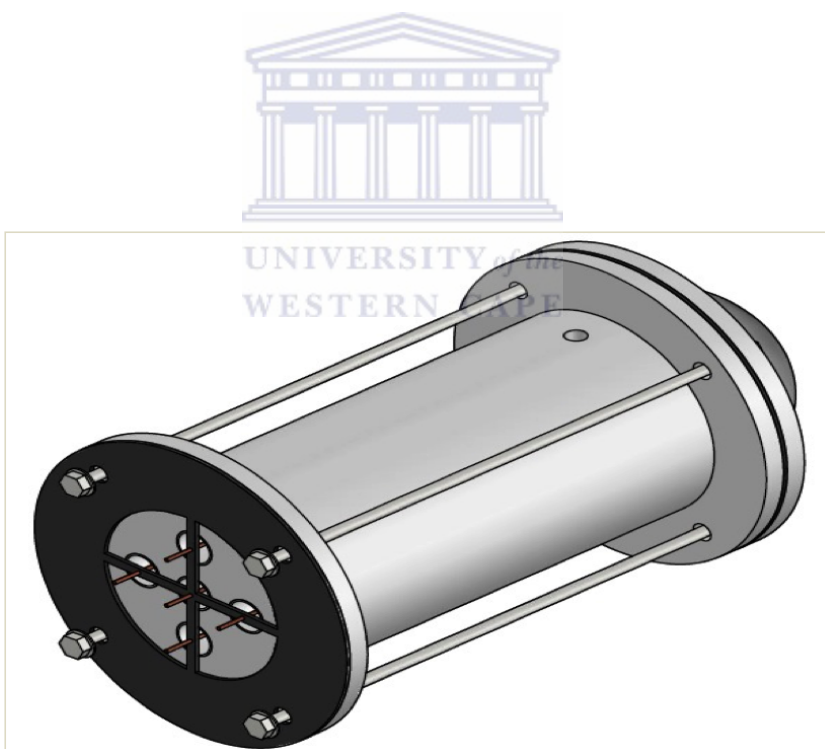


Figure B.3: Reactor vessel with end cap removed

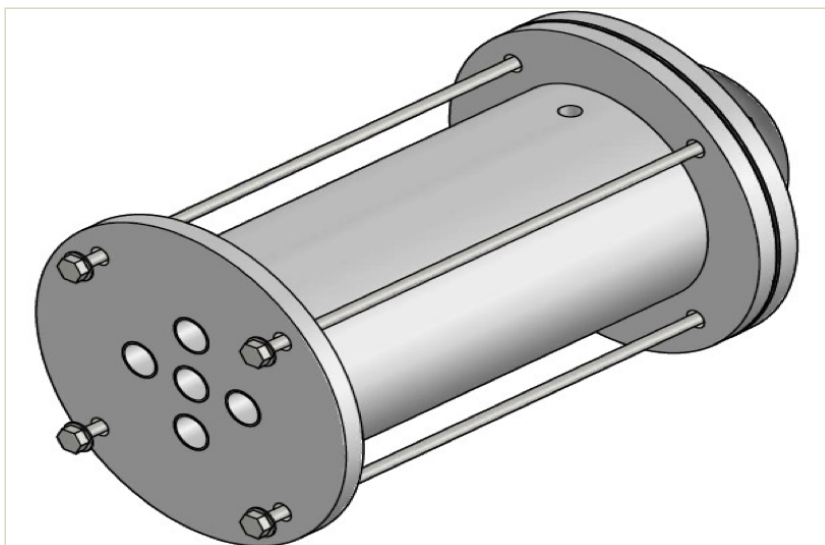


Figure B.4: Reactor vessel with electrode placement disk and electrodes removed

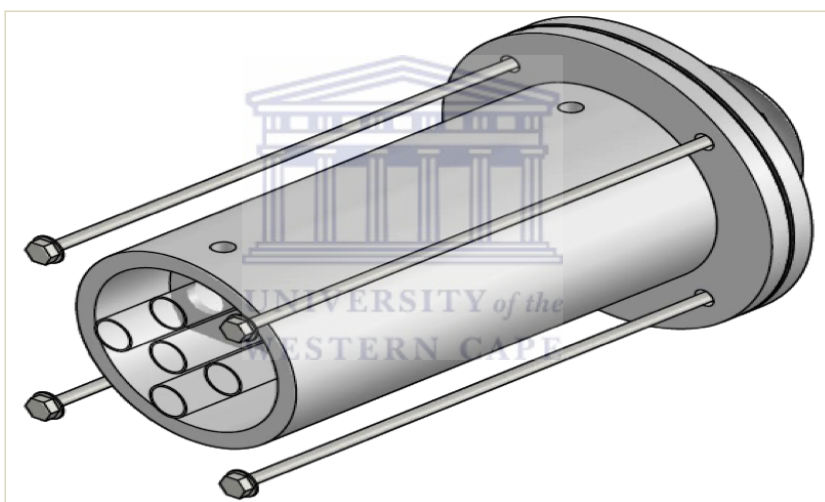


Figure B.5: Reactor with shell flange removed

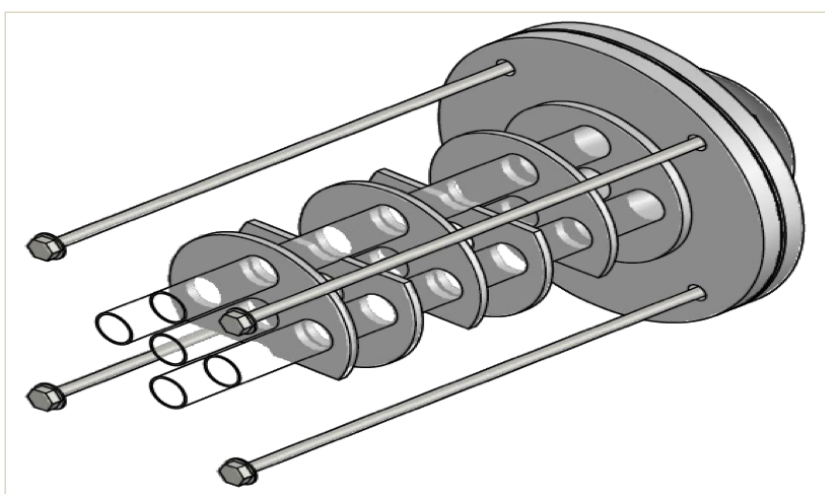


Figure B.6: Reactor vessel with shell removed

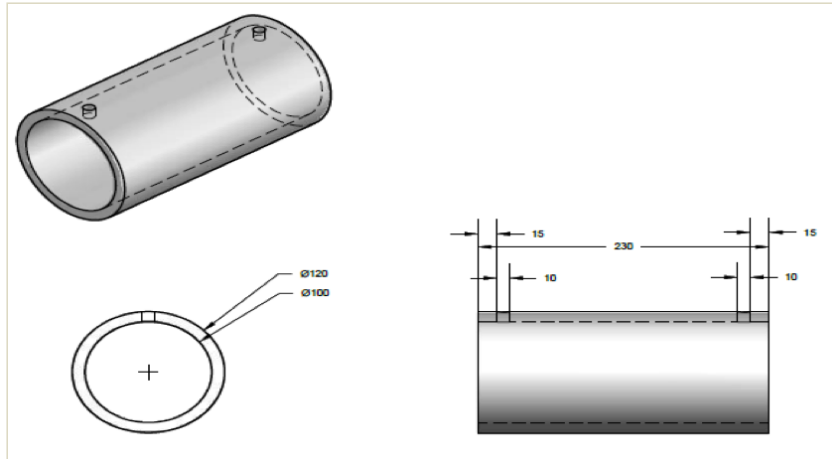


Figure B.7: Perspex shell dimensions

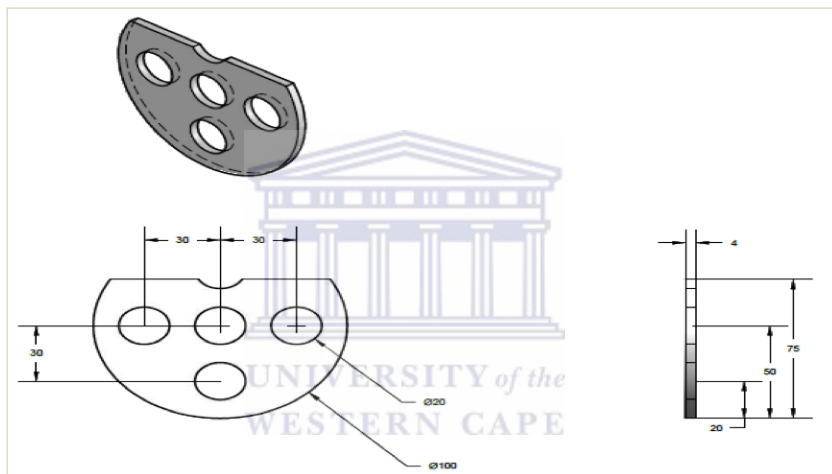


Figure B.8: Teflon baffle dimensions

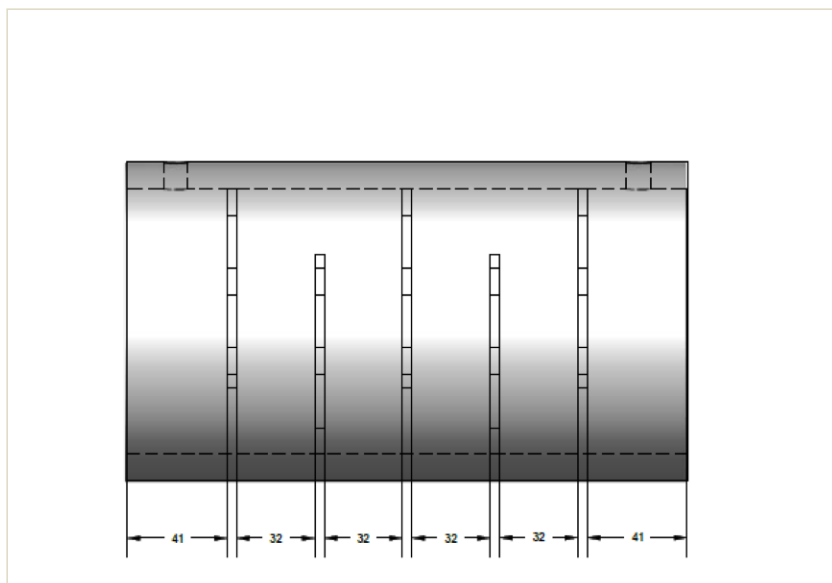


Figure B.9: Baffle placement in shell

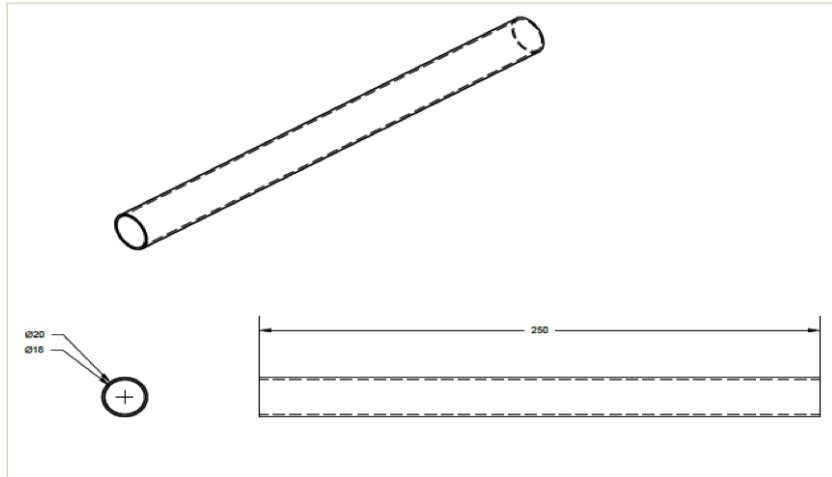


Figure B.10: Quartz tube dimensions

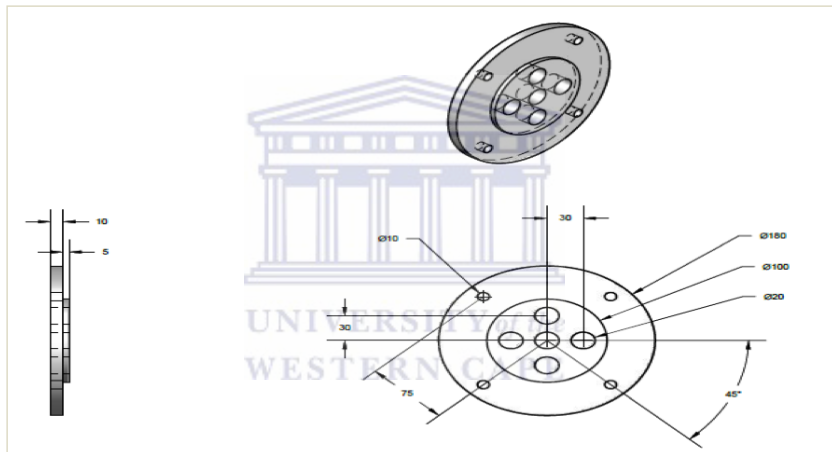


Figure B.11: Teflon shell flange dimensions

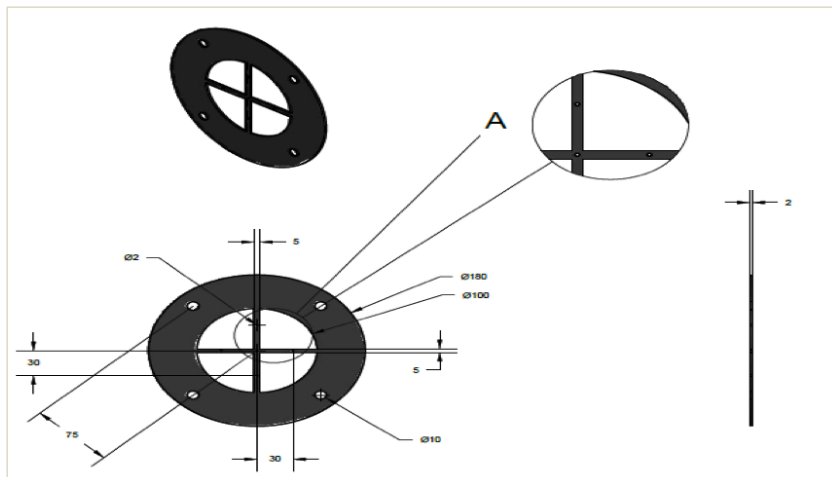


Figure B.12: Teflon electrode placement disk dimensions

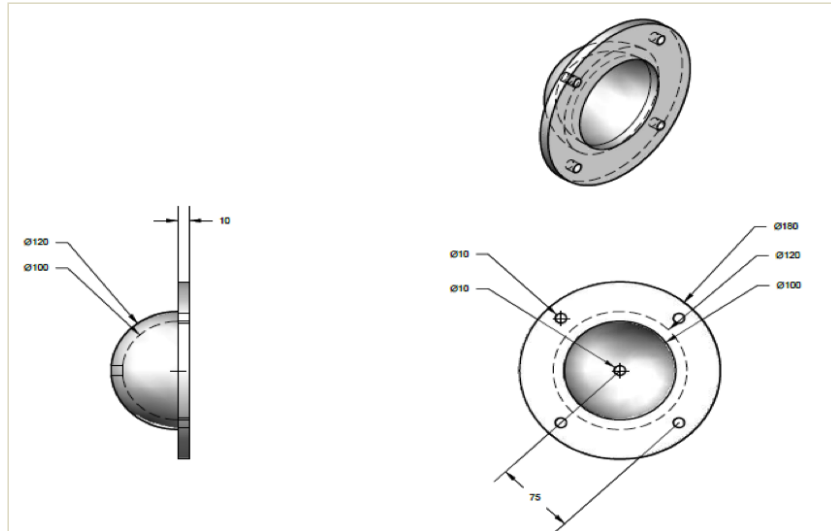


Figure B.13: Perspex end cap dimensions



Appendix C

SEM images of different samples



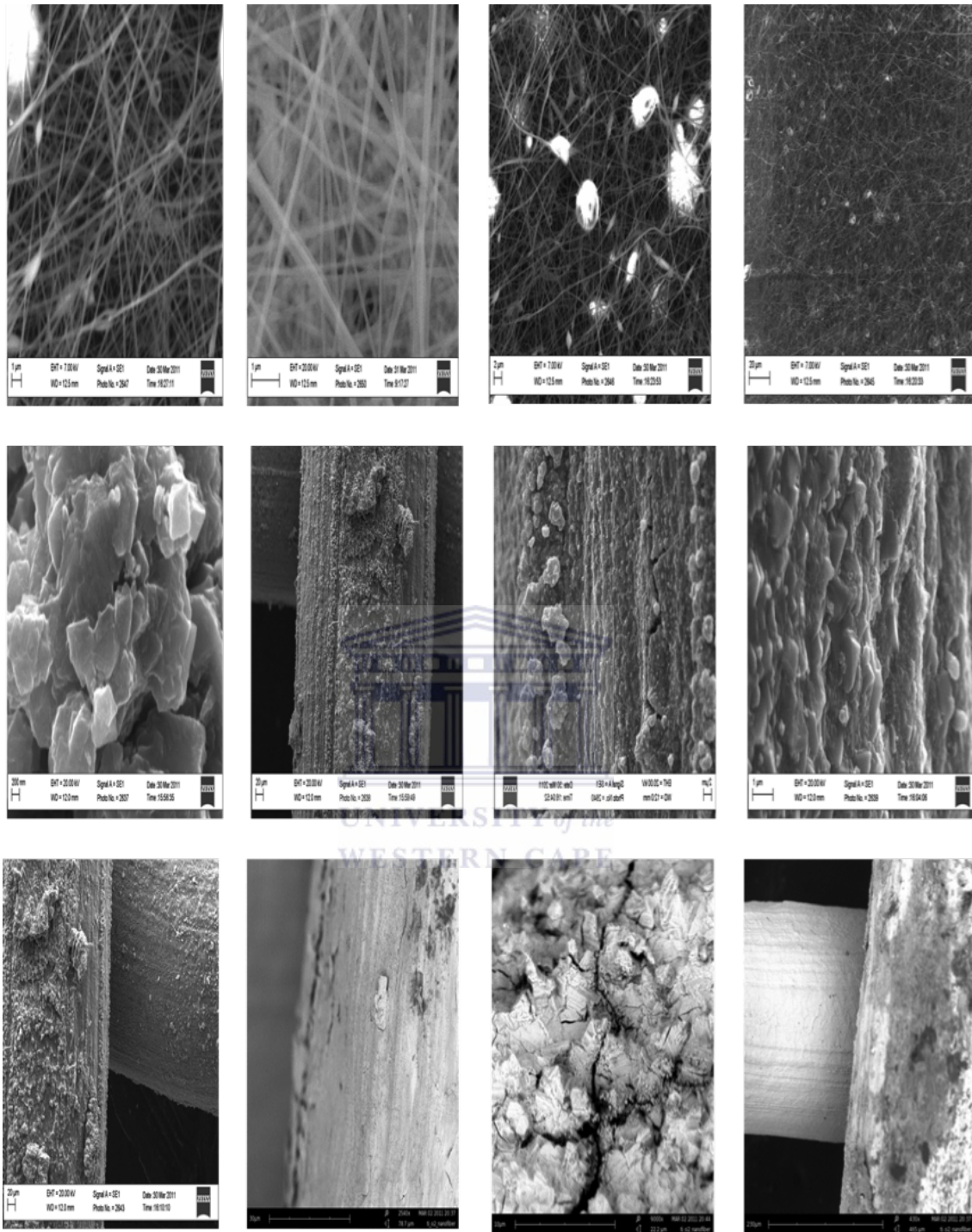


Figure C.1: SEM images of different samples

List of References

Adohi, B. J. P., Mdarhri, A., Prunier, C., Haidar, B., and Brosseau, C. (2010) A Comparison between Physical Properties of Carbon Black-Polymer and Carbon Nanotubes-Polymer Composites, *Journal of Applied Physics* 108, 074108.

Akpan, U., and Hameed, B. (2009) Parameters Affecting the Photocatalytic Degradation of Dyes Using TiO₂-Based Photocatalysts: A Review, *Journal of Hazardous Materials* 170, 520-529.

Ali, H. (2010) Biodegradation of Synthetic Dyes: A Review, *Water, Air & Soil Pollution* 213, 251-273.

An, G., Ma, W., Sun, Z., Liu, Z., Han, B., Miao, S., Miao, Z., and Ding, K. (2007) Preparation of Titania/Carbon Nanotube Composites Using Supercritical Ethanol and Their Photocatalytic Activity for Phenol Degradation under Visible Light Irradiation, *Carbon* 45, 1795-1801.

Anandan, S., Sathish Kumar, P., Pugazhenthiran, N., Madhavan, J., and Maruthamuthu, P. (2008) Effect of Loaded Silver Nanoparticles on TiO₂ for Photocatalytic Degradation of Acid Red 88, *Solar Energy Materials & Solar Cells* 92, 929-937.

Arico, A. S., Bruce, P., Scrosati, B., Tarascon, J. M., and Van Schalkwijk, W. (2005) Nanostructured Materials for Advanced Energy Conversion and Storage Devices, *Nature Materials* 4, 366-377.

Asahi, R., Morikawa, T., Ohwaki, T., Aoki, K., and Taga, Y. (2001) Visible-Light Photocatalysis in Nitrogen-Doped Titanium Oxides, *Science* 293, 269.

Banerjee, S. G., and Morella, E. (2011) Africa's Water and Sanitation Infrastructure: Access, Affordability and Alternatives, World Bank Publications.

Baruah, S., and Dutta, J. (2009) Nanotechnology Applications in Pollution Sensing and Degradation in Agriculture: A Review, *Environmental Chemistry Letters* 7, 191-204.

Bautista, P., Mohedano, A., Casas, J., Zazo, J., and Rodriguez, J. (2008) An Overview of the

Application of Fenton Oxidation to Industrial Wastewaters Treatment, *Journal of Chemical Technology & Biotechnology* 83, 1323-1338.

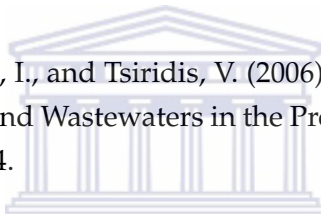
Baxter, J., Bian, Z., Chen, G., Danielson, D., Dresselhaus, M. S., Fedorov, A. G., Fisher, T. S., Jones, C. W., Maginn, E., and Kortshagen, U. (2009) Nanoscale Design to Enable the Revolution in Renewable Energy, *Energy Environ. Sci.* 2, 559-588.

Been, J., and Grauman, J. (2000) Titanium and Titanium Alloys, *Uhlig's Corrosion Handbook*, 861-878.

Behnajady, M., Modirshahla, N., Shokri, M., and Rad, B. (2008) Enhancement of Photocatalytic Activity of TiO₂ Nanoparticles by Silver Doping: Photo Deposition Versus Liquid Impregnation Methods, *Global NEST Journal* 10, 1-7.

Beydoun, D., Amal, R., Low, G., and McEvoy, S. (1999) Role of Nanoparticles in Photocatalysis, *Journal of Nanoparticle Research* 1, 439-458.

Bizani, E., Fytianos, K., Poullos, I., and Tsiridis, V. (2006) Photocatalytic Decolorization and Degradation of Dye Solutions and Wastewaters in the Presence of Titanium Dioxide, *Journal of Hazardous Materials* 136, 85-94.



Blackmond, D. G. (2005) Reaction Progress Kinetic Analysis: A Powerful Methodology for Mechanistic Studies of Complex Catalytic Reactions, *Angewandte Chemie International Edition* 44, 4302-4320.

Borup, R., Meyers, J., Pivovar, B., Kim, Y. S., Mukundan, R., Garland, N., Myers, D., Wilson, M., Garzon, F., and Wood, D. (2007) Scientific Aspects of Polymer Electrolyte Fuel Cell Durability and Degradation, *Chemical Reviews* 107, 3904-3951.

Brown, O., Hammill, A., and McLeman, R. (2007) Climate Change as the New Security Threat: Implications for Africa, *International Affairs*, Vol. 83, No. 6, pp. 1141-1154, November 2007.

Carballa, M., Omil, F., Lema, J. M., Llompart, M., Garcia-Jares, C., Rodríguez, I., Gómez, M., and Ternes, T. (2004) Behavior of Pharmaceuticals, Cosmetics and Hormones in a Sewage Treatment Plant, *Water research* 38, 2918-2926. Carp, O., Huisman, C., and Reller, A. (2004) Photoinduced Reactivity of Titanium Dioxide, *Progress in Solid State Chemistry* 32, 33-177.

Chatterjee, D., and Dasgupta, S. (2005) Visible Light Induced Photocatalytic Degradation of Organic Pollutants, *Journal of Photochemistry and Photobiology C: Photochemistry Reviews* 6, 186-205.

Chen, J., and Poon, C. (2009) Photocatalytic Construction and Building Materials: From Fundamentals to Applications, *Building and Environment* 44, 1899-1906.

Chen, X., and Mao, S. S. (2007) Titanium Dioxide Nanomaterials: Synthesis, Properties, Modifications, and Applications, *Chemical Reviews* 107, 2891-2959.

Ciardelli, G., and Ranieri, N. (2001) The Treatment and Reuse of Wastewater in the Textile Industry by Means of Ozonation and Electroflocculation, *Water Research* 35, 567-572.

Cornu, C., Colussi, A., and Hoffmann, M. (2003) Time Scales and Ph Dependences of the Redox Processes Determining the Photocatalytic Efficiency of TiO₂ Nanoparticles from Periodic Illumination Experiments in the Stochastic Regime, *The Journal of Physical Chemistry B* 107, 3156-3160.

Crini, G. (2006) Non-Conventional Low-Cost Adsorbents for Dye Removal: A Review, *Biore-source Technology* 97, 1061-1085.

Fatta-Kassinos, D., Hapeshi, E., Malato, S., Mantzavinos, D., Rizzo, L., and Xekoukoulotakis, N. P. (2010) Removal of Xenobiotic Compounds from Water and Wastewater by Advanced Oxidation Processes, *Xenobiotics in the Urban Water Cycle*, 387-412.

Fujishima, A., Rao, T. N., and Tryk, D. A. (2000) Titanium Dioxide Photocatalysis, *Journal of Photochemistry and Photobiology C: Photochemistry Reviews* 1, 1-21.

Fujishima, A., Zhang, X., and Tryk, D. A. (2008) TiO₂ Photocatalysis and Related Surface Phenomena, *Surface Science Reports* 63, 515-582.

Gao, B., Chen, G. Z., and Li Puma, G. (2009) Carbon Nanotubes/Titanium Dioxide (Cnts/TiO₂) Nanocomposites Prepared by Conventional and Novel Surfactant Wrapping Sol-Gel Methods Exhibiting Enhanced Photocatalytic Activity, *Applied Catalysis B: Environmental* 89, 503-509.

García Molina, V. (2006) Wet Oxidation Processes for Water Pollution Remediation.

Gaya, U. I., and Abdullah, A. H. (2008) Heterogeneous Photocatalytic Degradation of Organic Contaminants over Titanium Dioxide: A Review of Fundamentals, Progress and Problems, *Journal of Photochemistry and Photobiology C: Photochemistry Reviews* 9, 1-12.

Gupta, V. K., Jain, R., Nayak, A., Agarwal, S., and Shrivastava, M. (2011) Removal of the Hazardous Dye–Tartrazine by Photodegradation on Titanium Dioxide Surface, *Materials Science and Engineering: C*.

Hader, D. P., Kumar, H., Smith, R., and Worrest, R. (2007) Effects of Solar Uv Radiation on Aquatic Ecosystems and Interactions with Climate Change, *Photochemical & Photobiological Sciences* 6, 267-285.

Hallermann, F., Rockstuhl, C., Fahr, S., Seifert, G., Wackerow, S., Graener, H., Plessen, G., and Lederer, F. (2008) On the Use of Localized Plasmon Polaritons in Solar Cells, *Physica Status Solidi (A)* 205, 2844-2861.

Hameed, B., Din, A. T. M., and Ahmad, A. (2007) Adsorption of Methylene Blue onto Bamboo-Based Activated Carbon: Kinetics and Equilibrium Studies, *Journal of Hazardous Materials* 141, 819-825.

Harris, P. J. F., Hernández, E., and Yakobson, B. I. (2004) Carbon Nanotubes and Related Structures: New Materials for the Twenty-First Century, *American Journal of Physics* 72, 415.

Hasan, M. (2008) Adsorption of Reactive Azo Dyes on Chitosan/Oil-Palm Ash Composite Adsorbent: Batch and Continuous Studies [Tp918. R2 M397 2008 F Rb].

Heimer, T. A., and Heilweil, E. J. (1997) Direct Time-Resolved Infrared Measurement of Electron Injection in Dye-Sensitized Titanium Dioxide Films, *The Journal of Physical Chemistry B* 101, 10990-10993.

Hernández-Alonso, M. D., Fresno, F., Suárez, S., and Coronado, J. M. (2009) Development of Alternative Photocatalysts to TiO₂: Challenges and Opportunities, *Energy Environ. Sci.* 2, 1231-1257.

Huang, S., Woodson, M., Smalley, R., and Liu, J. (2004) Growth Mechanism of Oriented Long Single Walled Carbon Nanotubes Using "Fast-Heating" Chemical Vapor Deposition Process, *Nano Letters* 4, 1025-1028.

Huang, X. Y., Bu, H. T., Jiang, G. B., and Zeng, M. H. (2011) Cross-Linked Succinyl Chitosan as an Adsorbent for the Removal of Methylene Blue from Aqueous Solution, *International Journal of Biological Macromolecules*.

Iijima, S. (1991) Helical Microtubules of Graphitic Carbon, *Nature* 354, 56-58.

Johannesson, M. (2002) A Review of Risks Associated to Arsenic, Cadmium, Lead, Mercury and Zinc, The Market Implication of Integrated Management for Heavy Metals Flows for Bioenergy Use in the European Union, Kalmar University, Kalmar, Sweden, 115.

Joubert, V., Cheype, C., Bonnet, J., Packan, D., Garnier, JP, Teissie, J., and Blanckaert, V. (2013) Inactivation of bacillus subtilis var niger of both spore and vegetative forms by means of

corona discharges applied water, *Water Research* 47, 1381-1389

Kasprzyk-Hordern, B., Zi ek, M., and Nawrocki, J. (2003) Catalytic Ozonation and Methods of Enhancing Molecular Ozone Reactions in Water Treatment, *Applied Catalysis B: Environmental* 46, 639-669.

Kharissova, O. V., Kharisov, B. I., Valdés, J. J. R., and Méndez, U. O. (2011) Ultrasound in Nanochemistry: Recent Advances, Synthesis and Reactivity in Inorganic, *Metal-Organic, and Nano-Metal Chemistry* 41, 429-448.

Klavarioti, M., Mantzavinos, D., and Kassinos, D. (2009) Removal of Residual Pharmaceuticals from Aqueous Systems by Advanced Oxidation Processes, *Environment International* 35, 402-417.

Krause, H., Schweiger, B., Schuhmacher, J., Scoll, S., and Steinfeld, U. (2009) Degradation of the endocrine disrupting chemicals (EDCs) carbamazepine, clofibric acid, and iopromide by corona discharge over water, *Chemosphere* 75, 163-168.

Kumar, A. (2007) Integrated Photocatalytic and Biological Treatment of Bio-Recalcitrant Compounds in Textile Industry Effluent.

Lau, W. J., and Ismail, A. (2009) Polymeric Nanofiltration Membranes for Textile Dye Wastewater Treatment: Preparation, Performance Evaluation, Transport Modelling, and Fouling Control—a Review, *Desalination* 245, 321-348.

Li, G. S., Li, L. P., and Zheng, J. (2011) Understanding the Defect Chemistry of Oxide Nanoparticles for Creating New Functionalities: A Critical Review, *SCIENCE CHINA Chemistry* 54, 876-886.

Li Puma, G., Bono, A., Krishnaiah, D., and Collin, J. G. (2008) Preparation of Titanium Dioxide Photocatalyst Loaded onto Activated Carbon Support Using Chemical Vapor Deposition: A Review Paper, *Journal of Hazardous Materials* 157, 209-219.

Li, W., Shah, S. I., Sung, M., and Huang, C. P. (2002) Structure and Size Distribution of TiO Nanoparticles Deposited on Stainless Steel Mesh, *Journal of Vacuum Science & Technology B: Microelectronics and Nanometer Structures* 20, 2303.

Li, X., Niu, J., Zhang, J., Li, H., and Liu, Z. (2003) Labeling the Defects of Single-Walled Carbon Nanotubes Using Titanium Dioxide Nanoparticles, *The Journal of Physical Chemistry B* 107, 2453-2458.

Lihua, X., Zhenping, F., Ping, S., and Mao, P. (2010) Effects of corona discharge on the surface structure, morphology and properties of multi-walled carbon nanotubes. *Applied Surface Science* 256, 6447-6453.

Lin, S. H. (1999) Operating Characteristics and Kinetic Studies of Surfactant Wastewater Treatment by Fenton Oxidation, *Water Research* 33, 1735-1741.

Lin, S. H., and Peng, C. F. (1994) Treatment of Textile Wastewater by Electrochemical Method, *Water Research* 28, 277-282.

Linsebigler, A. L., Lu, G., and Yates Jr, J. T. (1995) Photocatalysis on TiO₂ Surfaces: Principles, Mechanisms, and Selected Results, *Chemical Reviews* 95, 735-758.

Liotta, L., Gruttadauria, M., Di Carlo, G., Perrini, G., and Librando, V. (2009) Heterogeneous Catalytic Degradation of Phenolic Substrates: Catalysts Activity, *Journal of Hazardous Materials* 162, 588-606.

Londeree, D. J. (2002) Silica-Titania Composites for Water Treatment, University of Florida.

Macwan, D., Balasubramanian, C., Dave, P., and Chaturvedi, S. (2011) Thermal Plasma Synthesis of Nano Titania and Its Characterization, *Journal of Saudi Chemical Society*.

Malato, S., Fernández-Ibáñez, P., Maldonado, M., Blanco, J., and Gernjak, W. (2009) Decontamination and Disinfection of Water by Solar Photocatalysis: Recent Overview and Trends, *Catalysis Today* 147, 1-59.

Mansor, A. (2008) Photocatalytic Degradation of Phenol in Aqueous Solution Using Fe/TiO₂ Thin Films under UV and Visible Light.

Martin, S. T., Kesselman, J. M., Park, D. S., Lewis, N. S., and Hoffmann, M. R. (1996) Surface Structures of 4-Chlorocatechol Adsorbed on Titanium Dioxide, *Environmental Science & Technology* 30, 2535-2542.

Martínez-Huerta, M., Rodríguez, J., Tsiouvaras, N., Peña, M., Fierro, J., and Pastor, E. (2008) Novel Synthesis Method of Co-Tolerant PtRu-Mo X Nanoparticles: Structural Characteristics and Performance for Methanol Electrooxidation, *Chemistry of Materials* 20, 4249-4259.

Matarredona, O., Rhoads, H., Li, Z., Jeffrey, H., Balzano, L., and Resasco, D. E. (2003) Dispersion of Single-Walled Carbon Nanotubes in Aqueous Solutions of the Anionic Surfactant Naddbs, *The Journal of Physical Chemistry B* 107, 13357-13367.

Méndez-Arriaga, F., Esplugas, S., and Giménez, J. (2008) Photocatalytic Degradation of Non-Steroidal Anti-Inflammatory Drugs with TiO₂ and Simulated Solar Irradiation, *Water Research* 42, 585-594.

Mohammed, A. O. (2007) Evaluation and Testing of a Novel Photocatalytic Reactor with Model Water Pollutants.

Munter, R. (2001) Advanced Oxidation Processes-Current Status and Prospects, *Proc. Estonian Acad. Sci. Chem.* 50, 59-80.

Nash, J. (2006) Human Safety and Efficacy of Ultraviolet Filters and Sunscreen Products, *Dermatologic Clinics* 24, 35-51.

Nian, J. N., and Teng, H. (2006) Hydrothermal Synthesis of Single-Crystalline Anatase TiO₂ Nanorods with Nanotubes as the Precursor, *The Journal of Physical Chemistry B* 110, 4193-4198.

Ning, Y., Alguacil, F., Adeva, P., Alonso, M., Cortie, M., Maaroo, A., Smith, G., Garcia-Guinea, J., Correcher, V., and Rojas, R. (2005) Gold Bulletin, *Gold Bulletin* 38, 1.

Ollis, D., Pelizzetti, E., and Serpone, N. (1991) Photocatalyzed Destruction of Water Contaminants, *Environmental Science & Technology* 25, 1522-1529.

Otieno, F., and Ochieng, G. (2007) Water Management Tools as a Means of Averting a Possible Water Scarcity in South Africa by the Year 2025, *Water SA* 30, 120-124.

Oturan, M. A., Oturan, N., Lahitte, C., and Trevin, S. (2001) Production of Hydroxyl Radicals by Electrochemically Assisted Fenton's Reagent:: Application to the Mineralization of an Organic Micropollutant, Pentachlorophenol, *Journal of Electroanalytical Chemistry* 507, 96-102.

Park, H. J., Park, M., Chang, J. Y., and Lee, H. (2008) The Effect of Pre-Treatment Methods on Morphology and Size Distribution of Multi-Walled Carbon Nanotubes, *Nanotechnology* 19, 335702.

Paz, Y. (2010) Application of TiO₂ Photocatalysis for Air Treatment: Patents' Overview, *Applied Catalysis B: Environmental* 99, 448-460.

Pera-Titus, M., Garcia-Molina, V., Banos, M. A., Gimenez, J., and Esplugas, S. (2004) Degradation of Chlorophenols by Means of Advanced Oxidation Processes: A General Review, *Applied Catalysis B: Environmental* 47, 219-256.

Pereira, L. S., Cordery, I., and Iacovides, I. (2009) *Coping with Water Scarcity: Addressing the Challenges*, Springer Verlag

Pereira, M. F. R., Soares, S. F., Orfao, J. J. M., and Figueiredo, J. L. (2003) Adsorption of Dyes on Activated Carbons: Influence of Surface Chemical Groups, *Carbon* 41, 811-821.

Pérez-Estrada, L. A., Malato, S., Gernjak, W., Agüera, A., Thurman, E. M., Ferrer, I., and Fernández-Alba, A. R. (2005) Photo-Fenton Degradation of Diclofenac: Identification of Main Intermediates and Degradation Pathway, *Environmental Science & Technology* 39, 8300-8306.

Pernicone, N. (2003) Catalysis at the Nanoscale Level, *Cattech* 7, 196-204.

Pillai, S. K., Ray, S. S., and Moodley, M. (2007) Purification of Single-Walled Carbon Nanotubes, *Journal of Nanoscience & Nanotechnology* 7, 3011-3047.

Pirkanniemi, K., and Sillanpää, M. (2002) Heterogeneous Water Phase Catalysis as an Environmental Application: A Review, *Chemosphere* 48, 1047-1060.

Pokryvailo, A., Wolf, M., Yankelevich, Y., Wald, S., Grabowski, L., van Veldhuizen, E. M., Rutgers, W. R., Reiser, M., Glocker, B., and Eckhardt, T. (2006) High-Power Pulsed Corona for Treatment of Pollutants in Heterogeneous Media, *Plasma Science, IEEE Transactions on Plasma Science* 34, 1731-1743.

Qamar, M., Muneer, M., and Bahnemann, D. (2006) Heterogeneous Photocatalysed Degradation of Two Selected Pesticide Derivatives, Triclopyr and Daminozid in Aqueous Suspensions of Titanium Dioxide, *Journal of Environmental Management* 80, 99-106.

Rajeshwar, K., Chenthamarakshan, C., Goeringer, S., and Djukic, M. (2001) Titania-Based Heterogeneous Photocatalysis. Materials, Mechanistic Issues, and Implications for Environmental Remediation, *Pure and Applied Chemistry* 73, 1849-1860.

Rakov, E. G. (2000) Methods for Preparation of Carbon Nanotubes, *Russian Chemical Reviews* 69, 35.

Ramesh, R., and Spaldin, N. A. (2007) Multiferroics: Progress and Prospects in Thin Films, *Nature Materials* 6, 21-29.

Reyes-Coronado, D., Rodríguez-Gattorno, G., Espinosa-Pesqueira, M., Cab, C., De Coss, R., and Oskam, G. (2008) Phase-Pure TiO₂ Nanoparticles: Anatase, Brookite and Rutile, *Nanotechnology* 19, 145605.

Robinson, T., McMullan, G., Marchant, R., and Nigam, P. (2001) Remediation of Dyes in Textile Effluent: A Critical Review on Current Treatment Technologies with a Proposed Alternative, *Bioresource Technology* 77, 247-255.

Royne, A., Dey, C. J., and Mills, D. R. (2005) Cooling of Photovoltaic Cells under Concentrated Illumination: A Critical Review, *Solar Energy Materials and Solar Cells* 86, 451-483.

Sakthivel, S., and Kisch, H. (2003) Daylight Photocatalysis by Carbon Modified Titanium Dioxide, *Angewandte Chemie International Edition* 42, 4908-4911.

Samantaa, A. K., and Agarwal, P. (2009) Application of Natural Dyes on Textiles, *Indian Journal of Fibre & Textile Research* 34, 384-399.

Santhi, T., Manonmani, S., Smitha, T., and Mahalakshmi, K. (2009) Adsorption Kinetics of Cationic Dyes from Aqueous Solution by Bioadsorption onto Activated Carbon Prepared from Cucumis Sativa, *Journal of Applied Sciences in Environmental Sanitation* 4, 263-271.

SayIlkan, F., Asilturk, M., Erdemoglu, S., Akarsu, M., SayIlkan, H., Erdemoglu, M., and Arpaç, E. (2006) Characterization and Photocatalytic Properties of TiO₂-Nanosols Synthesized by Hydrothermal Process at Low Temperature, *Materials Letters* 60, 230-235.

Schäfer, A., Nghiem, L., and Waite, T. (2003) Removal of the Natural Hormone Estrone from Aqueous Solutions Using Nanofiltration and Reverse Osmosis, *Environmental science & technology* 37, 182-188.

Schlager, K. J., and Gorski, S. H. (2008) Electroionic Flow Cell Electrode Configuration, US Patent App. 20,080/264, 800.

Schummer, J. (2007) The Global Institutionalization of Nanotechnology Research: A Bibliometric Approach to the Assessment of Science Policy, *Scientometrics* 70, 669-692.

Serp, P., Corrias, M., and Kalck, P. (2003) Carbon Nanotubes and Nanofibers in Catalysis, *Applied Catalysis A: General* 253, 337-358.

Shen, X. P., Yuan, A. H., Wang, F., Hong, J. M., and Xu, Z. (2005) Fabrication of Well-Aligned Cds Nanotubes by Cvd-Template Method, *Solid State Communications* 133, 19-22.

Shopa, M., Kolwas, K., Derkachova, A., and Derkachov, G. (2010) Dipole and Quadrupole Surface Plasmon Resonance Contributions in Formation of near-Field Images of a Gold Nanosphere, *Opto-Electronics Review*, 1-8.

Smirnova, A., Dong, X., Hara, H., Vasiliev, A., and Sammes, N. (2005) Novel Carbon Aerogel-Supported Catalysts for Pem Fuel Cell Application, *International Journal of Hydrogen Energy* 30, 149-158.

Solhy, A., Machado, B., Beausoleil, J., Kihn, Y., Gonçalves, F., Pereira, M., Órfão, J., Figueiredo, J., Faria, J., and Serp, P. (2008) Mwcnt Activation and Its Influence on the Catalytic Performance of Pt/Mwcnt Catalysts for Selective Hydrogenation, *Carbon* 46, 1194-1207.

Sonawane, R., Kale, B., and Dongare, M. (2004) Preparation and Photo-Catalytic Activity of Fe-TiO₂ Thin Films Prepared by Sol-Gel Dip Coating, *Materials chemistry and Physics* 85, 52-57.

Tayade, R. J., Natarajan, T. S., and Bajaj, H. C. (2009) Photocatalytic Degradation of Methylene Blue Dye Using Ultraviolet Light Emitting Diodes, *Industrial & Engineering Chemistry Research* 48, 10262-10267.

Theron, J., Walker, J. A., and Cloete, T. E. (2010) Nanotechnology and Water Treatment: Applications and Emerging, *Nanotechnology in Water Treatment Applications*, 1.

Tilli, S., Ciullini, I., Scozzafava, A., and Briganti, F. (2011) Differential Decolorization of Textile Dyes in Mixtures and the Joint Effect of Laccase and Cellobiose Dehydrogenase Activities Present in Extracellular Extracts from *Funalia Trogii*, *Enzyme and Microbial Technology*.

Tseng, T. K., Lin, Y. S., Chen, Y. J., and Chu, H. (2010) A Review of Photocatalysts Prepared by Sol-Gel Method for Vocs Removal, *International Journal of Molecular Sciences* 11, 2336-2361.

Wang, W., Serp, P., Kalck, P., and Faria, J. L. (2005) Photocatalytic Degradation of Phenol on Mwnt and Titania Composite Catalysts Prepared by a Modified Sol-Gel Method, *Applied Catalysis B: Environmental* 56, 305-312.

Watanabe, T., Nakajima, A., Wang, R., Minabe, M., Koizumi, S., Fujishima, A., and Hashimoto, K. (1999) Photocatalytic Activity and Photoinduced Hydrophilicity of Titanium Dioxide Coated Glass, *Thin Solid Films* 351, 260-263.

Watts, P., and Haswell, S. J. (2005) The Application of Micro Reactors for Organic Synthesis, *Chem. Soc. Rev.* 34, 235-246.

Weisz, A., Garcia Rodenas, L., Morando, P., Regazzoni, A., and Blesa, M. (2002) Ftir Study of the Adsorption of Single Pollutants and Mixtures of Pollutants onto Titanium Dioxide in Water: Oxalic and Salicylic Acids, *Catalysis Today* 76, 103-112.

Whatmore, R. W. (2006) Nanotechnology-What Is It? Should We Be Worried?, *Occupational Medicine* 56, 295.

Xu, C., and Zhu, J. (2004) One-Step Preparation of Highly Dispersed Metal-Supported Catalysts by Fluidized-Bed MOCVD for Carbon Nanotube Synthesis, *Nanotechnology* 15, 1671.

Xu, P., Janex, M. L., Savoye, P., Cockx, A., and Lazarova, V. (2002) Wastewater Disinfection by Ozone: Main Parameters for Process Design, *Water Research* 36, 1043-1055.

Yang, H., and Griffiths, P. R. (1999) Application of Multilayer Feed-Forward Neural Networks to Automated Compound Identification in Low-Resolution Open-Path FT-IR Spectrometry, *Analytical Chemistry* 71, 751-761.

You, X., Chen, F., Zhang, J., and Anpo, M. (2005) A Novel Deposition Precipitation Method for Preparation of Ag-Loaded Titanium Dioxide, *Catalysis Letters* 102, 247-250.

Yu, J. C., Yu, J., Ho, W., Jiang, Z., and Zhang, L. (2002) Effects of F-Doping on the Photocatalytic Activity and Microstructures of Nanocrystalline TiO₂ Powders, *Chemistry of Materials* 14, 3808-3816.

Zhdanov, V., and Kasemo, B. (2000) Simulations of the Reaction Kinetics on Nanometer Supported Catalyst Particles, *Surface Science Reports* 39, 25-104.

